

DEPARTMENT OF PHYSICS  
UNIVERSITY OF JYVÄSKYLÄ  
RESEARCH REPORT No. 9/2006

**STUDIES ON EXOTIC NUCLEI OF ASTROPHYSICAL  
INTEREST NEAR THE  $N=Z$  LINE**

**BY  
ANU KANKAINEN**

Academic Dissertation  
for the Degree of  
Doctor of Philosophy



Jyväskylä, Finland  
August 2006

DEPARTMENT OF PHYSICS  
UNIVERSITY OF JYVÄSKYLÄ  
RESEARCH REPORT No. 9/2006

**STUDIES ON EXOTIC NUCLEI OF ASTROPHYSICAL  
INTEREST NEAR THE  $N=Z$  LINE**

**BY  
ANU KANKAINEN**

Academic Dissertation  
for the Degree of  
Doctor of Philosophy

*To be presented, by permission of the  
Faculty of Mathematics and Natural Sciences  
of the University of Jyväskylä,  
for public examination in Auditorium FYS-1 of the  
University of Jyväskylä on August 2, 2006  
at 12 o'clock noon*



Jyväskylä, Finland  
August 2006

# Preface

The work reported in this thesis has been carried out during the years 2002-2005 at the Department of Physics of the University of Jyväskylä. Although some of the experiments in this thesis work have been carried out at the ISOLDE facility at CERN, the main part of the work and most of the experiments have been done at the Department of Physics. I would like to thank the whole staff of the Department of Physics for creating a pleasant working atmosphere.

Most of all, I would like to thank my supervisors, professor Juha Äystö and docent Ari Jokinen for giving me the opportunity to do my PhD thesis work in the IGISOL group and for the guidance and encouragement during this project. It has been a pleasure to work in such an exotic and international field of physics. My warmest thanks go to all the people who have participated in the experiments at IGISOL and to the people at ISOLDE, especially to the IS394 and IS403 collaborations. I would like to express my gratitude to Dr. Youbao Wang, Dr. Hans Fynbo and Dr. Luis Fraile for their help and know-how in the setting up of the DSSSDs and the ISOLDE Silicon Ball and in the related data analysis. I would also like to thank professor Yoshitaka Fujita for his efforts in the study of isospin symmetry of transitions within the IS403 collaboration. Dr. Mario Santana Leitner and Dr. Kari Peräjärvi deserve thanks for introducing me to the ISOLDE target development. I wish to express my sincere thanks to the intensive and fruitful collaboration with the professor Yuri Novikov and Dr. Gleb Vorobjev in the experiments in the  $A \approx 80$  region and in the related data analysis. The contribution of Ms. Ulrike Hager in the mass measurements and the related data analysis is highly acknowledged. Thanks go also to Dr. Iain Moore, who has patiently read through the related articles, and to all the members of the IGISOL group for their efforts during the years.

The financial support from the Graduate School in Particle and Nuclear Physics (GRASPANP), from the rector of the University of Jyväskylä and from the Alfred Kordelin's foundation are gratefully acknowledged. I wish to thank the Waldemar von Frenckell's foundation and GRASPANP for providing me an opportunity to participate in the experiments at CERN and in various summer schools and conferences.

Finally, I would like to thank my husband Tomi, my parents and my sister for all the support and encouragement.

Jyväskylä, April 2006

Anu Kankainen

# Abstract

In this thesis work, beta decays of nuclei close to the  $N = Z$  line have been studied at the ISOLDE facility at CERN and at the IGISOL facility in the Accelerator Laboratory of the University of Jyväskylä. In addition, masses of 13 neutron-deficient nuclides have been measured with the JYFLTRAP setup at IGISOL. The nuclides of interest have been produced via fusion-evaporation reactions at IGISOL and via spallation reactions at ISOLDE. With novel silicon detector setups and high-efficiency HPGe detectors, important information on the beta-decays of  $^{31}\text{Cl}$  and  $^{58}\text{Zn}$  has been obtained. Previously controversial proton peaks from the beta decay of  $^{31}\text{Cl}$  have been confirmed and a new proton peak of potential interest for nova nucleosynthesis has been found. The Gamow-Teller strength of a transition in the beta decay of  $^{58}\text{Zn}$  has been found to agree with the strength of the analogous transition in  $^{58}\text{Ni}(^3\text{He},t)$  charge-exchange reactions. In the mass  $A \approx 80$  region, decay properties of several nuclei have been investigated and masses of 13 nuclides have been measured with an accuracy better than 10 keV. Large deviations to the tabulated values have been found for the measured masses. The results from these experiments are useful for astrophysical network calculations which help to understand how elements are synthesized in various astrophysical sites, such as in novae and in X-ray bursts.

# Contents

<b>1</b>	<b>Introduction</b>	<b>1</b>
<b>2</b>	<b>Theoretical and astrophysical background</b>	<b>5</b>
2.1	Theoretical background . . . . .	5
2.1.1	Shell model . . . . .	5
2.1.2	Isospin . . . . .	7
2.1.3	Isobaric multiplet mass equation . . . . .	8
2.1.4	Symmetries in nuclei close to the $N = Z$ line . . . . .	9
2.2	Beta decay . . . . .	10
2.2.1	Transition strength and selection rules . . . . .	10
2.2.2	Allowed Fermi decay . . . . .	12
2.2.3	Allowed Gamow-Teller decay . . . . .	13
2.2.4	Charge-exchange reactions and the GT strength . . . . .	14
2.2.5	Beta-delayed decay modes . . . . .	16
2.3	Astrophysical motivation . . . . .	19
2.3.1	Rapid proton capture (rp) process . . . . .	20
2.3.2	Nucleosynthesis in novae . . . . .	25
2.3.3	$^{81}\text{Br}$ as a solar neutrino detector . . . . .	27
<b>3</b>	<b>Experimental method</b>	<b>29</b>
3.1	Isotope Separator On-Line (ISOL) facilities . . . . .	29
3.1.1	ISOLDE . . . . .	29
3.1.2	IGISOL . . . . .	32
3.2	Experimental setups . . . . .	36
3.2.1	MINIBALL detectors for beta-delayed $\gamma$ -rays of $^{58}\text{Zn}$ . . . . .	36
3.2.2	ISOLDE Silicon Ball for beta-delayed protons of $^{58}\text{Zn}$ . . . . .	38
3.2.3	Double-Sided Silicon Strip Detectors for the beta decay of $^{31}\text{Cl}$ . . . . .	40
3.2.4	$\Delta E$ -E detector setup for beta-delayed protons of Kr isotopes . . . . .	43
3.2.5	ELLI setup for the studies of isomers around $A \approx 80$ . . . . .	43
3.2.6	JYFLTRAP for high-precision mass measurements . . . . .	44
<b>4</b>	<b>Results and discussion</b>	<b>47</b>
4.1	Excited states of $^{31}\text{S}$ studied via beta decay of $^{31}\text{Cl}$ . . . . .	47
4.1.1	Beta-delayed $\gamma$ -rays . . . . .	48
4.1.2	Beta-delayed protons . . . . .	52
4.1.3	Branching ratios . . . . .	54

4.1.4	Discussion . . . . .	57
4.2	Beta decay of $^{58}\text{Zn}$ and isospin symmetry of transitions . . . . .	60
4.2.1	Beta-delayed $\gamma$ rays and half-life of $^{58}\text{Zn}$ . . . . .	62
4.2.2	Branching ratios and GT strengths . . . . .	64
4.2.3	ISOLDE Silicon Ball and beta-delayed protons of $^{58}\text{Zn}$ . . . . .	67
4.3	Search for $^{69}\text{Kr}$ . . . . .	71
4.4	Isomers of astrophysical interest close to $A = 80$ . . . . .	72
4.4.1	$A=81$ . . . . .	72
4.4.2	$A=85$ . . . . .	74
4.4.3	$A=86$ . . . . .	79
4.5	The decay of $^{81m}\text{Kr}$ and $^{81}\text{Br}$ solar neutrino detector . . . . .	82
4.6	Masses of neutron-deficient nuclides near $A = 80$ . . . . .	85
4.6.1	Measured masses . . . . .	85
4.6.2	Isomers . . . . .	87
4.6.3	Y isotopes . . . . .	88
4.6.4	Zr isotopes . . . . .	91
4.6.5	Nb isotopes . . . . .	94
4.6.6	Discussion . . . . .	98
<b>5</b>	<b>Summary and outlook</b>	<b>103</b>
	<b>References</b>	<b>107</b>

# 1 Introduction

The neutron-deficient nuclei close to the  $N = Z$  line have almost equal numbers of protons and neutrons. At higher masses, these nuclei lie further away from the stable nuclides (see fig. 1.1) and thus, they are quite exotic with short half-lives and low production cross sections. Beta-decay studies on these nuclei provide information on half-lives, branching ratios and beta-decay strengths of the transitions which can be compared, *e.g.*, to the shell-model calculations. Closer to the dripline, beta-decay  $Q$ -values increase and more exotic decay channels, such as proton or two-proton decays, can occur.

Symmetries play an important role in the nuclei close to the  $N = Z$  line. Assuming that the nuclear force is charge symmetric, protons and neutrons can be treated as two different states of a nucleon described by a new quantum number, isospin. Isospin symmetry suggests that the states in mirror nuclei, such as  $^{31}_{15}\text{P}_{16}$  and  $^{31}_{16}\text{S}_{15}$ , should be analogous and their excitation energies should be the same except for the Coulomb force and for the proton-neutron mass difference. Isospin symmetry of analogue transitions can be probed for example via beta decay of  $^{58}\text{Zn}$  which is also useful for testing a so-called pseudo-SU(4) symmetry.

The studies of the nuclei close to the  $N = Z$  line are of great help in explaining how elements are made in the Universe. Namely, the astrophysical rapid proton (rp) capture process responsible for the nucleosynthesis of heavier elements in hot and dense hydrogen-rich astrophysical sites, such as in X-ray bursts, depends mainly on the beta-decay half-lives and the masses of the nuclides on its path. The rp process proceeds as a sequence of beta-decays and proton captures close to the proton dripline up to the tin region. The nuclides around the mass  $A = 80$  region can be substantially deformed and rich in isomers. Information on the beta decays, existing isomers and the masses of these nuclides can be used in the network calculations which estimate the average time scale, abundances of the produced elements and the end-point of the process. An interesting open question in astrophysics is whether large amounts of so-called p-nuclei produced in the rp process, such as  $^{98}\text{Mo}$ ,  $^{102}\text{Pd}$  and  $^{106}\text{Cd}$ , can explain the origin of these nuclides in the solar system.

There have been many studies on the nuclei near or at the  $N = Z$  line via in-beam spectroscopy where the focus is on the high-spin states and rotational bands. For example, the nuclides  $^{58}\text{Cu}$  [Rud02] and  $^{85}\text{Zr}$  [Tan02] have been studied in detail and their rotational bands are well-known. However, the low-lying structures of these ex-

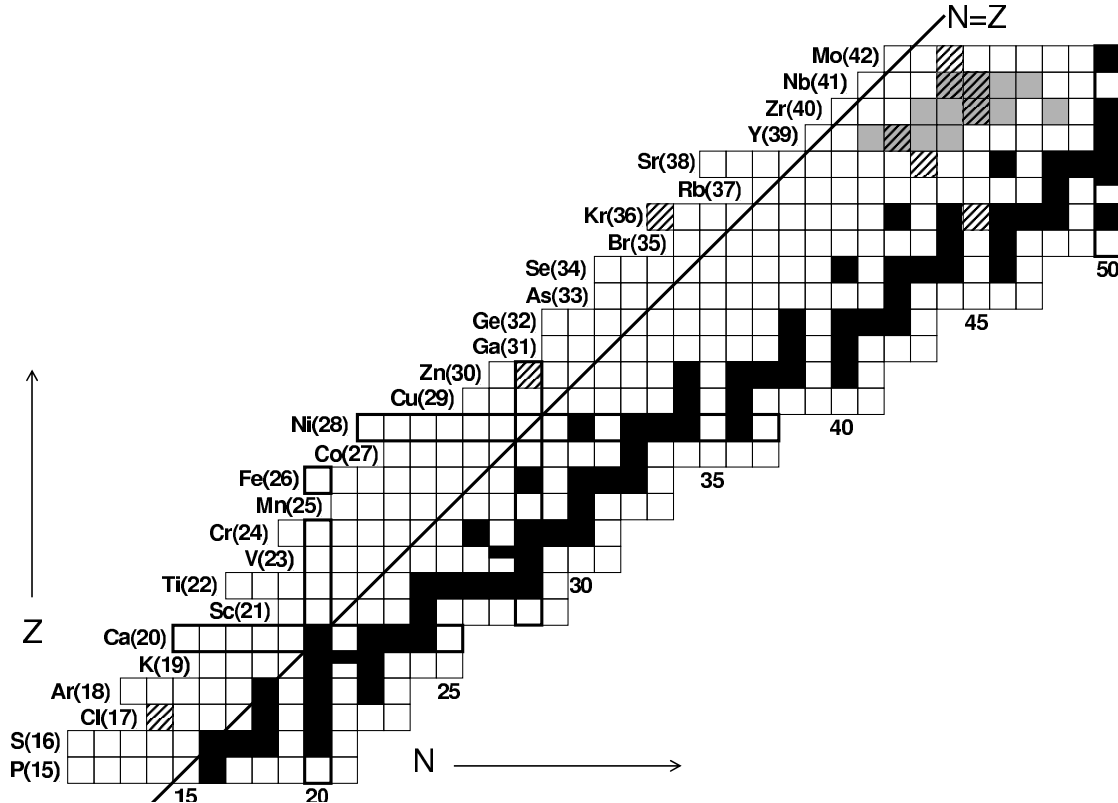


**Figure 1.1:** A part of the chart of the nuclides. The nuclides studied via beta decay have been hatched and the nuclides whose masses have been determined in this work are in grey. Stable nuclei are in black and the shell closures at  $N, Z=20, 28$  and  $N=50$  have been highlighted in the chart.

otic nuclei have not been extensively probed via beta-delayed gamma or proton spectroscopy. Some of these low-energy transitions decay via internal conversion instead of gamma decays. The observation of conversion electrons and low-energy gamma transitions is useful in determining the type of the transition and possible spin and parity assignments for the initial and/or final states. These observations can also serve as a link to in-beam studies where the position of the lowest observed level might be unknown.

In this work, the beta decays of  $^{31}\text{Cl}$ ,  $^{58}\text{Zn}$ ,  $^{69}\text{Kr}$ ,  $^{81}\text{Y}$ ,  $^{81}\text{Sr}$ ,  $^{85}\text{Nb}$ ,  $^{85}\text{Zr}$ ,  $^{86}\text{Mo}$  and  $^{86}\text{Nb}$  situated close to the  $N = Z$  line (see fig. 1.1) have been explored via gamma, proton or conversion electron spectroscopy. In addition, the isomeric transition in  $^{81}\text{Kr}$  relevant for a proposed  $^{81}\text{Br}$  solar neutrino detector has been studied. Masses of  $^{80,81,82,83}\text{Y}$ ,  $^{83,84,85,86,88}\text{Zr}$  and  $^{85,86,87,88}\text{Nb}$  have been measured with the JYFLTRAP double Penning trap setup. The short half-lives and low production cross sections of these nuclides demand efficient facilities. The search experiment for  $^{69}\text{Kr}$  was performed at the ISOLDE facility at CERN whereas all the other nuclides have been

studied at the IGISOL facility in the Accelerator Laboratory of the University of Jyväskylä. The beta decay of  $^{58}\text{Zn}$  has been studied both at ISOLDE and at IGISOL.

This thesis work is a continuation of a series of PhD works on the  $N = Z$  nuclei done in the IGISOL group during the last decades. Beta-delayed particle emission from  $^{20}\text{Na}$ ,  $^{24}\text{Al}$ ,  $^{28}\text{P}$ ,  $^{32}\text{Cl}$ ,  $^{36}\text{K}$  and  $^{40}\text{Sc}$  were studied already in the PhD work of J. Honkanen [Hon81]. High-isospin nuclei  $^{31,33}\text{Ar}$  and  $^{41}\text{Ti}$  were investigated in the thesis of A. Honkanen [Hon98]. At the same time, M. Oinonen concentrated on the decay studies of  $^{58}\text{Zn}$ ,  $^{70,71}\text{Kr}$  and  $^{73,74}\text{Rb}$  and performed a survey experiment in the mass  $A = 80$  region [Oin98a]. K. Peräjärvi's work on the beta-decay of  $^{23}\text{Al}$  provided essential information for the astrophysics and the study on the ground-state beta decay of  $^{58}\text{Cu}$  yielded an important input for the normalization of the Gamow-Teller strength in the charge-exchange reactions on  $^{58}\text{Ni}$  [Per01a]. J. Huikari's thesis on the mirror decay of  $^{75}\text{Sr}$  and the isomeric state  $^{80m}\text{Y}$  together with the efforts in the development of the ion-guide method and improvement of the yields at (H)IGISOL have also pushed forward the studies of the  $N = Z$  nuclei at IGISOL [Hui03]. The present PhD thesis continues the work done on the beta decay of  $^{58}\text{Zn}$  by M. Oinonen and extends the studies in the mass  $A = 80$  region. A special attention has been paid to the astrophysical motivation of these studies. These PhD theses show that the interest in the  $N = Z$  nuclei has been high in the IGISOL group. Experimental setups and the production methods have been continuously developed in order to explore these exotic nuclear species.

This thesis work is based on the publications listed below. The author has written all the articles 1-5. She has been actively involved in the setting up and running the experiments and has done the related data analysis for the papers 1-4. Concerning the paper 1, the Monte Carlo simulations have been done by M. Santana Leitner. For the publication 5, the author has participated in the experiment and done the further analysis based on the masses determined via time-of-flight resonances.

1. **Optimization of krypton yields for rp-process studies at ISOLDE (CERN)**

A. Kankainen, M. Santana Leitner, L.M. Fraile, A. Jokinen, M. Oinonen, K. Peräjärvi, H. Ravn, J. Äystö and the ISOLDE Collaboration, Nucl. Phys. A **746**, 433c (2004).

2. **Beta-delayed gamma and proton spectroscopy near the  $Z = N$  line**

A. Kankainen, S.A. Eliseev, T. Eronen, S.P. Fox, U. Hager, J. Hakala, W. Huang, J. Huikari, D. Jenkins, A. Jokinen, S. Kopecky, I. Moore, A. Nieminen, Yu.N. Novikov, H. Penttilä, A.V. Popov, S. Rinta-Antila, H. Schatz, D.M. Seliverstov, G.K. Vorobjev, Y. Wang, J. Äystö, and the IS403 Collaboration, Eur. Phys. J. A **25**, Supplement 1, 129 (2005).

3. **Isomers of astrophysical interest in neutron-deficient nuclei at masses  $A=81, 85$  and  $86$**   
A. Kankainen, G.K. Vorobjev, S.A. Eliseev, W. Huang, J. Huikari, A. Jokinen, A. Nieminen, Yu.N. Novikov, H. Penttilä, A.V. Popov, S. Rinta-Antila, H. Schatz, D.M. Seliverstov, Yu.P. Suslov and J. Äystö,  
Eur. Phys. J. A **25**, 355 (2005).
4. **Excited states in  $^{31}\text{S}$  studied via beta decay of  $^{31}\text{Cl}$**   
A. Kankainen, T. Eronen, S.P. Fox, H.O.U. Fynbo, U. Hager, J. Hakala, J. Huikari, D.G. Jenkins, A. Jokinen, S. Kopecky, I. Moore, A. Nieminen, H. Penttilä, S. Rinta-Antila, O. Tengblad, Y. Wang and J. Äystö,  
Eur. Phys. J. A **27**, 67 (2006).
5. **Mass measurements of neutron-deficient nuclides close to  $A \approx 80$  with a Penning trap**  
A. Kankainen, L. Batist, S.A. Eliseev, V.-V. Elomaa, T. Eronen, U. Hager, J. Hakala, A. Jokinen, I. Moore, Yu.N. Novikov, H. Penttilä, K. Peräjärvi A.V. Popov, S. Rahaman, S. Rinta-Antila, P. Ronkanen, A. Saastamoinen, D.M. Seliverstov, T. Sonoda, G.K. Vorobjev and J. Äystö,  
Submitted to Eur. Phys. J. A.

# 2 Theoretical and astrophysical background

The motivation for the studies of exotic nuclei close to the  $N = Z$  line arises both from the theoretical background and from the nuclear astrophysics. Experimental data are needed to test the nuclear shell model and the isospin symmetry in mirror nuclei or in analogous transitions of an isobaric multiplet (see secs. 2.1 and 2.2.4). An overview of beta decay is given in sec. 2.2. Beta decays of these neutron-deficient nuclei play a crucial role in nuclear astrophysics, especially in the astrophysical  $rp$  process (see sec. 2.3).

## 2.1 Theoretical background

Beta-decay experiments on nuclei close to the  $N = Z$  line provide useful information for testing the nuclear shell model and isospin symmetry of nuclei. The shell model and the concept of isospin are discussed below with an emphasis on the subjects relevant for the experiments carried out in this PhD thesis work. The isobaric multiplet mass equation can be used to estimate the nuclear mass of a member in an isobaric multiplet. This is dealt separately in sec. 2.1.3.

### 2.1.1 Shell model

In the nuclear shell model, a nucleon is moving in a potential created by the other nucleons in the nucleus. As fermions, protons and neutrons obey the Pauli exclusion principle and thus, there cannot be two identical particles in the same quantum state. Discontinuities in the binding energies at magic proton or neutron numbers (2, 8, 20, 28, 50, 82 and 126) and the systematics in the spins and parities gave strong experimental support for the model. Although the shell structure of nuclei was noticed already in the 1930s, the correct shell-model description was achieved in 1949 when the spin-orbit potential was included in the model. A thorough review on the shell-model can be found in [Cau05].

The nuclei studied in this work belong to an  $sd$  or  $pf$  shell. The  $sd$  shell consists of

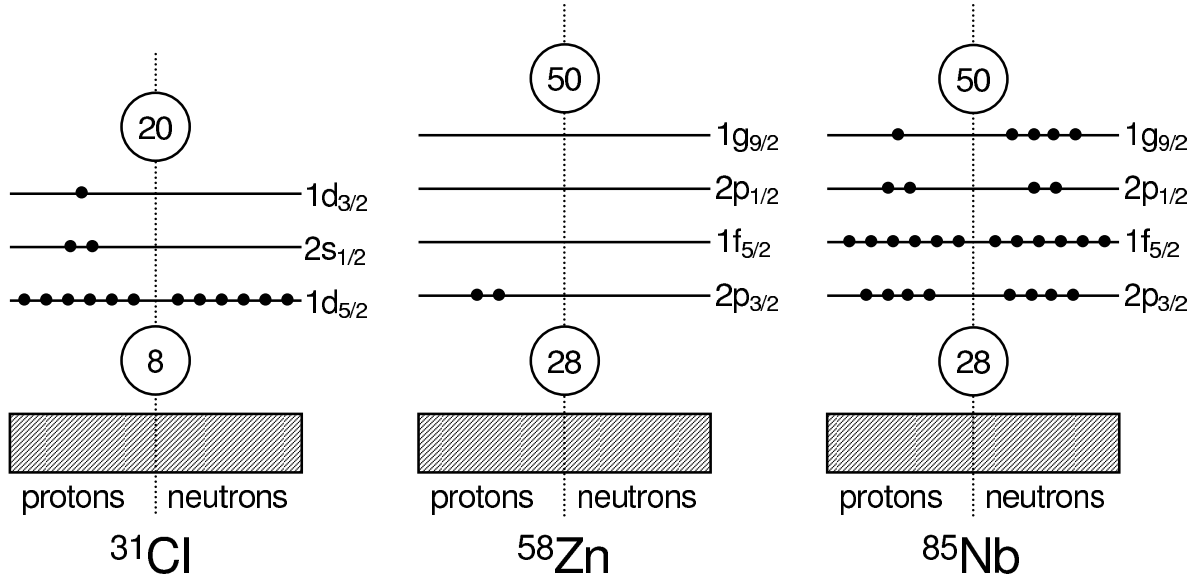


**Figure 2.1:** A schematic view of the occupation of the shell-model single-particle states in  ${}^{31}_{17}\text{Cl}_{14}$ ,  ${}^{58}_{30}\text{Zn}_{28}$  and  ${}^{85}_{41}\text{Nb}_{44}$ . The ground state spins of  ${}^{31}\text{Cl}$  and  ${}^{58}\text{Zn}$ ,  $3/2^+$  and  $0^+$ , can be predicted from this model. The ground state spin of  ${}^{85}_{41}\text{Nb}_{44}$  is not experimentally determined but it is expected to be  $9/2^+$  corresponding to a  $\pi 1g_{9/2}$  single-particle state (see fig. 2.1).

$1d_{5/2}$ ,  $2s_{1/2}$  and  $1d_{3/2}$  shells each of which can be occupied by  $2j + 1$  nucleons. An example of an  $sd$ -shell nucleus is  ${}^{31}_{17}\text{Cl}_{14}$  (see fig. 2.1). The other studied nuclei belong to the  $pf(g)$ -shell which consists of  $1f_{7/2}$ ,  $2p_{3/2}$ ,  $1f_{5/2}$ ,  $2p_{1/2}$  and  $1g_{9/2}$  shells. For the studied  $pf(g)$ -shell nuclei, the  $1f_{7/2}$  shell is fully occupied and therefore, the major contribution comes from the upper shells. An example of such a nucleus is  ${}^{58}_{30}\text{Zn}_{28}$  (see fig. 2.1). The  $sd$ -shell nuclei have been modeled successfully with a universal  $sd$  interaction in the past [Cau05]. Applying the shell model to the  $pf$  shell is more complicated due to a much larger valence space. Nowadays matrices with determinantal spaces of dimensionality up to  $10^9$  can be diagonalized and the shell-model calculations can be performed for the  $pf(g)$ -shell nuclei (see, *e.g.*, [Kan04]).

Nuclei far away from the closed shells are often non-spherical, and thus, have a prolate ( $\beta_2 > 0$ ) or an oblate ( $\beta_2 < 0$ ) deformed shape. The proton-neutron interactions were proposed to be responsible for collectivity and deformation in nuclei a long time ago [Tal62]. The magnitude of the  $pn$ -interaction (and deformation) can be estimated with an  $N_p N_n$  scheme [Cas85] which relates the number of valence protons and neutrons to the average proton-neutron interaction. Most of the studied nuclei, such as  ${}^{31}\text{Cl}$  and  ${}^{58}\text{Zn}$ , have spherical ground states [Möl95]. The  ${}^{69}\text{Kr}$  ought to have the most oblate ground state ( $\beta_2 \approx -0.3$  [Möl95]) and  ${}^{80,81}\text{Y}$  should have the largest prolate deformation ( $\beta_2 \approx 0.4$  [Möl95]). The other studied nuclei around mass  $A = 80$  should be slightly prolate ( $\beta_2 \approx 0.05$  [Möl95]). Experiments have shown that the nuclei around  $A = 80$  are highly deformed, such as  ${}^{80}\text{Zr}$  ( $\beta_2 \approx 0.4$  [Lis87]). Drastic changes in nuclear

shape and shape coexistence can be observed in these nuclei. As the  $1g_{9/2}$  orbit can occupy ten nucleons, it plays a crucial role in triggering the deformation. When moving towards the doubly-magic closed shell at  $N = Z = 50$ , the deformation decreases. In addition to the deformation, the lack of suitable final states due to the filling of the  $1g_{9/2}$  shell and its interplay with the  $pf$  shell may introduce long-lived isomeric states in the region close to  $A = 80$ .

### 2.1.2 Isospin

According to charge symmetry, the proton-proton interaction is identical to the neutron-neutron interaction after the correction for the Coulomb force. Isospin  $T$  is a quantum number that treats protons and neutrons as two different states of a nucleon. The isospin of a proton or a neutron is  $\frac{1}{2}$  whereas the isospin projection to an arbitrary  $Z$ -axis is  $t_Z = -\frac{1}{2}$  for protons and  $t_Z = +\frac{1}{2}$  for neutrons. The total  $Z$ -component of the isospin,  $T_Z$  is a sum of the  $Z$ -axis components of all nucleons,  $t_{Zi}$  (see eq. 2.1). If charge symmetry is assumed, isospin is a good quantum number and it must be conserved in strong interaction reactions.

Coupling of isospin follows the same rules as an ordinary angular momentum coupling. For an isospin projection  $T_Z$  defined by the eq. 2.1, the total isospin can take any value greater than or equal to  $|T_Z|$ . Usually the lowest states in a nucleus have  $T = |T_Z|$  due to the symmetry. This is not always the case. For example in  ${}^{58}_{29}\text{Cu}_{29}$  ( $T_Z = 0$ ) the ground state is a  $T = 1$  state and the first excited state is a  $T = 0$  state.

$$T_Z = \sum_i t_{Zi} = \frac{1}{2}(N - Z) \quad (2.1)$$

Isospin multiplets are isobars which have states with the same isospin  $T$  but with different isospin projection  $T_Z = T, T - 1, \dots, -T$ . For example mirror nuclei, such as  ${}^{31}_{16}\text{S}_{15}$  and  ${}^{31}_{15}\text{P}_{16}$ , have  $T_Z = \pm\frac{1}{2}$  and the states with  $T = \frac{1}{2}$  are isobaric analog states (IAS). These states have identical wave functions except for the change in proton and neutron numbers. The energies of the isobaric analog states are almost identical after the correction for the Coulomb interaction and proton-neutron mass difference. The isobaric triplet at  $A = 58$  has  $T = 1$  isobaric analog states in  ${}^{58}_{30}\text{Zn}$  ( $T_Z = -1$ ),  ${}^{58}_{29}\text{Cu}$  ( $T_Z = 0$ ) and  ${}^{58}_{28}\text{Ni}$  ( $T_Z = +1$ ). Isobaric quartets, such as the mass  $A = 31$  quartet ( ${}^{31}_{17}\text{Cl}$ ,  ${}^{31}_{16}\text{S}$ ,  ${}^{31}_{15}\text{P}$  and  ${}^{31}_{14}\text{Si}$ ) have  $T = \frac{3}{2}$  isobaric analog states in the corresponding  $T_Z = -\frac{3}{2}, -\frac{1}{2}, +\frac{1}{2}$  and  $+\frac{3}{2}$  nuclei. A detailed description of isospin and related issues can be found in [Wil69].

### 2.1.3 Isobaric multiplet mass equation

Masses of the members in an isobaric multiplet can be related to each other by the Isobaric Multiplet Mass Equation (IMME):

$$M(A, T, T_Z) = a(A, T) + b(A, T)T_Z + c(A, T)T_Z^2 \quad (2.2)$$

where  $a$ ,  $b$  and  $c$  are constants which can be determined from experimental data for isobaric multiplets ( $T \geq \frac{3}{2}$ ). IMME is based on the assumption that isospin is a good quantum number and the members of an isobaric multiplet should have equal energies in the absence of Coulomb interaction. The Coulomb interaction for the members of an isobaric multiplet can be calculated in the first order perturbation theory [Wil69]. When applying the Wigner-Eckart theorem to the expectation value of Coulomb interaction, the  $T_Z$  dependence can be factored out from eq. 2.3:

$$\begin{aligned} E_C(A, T, T_Z) &= \langle \alpha T T_Z | H_C | \alpha T T_Z \rangle \\ &= E_C^{(0)}(A, T) - T_Z E_C^{(1)}(A, T) + (3T_Z^2 - T(T+1))E_C^{(2)}(A, T) \end{aligned} \quad (2.3)$$

IMME can be used to predict masses of proton rich-nuclei provided that at least three masses of the isobaric multiplet are known. The coefficients  $a$  (isoscalar),  $b$  (isovector) and  $c$  (isotensor) have been fitted for nuclei up to mass 60 [Bri98] based on the values from the 1995 atomic mass evaluation [Aud95].

The isovector coefficient  $b$  can be expressed as:

$$b = \Delta_{nH} - \frac{3e^2 A^{2/3}}{5r_0} \quad (2.4)$$

where  $\Delta_{nH}$  is the neutron-hydrogen mass difference,  $\Delta_{nH}=782.354$  keV,  $e$  is the elementary charge,  $A$  is the mass number and  $r_0$  is the parameter in the equation for nuclear radius  $R = r_0 A^{1/3}$ . This value has been fitted for 430 multiplets in [Bri98]. The isovector coefficient  $b$  is useful for mass predictions of proton-rich nuclei with  $T_Z = -T$  if the mass of the corresponding neutron-rich nucleus  $T_Z = T$  is known (see eq. 2.5).

$$M(T_Z = -T) = M(T_Z = T) - 2bT \quad (2.5)$$

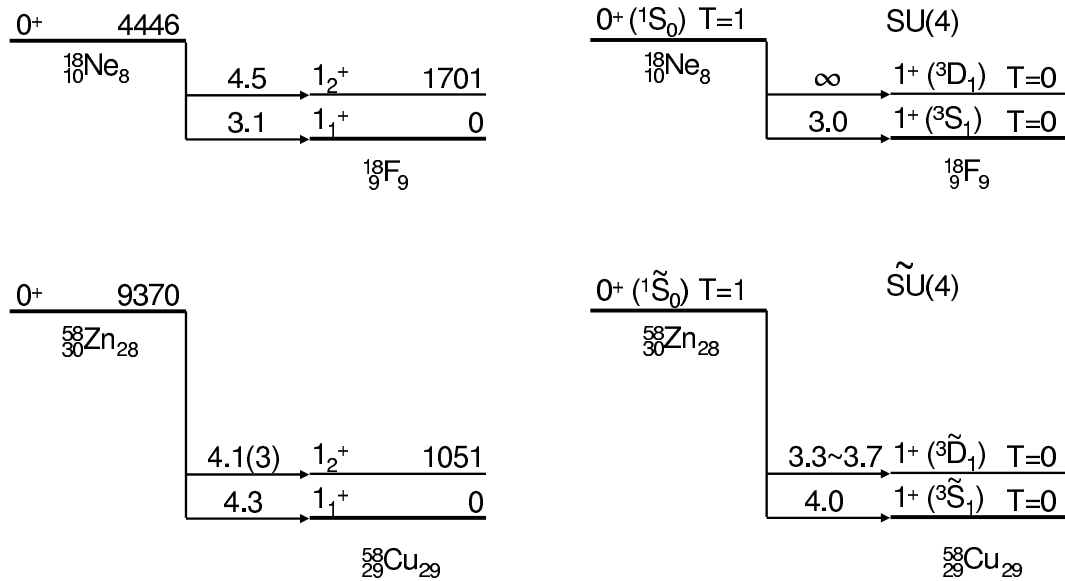


**Figure 2.2:** The  $\log ft$  values for Gamow-Teller matrix elements in the beta decays of  $^{18}\text{Ne}$  and  $^{58}\text{Zn}$  according to ref. [Isa99]. On the left are shown the experimental values and on the right the corresponding SU(4) or pseudo-SU(4) (marked with a tilde).

### 2.1.4 Symmetries in nuclei close to the $N = Z$ line

Symmetries play an important role in nuclei close to the  $N = Z$  line. For example, isospin symmetry (SU(2) algebra) discussed in sec. 2.1.2, can explain the analogous structure of mirror nuclei and the isobaric analog states in isobaric multiplets. Another interesting symmetry model is Wigner's SU(4) supermultiplet model, which assumes that nuclear forces are invariant under rotations both in spin and isospin. However, Wigner's spin-isospin symmetry is known to be broken in heavier nuclei due to the strong spin-orbit coupling of nuclear force and Coulomb interaction. As the shell-model calculations for  $pf$ -shell nuclei are complicated due to a large valence space, a symmetry or an algebra generating the spectrum for these nuclei would be very useful. For this purpose, a *pseudo*-SU(4) symmetry has been proposed for nuclei above  $^{56}\text{Ni}$  [Isa99, Isa02]. In this symmetry, the  $p_{1/2}$ ,  $p_{3/2}$  and  $f_{5/2}$  orbits above  $N, Z = 28$  are treated as a pseudo- $sd$  shell. The pseudo-SU(4) symmetry is expected especially at the beginning of the 28 to 50 shell. Towards the  $N, Z = 50$  shell closures the  $g_{9/2}$  shell starts to play a more important role and the pseudo- $sd$  shell is not so dominant anymore.

The SU(4) and pseudo-SU(4) symmetries can be tested with experimental data on beta-decay probabilities and binding energies. As the nuclear masses along the  $N = Z$  line from  $^{56}\text{Ni}$  to  $^{80}\text{Zr}$  are not yet well-known, the testing has been done via beta decay. The beta decay of  $^{18}\text{Ne}_8$  can be used to test the validity of the SU(4) model [Isa99]. To test the pseudo-SU(4) symmetry, the beta decay of  $^{58}\text{Zn}_{28}$  is crucial [Isa99]. Namely,

${}^{58}_{30}\text{Zn}_{28}$  should be the same to the pseudo- $sd$  shell as  ${}^{18}_{10}\text{Ne}_8$  is to the  $sd$  shell. The  $\log ft$  values for the Gamow-Teller beta decays of  ${}^{18}\text{Ne}$  and  ${}^{58}\text{Zn}$  taken from [Isa99] are shown in fig. 2.2. The SU(4) model can qualitatively explain the beta decay of  ${}^{18}\text{Ne}$ . The beta decay of  ${}^{58}\text{Zn}$  differs from  ${}^{18}\text{Ne}$  and can be better understood with the pseudo-SU(4) model.

## 2.2 Beta decay

Beta decay is a transition between two neighboring nuclear isobars caused by the weak interaction. There are two types of beta-decay modes relevant for the studies of neutron-deficient nuclei close to the  $N = Z$  line, namely  $\beta^+$  and electron-capture ( $EC$ ) decays. In these decays, an excess proton is converted into a neutron, which results in  ${}^A_Z X \rightarrow {}^A_{Z-1} Y + e^+ + \nu_e$  for  $\beta^+$  decay and  ${}^A_Z X + e^- \rightarrow {}^A_{Z-1} Y + \nu_e$  for the  $EC$  decay. A continuous bell-shaped spectrum of positrons is observed with a beta-detector as the energy released in a  $\beta^+$  decay is shared among a positron and a neutrino. In the electron capture, a nucleus captures an electron from an atomic shell, which is observed as an emitted X-ray or an Auger electron. The  $EC$ -decay is the only possible decay mode to the states above  $Q_{EC} - 2m_e c^2$ . Beta-decay  $Q$ -values of nuclei close to the  $N = Z$  line are large and mainly allowed beta decays are important. Thus, beta-decay strengths to a variety of states in daughter nuclei can be studied within the beta-decay  $Q$ -window. The experimental strengths give information on the nuclear matrix elements and they provide a means to test the shell model. An alternative way to study these transition strengths is via charge-exchange reactions which yield experimental information on the strengths to states both below and above the corresponding beta-decay  $Q$ -value. A comparison of charge-exchange reaction strengths and beta-decay strengths can be used to test isospin symmetry within an isospin multiplet.

### 2.2.1 Transition strength and selection rules

The beta-decay transition rate  $\lambda$ , as stated in Fermi's Golden Rule, is

$$\lambda = \frac{2\pi}{\hbar} |M_{fi}|^2 \rho(E_f) \quad (2.6)$$

where the matrix element  $M_{fi}$  is the integral of vector (V) and axial-vector (A) interactions between the initial (i) and final (f) states and  $\rho(E_f)$  is the density of final states ( $dn/dE_f$ ).

The so-called comparative half-life or  $ft$  value offers a means to compare beta-decay probabilities in different nuclei. As the decay probability grows to the fifth power of the decay energy, there are huge variations in beta-decay half-lives. Therefore, usually  $\log_{10} ft$  values are used instead of bare  $ft$  values.

$$f_i t = f_i \times \frac{\ln 2}{\lambda_i} = \ln 2 \times \frac{2\pi^3 \hbar^7}{m_e^5 c^4 g^2 |M_{fi}|^2} \quad (2.7)$$

where  $f = f(Z, E_0)$  is the Fermi integral which takes into account the statistical factor derived from the number of accessible final states and the influence of the Coulomb field. Thus, differences in  $ft$  values arise from the differences in nuclear matrix elements.

There are two types of beta-decay transitions depending on the orientation of positron and neutrino spins. In a Fermi type of transition, the spins of the emitted positron and the neutrino are antiparallel (total  $S = 0$ ), whereas in a Gamow-Teller transition the spins are parallel ( $S = 1$ ). Let us mark the initial and final angular momenta by  $\mathbf{I}_i$  and  $\mathbf{I}_f$ , and the orbital angular momentum carried away by  $\mathbf{L}$ . From the vector addition of angular momenta, the following requirements for Fermi and Gamow-Teller transitions are obtained:

$$\mathbf{I}_f = \mathbf{I}_i + \mathbf{L} \quad \text{for Fermi transitions} \quad (2.8)$$

$$\mathbf{I}_f = \mathbf{I}_i + \mathbf{L} + \mathbf{1} \quad \text{for Gamow-Teller transitions} \quad (2.9)$$

There is no orbital angular momentum  $L$  in allowed beta decays,  $L=0$ . Therefore,  $\Delta I = |I_i - I_f|$ , must be 0 for Fermi decays and  $\Delta I = 0$  or 1 for Gamow-Teller decays, except for  $0^+ \rightarrow 0^+$  decays for which only Fermi decays are possible. The connection between the parity and orbital angular momentum is  $\pi_i = \pi_f (-1)^L$  and thus, parity does not change in allowed beta decays. So-called forbidden decays are not really forbidden but they are much less probable than the allowed beta decays. First-forbidden decays have  $L = 1$ , which results in a parity change and  $\Delta I = 0, 1$  or 2. Most allowed beta decays have  $\log ft$  values between 3.5–7.5 and first-forbidden decays have  $\log ft$  values in the range 6.0–9.0 [Kra88]. Superalowed decays between analog states of an isospin multiplet are very fast as these states have almost identical wave functions resulting in a nuclear matrix element  $|M_{fi}|$  close to 1. The  $\log ft$  values for superallowed decays are below 3.8 [Kan95].

### 2.2.2 Allowed Fermi decay

For allowed beta decay, the matrix element  $M_{fi}$  can be divided into Fermi and Gamow-Teller (GT) matrix elements, which can interact simultaneously in a beta decay. Therefore, the transition rate can be written as:

$$\lambda \propto g^2 |M_{fi}|^2 = G_V^2 \langle M_F \rangle^2 + G_A^2 \langle M_{GT} \rangle^2 \quad (2.10)$$

where  $G_V$  and  $G_A$  are the vector and axial-vector coupling constants. In the allowed approximation, the Fermi operator, *i.e.* the vector part of the interaction, reduces to a unit operator  $\langle 1 \rangle$  and an isospin raising operator  $\tau_+$  which is needed to change a proton into a neutron. A simple formula in isospin formalism is obtained for the Fermi transition strength  $B(F)$  (see, *e.g.*, [Bru77]):

$$B(F) = \langle M_F \rangle^2 = \langle 1 \rangle^2 = T(T+1) - T_{Z_i} T_{Z_f} \quad (2.11)$$

The Fermi operator does not change spin, isospin or parity. In the case of  $\beta^+$  decay, the only thing a Fermi operator does, is the raising of the isospin projection by one,  $T_{Z_f} = T_{Z_i} + 1$ . In other words, Fermi decays occur only between isobaric analog states.

A special case of Fermi decays are the superallowed  $0^+ \rightarrow 0^+$  decays. As these transitions are pure Fermi, they are essential in the testing of the Conserved Vector Current (CVC) hypothesis according to which the vector current constant  $G_V$  is a true constant and not affected by the nuclear medium. Therefore,  $ft$  values of superallowed  $0^+ \rightarrow 0^+$  decays between  $T = 1$  analog states should be identical. Together with a muon lifetime, these decays provide a unique test of the up-down quark-mixing matrix element  $V_{ud}$  of the Cabibbo-Kobayashi-Maskawa (CKM) matrix. Unitarity of the CKM matrix is an important test for the Standard Model and various calculations on this problem have been performed (see refs. [Tow02],[Har02], [Har05] and [Wil05]). In order to compare the experimental  $\log ft$  values of the well-known superallowed  $0^+ \rightarrow 0^+$  decays, a few corrections have to be made. Firstly, radiative correction  $\delta_R$  takes into account that an emitted electron/positron may emit bremsstrahlung photons which are not detected in experiments. Secondly, isospin is not an exact symmetry in nuclei and an isospin-symmetry breaking correction  $\delta_C$  has to be included in the corrected  $ft$  values. A so-called ‘‘corrected’’  $ft$  value obtained by taking into account radiative and isospin corrections is shown in eq. 2.12. However, these corrections are quite small, all of the order of 1 % [Har05].

$$Ft = (1 + \delta_R)(1 - \delta_C)ft \quad (2.12)$$

### 2.2.3 Allowed Gamow-Teller decay

The Gamow-Teller operator is often called  $\sigma\tau$  as it operates on spin and isospin, which can be changed by 0 or 1 in a GT transition. An extreme single-particle estimate for the square of the GT matrix element can be calculated from (see [Bru77]):

$$\langle\sigma\tau\rangle^2 = 6(2j_f + 1) \left\{ \begin{matrix} \frac{1}{2} & \frac{1}{2} & 1 \\ j_i & j_f & l \end{matrix} \right\}^2 \quad (2.13)$$

In this thesis the Gamow-Teller strength  $B(GT)$  has been defined as:

$$B(GT) = \left(\frac{g_A}{g_V}\right)^2 \langle\sigma\tau\rangle^2 \quad (2.14)$$

The  $ft$  value is calculated from:

$$ft = \frac{C}{B(F) + B(GT)} = \frac{C}{\langle 1 \rangle^2 + \left(\frac{g_A}{g_V}\right)^2 \langle\sigma\tau\rangle^2} \quad (2.15)$$

where  $C=6145(4)$  s [Har98] is a constant based on the superallowed  $0^+ \rightarrow 0^+$  transitions. Sometimes eq. 2.15 is given so that the numerator is a constant  $K$ ,  $C = K/g_V^2$ , and the denominator is  $g_V^2 \langle 1 \rangle^2 + g_A^2 \langle\sigma\tau\rangle^2$ . The ratio  $g_A/g_V$  is deduced from the measured beta asymmetry coefficient in the free decay of polarized neutrons [Sch95],  $|g_A/g_V|=1.266(4)$ . A more recent value derived from a free neutron lifetime is given in [Gro00],  $|g_A/g_V| = 1.2670(35)$ .

The Gamow-Teller strength of a beta transition can be determined from eq. 2.15. In order to define the  $ft$  value, the  $Q_{EC}$  value must be known for the phase space factor  $f$  as well as the corresponding branching ratio and half-life for the partial half-life (see eq. 2.7). A model independent Ikeda sum rule [Ike62] can be derived for GT transitions:

$$\sum_f (\langle\sigma\tau_-\rangle^2 - \langle\sigma\tau_+\rangle^2) = 3(N - Z) \quad (2.16)$$

where  $\sigma\tau_-$  refers to  $\beta^-$  decay and  $\sigma\tau_+$  corresponds  $\beta^+$  decay of the nucleus  $(Z, N)$ . The sum goes over all final states in daughter nuclei  $(Z + 1, N - 1)$  and  $(Z - 1, N + 1)$ , respectively.

A comparison of  $(p, n)$  and  $(n, p)$  data has revealed that only about half of the sum-rule value is found in the experiments. Thus, the experimentally observed GT strength is suppressed, *i.e.* quenched, compared to the model independent prediction. Another indication of quenching comes from individual peaks seen in beta decays, which are much weaker than predicted with the shell model. Several reasons for the quenching have been proposed. The discrepancy between the shell-model strengths and the experimental values can be explained by nuclear configuration mixing [Ber82, Cau95]. Energetically high-lying 2p-2h states mix with the 1p-1h GT states and shift the strength towards higher energies. As the beta decay is  $Q$ -value limited, the strength at high energies cannot be observed. Another explanation for the quenching is a possible excitation of a nucleon into a  $\Delta$  resonance [Tow79]. The particle-hole configurations of the GT strength can be coupled with  $\Delta$ -hole excitations which lie about 300 MeV above the normal energy region for the GT strength. Thus, the part at that high-energy region cannot be detected in beta-decay experiments. Recently, a relativistic description of nuclei has shown that the total GT strength is reduced by about 12 % compared to the non-relativistic description [Kur03]. The reduction is due to antinucleon degrees of freedom.

The quenching factor  $q$  is the square root of the ratio of the experimental measured rate to the calculated rate. It has been calculated as  $q = 0.77(2)$  for the  $sd$ -shell [Wil83] and  $q = 0.744(15)$  for the  $pf$ -shell nuclei [Mar96]. Thus, the observed strength is about 60 % of the expected strength for the  $sd$ -shell nuclei and about 55 % for the  $pf$ -shell nuclei. It has been widely discussed whether this quenching is due to non-nucleonic renormalization of  $g_A$  or nuclear renormalization of  $\sigma\tau$ . In Caurier *et al.* [Cau05], the renormalization of the axial-vector constant  $g_A$  is ruled out. The results for  $M1$  transitions from the  $(p, p')$ ,  $(\gamma, \gamma')$  and  $(e, e')$  experiments, in which the constant  $g_A$  does not play a role, are quenched by a factor of 0.75 compared to the full  $pf$ -shell calculations for the  $N = 28$  isotones.

## 2.2.4 Charge-exchange reactions and the GT strength

Gamow-Teller transitions can also be studied via charge-exchange (CE) reactions, such as  $(p, n)$  or  $({}^3\text{He}, t)$  (see, *e.g.*, [Ost92] and [Rap94]). As the CE reactions are not  $Q$ -value limited, GT strengths over a broad energy range can be obtained. The determination of the GT strength is based on a proportionality between the  $B(\text{GT})$  and the CE reaction cross sections at  $0^\circ$  and at intermediate energies of above 100 MeV/nucleon [Goo80]:

$$\frac{d\sigma_{CE}}{d\Omega}(0^\circ) \approx KN_{\sigma\tau}|J_{\sigma\tau}(0)|^2 B(\text{GT}) \approx \hat{\sigma}_{GT} B(\text{GT}) \quad (2.17)$$

where  $K$  is the kinematic factor,  $N_{\sigma\tau}$  is a distortion factor,  $J_{\sigma\tau}(0)$  is the volume integral of the effective interaction  $V_{\sigma\tau}$  at momentum transfer  $q=0$  and  $\hat{\sigma}_{GT}$  is a unit cross section for the GT transition.

GT transitions are favored against Fermi transitions at intermediate energies. The forward angles around  $0^\circ$  are chosen due to the  $\Delta L = 0$  nature of the GT transitions. In order to identify the  $L = 0$  GT states, spectra at different angle cuts can be compared. As the angle increases, the cross sections for  $L = 0$  states decreases whereas for  $L = 1$  and other states the cross sections increase. The proportionality is valid only for allowed GT transitions. With small  $B(\text{GT})$  values, the  $0^\circ$  cross sections of  $l$  forbidden transitions can be enhanced [And96].

Previously, CE reactions have suffered from a poor energy resolution and identification of individual states has been difficult. In the early (p,n) reactions, the energy resolution was about 200–300 keV in neutron-time-of-flight systems [Rap83]. Fujita *et al.* have successfully used ( $^3\text{He},t$ ) CE reactions to study GT strength at the Grand Raiden spectrometer at RCNP. In these experiments, the momenta of tritons can be measured precisely by a magnetic spectrometer. As the incoming  $^3\text{He}$  beam has a much smaller bending radius than tritons, the beam can be stopped in a Faraday cup inside the spectrometer. The tritons are detected by multi-wire drift-chambers. Dispersion matching and angular dispersion matching techniques [Fuj97] and the over-focus mode of the spectrometer [Fuj01] have provided an energy resolution of about 35 keV [Fuj04].

The GT strength obtained from CE reactions is a useful tool in the studies of isospin symmetry. The strength can be compared to the strength from an analogous beta decay. For example, transitions between mirror nuclei ( $T_Z = \pm\frac{1}{2}$ ) should be analogous. This mirror symmetry has been studied for various pairs of  $sd$ -shell nuclei, such as  $^{27}\text{Al} - ^{27}\text{Si}$  [Fuj99] and  $^{23}\text{Na} - ^{23}\text{Mg}$  [Fuj02a]. Isospin symmetry of transitions has also been studied in  $T = 1$  isospin triplets, where the transitions  $T_Z = \pm 1 \rightarrow T_Z = 0$  should be analogous. Only a few studies on  $sd$ -shell nuclei, such as on the  $A = 26$  [Fuj03] and  $A = 38$  [And96] isobar triplets have been performed. Recently, experiments on  $pf$ -shell nuclei, such as on  $A = 50$  [Fuj05] and  $A = 58$  [Fuj02b, Fuj06] triplets, have been performed. Isospin studies can be extended further to isobaric quartets in which one can compare the GT-strengths of the transitions  $T_Z = \pm\frac{3}{2} \rightarrow T_Z = \pm\frac{1}{2}$ . An example of this kind of study is the  $A = 41$  isobar quartet [Fuj04].

The  $A = 58$  triplet,  $^{58}\text{Ni}$  ( $T_Z = 1$ ),  $^{58}\text{Cu}$  ( $T_Z = 0$ ) and  $^{58}\text{Zn}$  ( $T_Z = -1$ ), is of special interest in this thesis work (see fig. 2.3). Namely,  $B(\text{GT})$  results from the beta decay of  $^{58}\text{Zn}$  can be compared to the values from  $^{58}\text{Ni}(^3\text{He},t)^{58}\text{Cu}$  CE-reactions. The proportionality of the  $B(\text{GT})$  values in the CE-reactions can be calibrated with the ground state beta decay of  $^{58}\text{Cu}$  [Per01b, Jan01]. This allows a detailed comparison

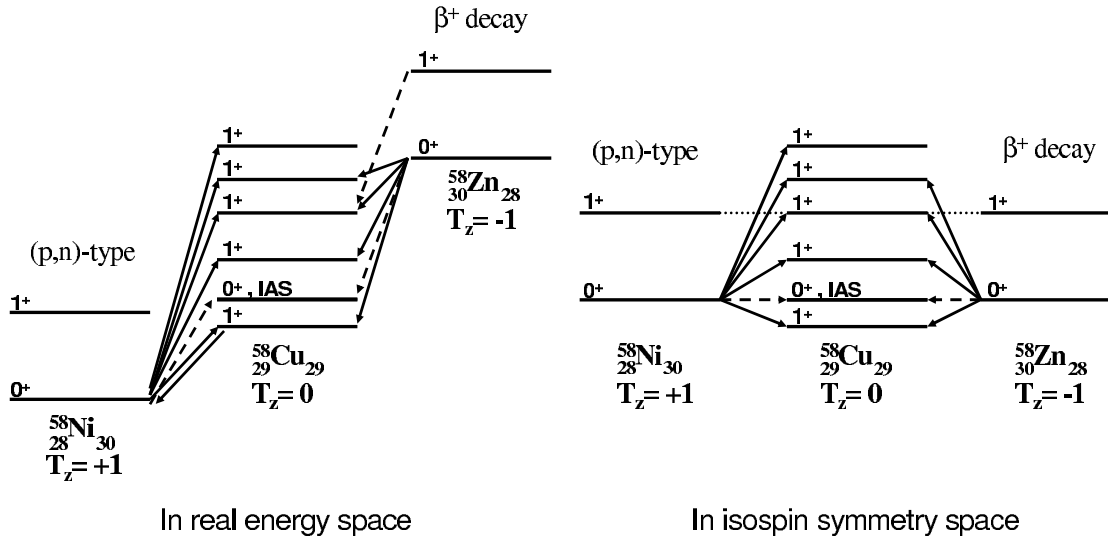


**Figure 2.3:** A schematic view of symmetric transitions in the  $T = 1$  triplet at  $A = 58$  in the real energy space and in the isospin symmetry space where the Coulomb displacement energy and the proton-neutron mass difference have been taken into account. Beta decay of  $^{58}\text{Cu}$  can be used to normalize the GT strength of the  $^{58}\text{Ni}_{g.s.}$  to  $^{58}\text{Cu}_{g.s.}$  transition.

of the GT strengths of the analogous transitions from  $^{58}\text{Zn}$  to  $^{58}\text{Cu}$  and from  $^{58}\text{Ni}$  to  $^{58}\text{Cu}$ .

## 2.2.5 Beta-delayed decay modes

Beta decay  $Q$ -values increase rapidly when moving from the valley of stability towards more neutron-deficient nuclei. At the same time, protons become less and less bound in the nuclei due to Coulomb repulsion. Thus, a neutron-deficient nucleus can beta decay to excited states which are unbound against particle emission. Figure 2.4 shows a schematic view of a beta decay of a neutron-deficient nucleus (precursor) to its daughter (emitter) which can further decay by emitting beta-delayed protons. The states above the proton separation energy  $S_p$  are unbound against proton emission. Also alpha emission (above the alpha separation energy) and emission of two protons can be energetically possible for some nuclei.

As the proton emission is a strong-interaction process, it is much faster than a decay with electromagnetic radiation. However, gamma-ray emission from excited states above the proton separation energy is possible, if the particle emission is delayed by Coulomb and angular-momentum barriers. The competition of different decay modes can be estimated with partial decay widths  $\Gamma_i$ . According to Heisenberg's uncertainty principle, the lifetime of a level is inversely proportional to its width. In other words, the partial decay width  $\Gamma_i$  is proportional to the partial decay constant  $\lambda_i$ . The in-

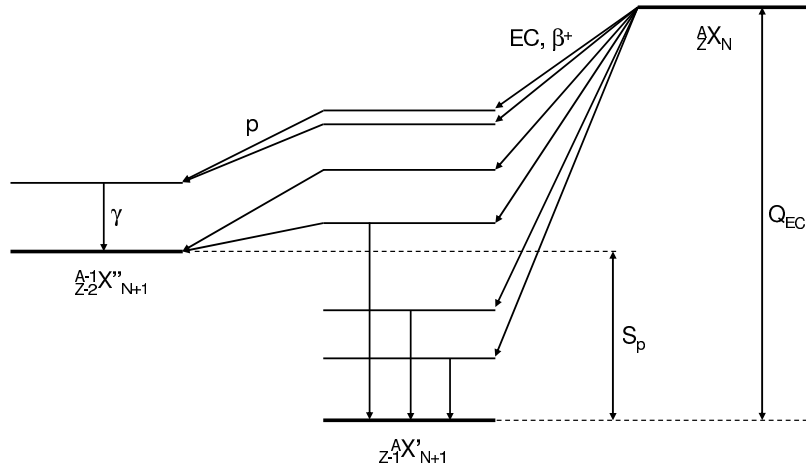


**Figure 2.4:** A schematic view of beta-delayed proton emission. The beta decay of the precursor  ${}^A_{Z-1}X'_N$  populates states in the emitter  ${}^A_{Z-1}X'_{N+1}$ . The excited states above the proton separation energy ( $S_p$ ) in the emitter decay to the states in the daughter nucleus  ${}^{A-1}_{Z-2}X''_{N+1}$  by emitting protons.

tensity of a beta-delayed proton peak is thus determined by the beta-decay branching ratio to a state  $i$  in the emitter ( $I_\beta^i$ ), the partial width for proton emission from the state  $i$  to the final state  $f$  ( $\Gamma_p^{if}$ ) and the total decay width of the state  $i$  ( $\Gamma = \Gamma_p^i + \Gamma_\gamma^i$ ):

$$I_p^{if} = I_\beta^i \frac{\Gamma_p^{if}}{\Gamma_p^i + \Gamma_\gamma^i} \quad (2.18)$$

The IAS is located above the  $S_p$  in many proton-rich nuclei. Although this state is heavily populated in a beta decay, it is possible that the proton decay from the IAS is isospin-forbidden. As the strong interaction conserves parity and isospin, the parity of the final state must be  $\pi_f = \pi_i(-1)^l$  and the isospin must be  $T_f + T_p = T_i$  where  $i$  and  $f$  refer to initial and final states, respectively. Angular momentum  $l$  carried away by the proton must satisfy the rule:

$$|J_i - J_f| - s_p \leq l \leq |J_i - J_f| + s_p \quad (2.19)$$

where  $J_i$  and  $J_f$  are the spins of the initial and final states and  $s_p = 1/2$  is the spin of the proton.

An example of an isospin-forbidden proton emission is beta-delayed proton emission from the IAS ( $T = 3/2$ ) in a  $T_Z = -1/2$  nucleus. The resulting daughter nucleus has  $T_Z = 0$  and thus, the final state is most likely  $T = 0$ . Isospin-forbidden decays, observed for example in the beta decay of  ${}^{23}\text{Al}$  [Per00], can be explained by isospin mixing meaning that the IAS is a mixture of two states with the same  $J^\pi$  but different

$T$ . This kind of nuclei, such as  $^{23}\text{Al}$  [Per00],  $^{27}\text{P}$  [Äys85, Ogn96],  $^{31}\text{Cl}$  [Äys85] and  $^{35}\text{K}$  [Ewa80], have been extensively studied in the past.

Up to now, only proton emission following a beta decay has been discussed. The states below  $S_p$  can only decay via  $\gamma$ -ray emission. The selection rules for angular momentum and parity in gamma decay are:

$$|J_i - J_f| \leq L \leq J_i + J_f \quad (\text{no } L=0) \quad (2.20)$$

$$\Delta\pi = no : \quad \text{even electric, odd magnetic} \quad (2.21)$$

$$\Delta\pi = yes : \quad \text{odd electric, even magnetic} \quad (2.22)$$

where  $L$  is the multipolarity of the transition and  $\Delta\pi$  refers to the change in parity between the initial and final states. Decay constants for  $\gamma$ -decay can be estimated by single-particle shell-model estimates, so-called Weisskopf estimates.

Gamma rays cannot be emitted in monopole transitions ( $L = 0$ ). Those are only possible via *internal conversion* which is a process competing with the  $\gamma$ -ray emission. In internal conversion, the energy of the nuclear transition is given to an atomic electron, usually in the  $K$ -shell closest to the nucleus. The electron gains an energy of  $E_e = E_\gamma - B_e$  where  $E_\gamma$  is the transition energy and  $B_e$  the binding energy of the electron. Internal conversion is described with an internal conversion coefficient  $\alpha$  which defines the ratio of conversion electron and gamma decay rates (see eq. 2.23). The total transition rate takes into account both conversion and gamma decay rates (see eq. 2.24). The total internal conversion coefficient  $\alpha$  can be further divided into partial conversion coefficients representing conversion from different atomic shells,  $\alpha = \alpha_K + \alpha_L + \alpha_M + \dots$ .

$$\alpha = \frac{\lambda_e}{\lambda_\gamma} \quad (2.23)$$

$$\lambda_{tot} = \lambda_\gamma(1 + \alpha) \quad (2.24)$$

After internal conversion, the atom is left with a vacancy in one of the electronic shells. This vacancy is rapidly filled with an electron from higher shells, which is observed as characteristic X-ray emission or emission of Auger electrons. The probability for X-ray emission is called fluorescence yield  $\omega$  and it is defined as the ratio of X-rays

to the primary vacancies in the corresponding shell. The most commonly used is  $K$ -fluorescence yield  $\omega_K$  given in eq. 2.25. Auger yield is defined in a similar way as the ratio of Auger electrons to the primary vacancies in the corresponding shell.

$$\omega_K = \frac{I(KX - rays)}{I(K - holes)} \quad (2.25)$$

Internal conversion coefficients are larger with decreasing transition energy, increasing multipole degree  $L$  and increasing  $Z$ . Electron shell, electron binding energies and nuclear structure have also an effect on the internal conversion. In many cases electromagnetic transitions have mixed multipoles, such as  $M1 + E2$ . For a mixed transition, the internal conversion coefficient can be calculated from [Kan95]:

$$\alpha = \frac{\alpha_{ML} + \delta^2 \times \alpha_{E(L+1)}}{1 + \delta^2} \quad (2.26)$$

Typically a measured internal conversion coefficient  $\alpha_{exp}$  is used for computing the mixing ratio  $\delta^2 = I[E(L+1)]/I[M(L)]$  [Kan95]:

$$\delta^2 = \frac{\alpha_{ML} - \alpha_{exp}}{\alpha_{exp} - \alpha_{E(L+1)}} \quad (2.27)$$

Sometimes excited states are exceptionally long-lived when compared to a normal gamma emission half-life which is generally less than  $10^{-9}$  s. The decay of these states, called *isomeric (or metastable) states* or shortly *isomers*, is inhibited by nuclear structure effects. Isomers can beta decay, thus affecting the total lifetime of a beta-decaying nucleus. Properties of isomers, such as spins (usually deduced from multipolarity and internal conversion coefficients for an isomeric transition) and half-lives, are in many cases important for modeling nuclear synthesis in astrophysical sites.

## 2.3 Astrophysical motivation

Neutron-deficient nuclei close to the  $N = Z$  line are involved in the nucleosynthesis of heavier elements in hot and hydrogen-rich astrophysical environments, such as in X-ray bursts or novae. These processes are discussed in the following sections. *Rapid proton capture process* or briefly, *rp process* is described in detail in sec. 2.3.1. Hydrogen burning in novae has been discussed separately in sec. 2.3.2. An isomer  $^{81m}\text{Kr}$  observed as a byproduct in the experiment around the  $A = 80$  mass region

brought another astrophysical issue under consideration. Namely, the use of  $^{81}\text{Br}$  as a solar neutrino detector presented in sec. 2.3.3.

### 2.3.1 Rapid proton capture (rp) process

Hydrogen-rich compositions can enter into explosive hydrogen burning at high stellar temperatures above  $T=10^8$  K. The hydrogen burning occurs at lower temperatures via the hot carbon-nitrogen-oxygen (CNO) cycle and above  $T=3\times 10^8$  K via the rp process or  $\alpha p$  process [Sch98]. The rp process, a sequence of rapid proton captures and  $\beta^+$  decays, was first introduced by Wallace and Woosley [Wal81]. Reaction rates and the timescale of the rp and  $\alpha p$  processes were discussed for nuclei with  $Z \leq 32$  in [Wor94] and the nucleosynthesis of nuclei above  $Z = 32$  was reported in detail in [Sch98].

The rp process can occur at various astrophysical sites which have high enough temperatures and hydrogen densities. Already in [Wal81] supermassive stars ( $M/M_\odot \approx 10^5$ - $10^8$ ), accreting neutron stars, red giants with neutron star cores (Thorne-Zytkow objects), nova and supernova outbursts and dense, inhomogeneous cosmologies were suggested as possible rp-process sites. Later, the predictions have improved and for example Thorne-Zytkow objects are nowadays thought unlikely to form as they are gravitationally unstable, and thus not a proper astrophysical site for the rp process [Sch98]. Recently, accretion disks around black holes and neutron stars, type I X-ray bursts and novae have been considered as likely sites for the rp process [Sch98]. In this section the focus is on accretion on the surface of a neutron star (see, *e.g.*, [Sch98], [Sch01a], [Sch01b] and [Sch06]). Novae will be discussed in sec. 2.3.2.

Type I X-ray bursts occur in close binary systems where a neutron star accretes hydrogen and helium rich matter from the companion star. The matter accumulates on the surface for some hours or days and then burns explosively within 10-100 s, which is observed as a type I X-ray burst. If the matter is accreted at high accretion rates, the thermonuclear burning proceeds in steady-state. This can happen for example in X-ray pulsars where a strong magnetic field forces the accretion flow onto a small area around magnetic polar regions [Sch06].

The astrophysical site influences the flow of the rp process. For example, in novae, where temperatures are lower, the explosive hydrogen burning will end in the  $A \approx 40$  region [Wal81]. The hydrogen burning usually starts with a hot CNO-cycle the rate of which is limited by the slow  $\beta^+$  decays of  $^{14}\text{O}$  and  $^{15}\text{O}$ . The break-out from the CNO-cycle can occur at temperatures around  $6\times 10^8$  K via  $^{15}\text{O}(\alpha,\gamma)^{19}\text{Ne}$  and  $^{18}\text{Ne}(\alpha,p)^{21}\text{Na}$  [Wie99]. At lower temperatures,  $^{18}\text{Ne}$   $\beta^+$  decays and is processed back to  $^{15}\text{O}$ . At high enough temperatures,  $^{19}\text{Ne}(p,\gamma)^{20}\text{Na}$  can occur and after that, the matter cannot return back to the main hot CNO-cycle loop. The reaction  $^{19}\text{Ne}(p,\gamma)^{20}\text{Na}$  serves as a

link from the CNO-cycles to the Ne-Na cycle and further to the rp process [Wie99]. In X-ray bursts, the thermonuclear runaway is triggered by the  $3\alpha$  reaction which is strongly temperature-dependent in contrast to the  $\beta$ -limited CNO-cycle. The break-out from the CNO-cycle occurs via  $^{14}\text{O}(\alpha,p)$  and  $^{18}\text{Ne}(\alpha,p)$ . The thermonuclear runaway proceeds via the  $\alpha p$  process, a sequence of  $(\alpha,p)$  and  $(p,\gamma)$  reactions up to  $^{41}\text{Sc}$ . The  $\alpha p$  process provides seed nuclei for the rp process which then continues up to  $^{56}\text{Ni}$  and further in optimal conditions.

The path and timescale of the rp process depend on the beta-decay lifetimes, proton capture and photodisintegration  $(\gamma,p)$  rates and the respective  $Q$ -values, *i.e.* the masses. The rp process is modeled with nuclear reaction network calculations which provide information on isotopic abundances and nuclear energy generation during the process. The calculations depend strongly on temperatures and densities. Whereas beta decays are (almost) temperature independent, proton captures are hindered by the Coulomb barrier at low energies and by photodisintegration at higher temperatures. For beta decays, the decay from thermally populated excited levels at high stellar energies and the enhancement of the electron capture rates due to continuum electron captures at high stellar densities have to be taken into account [Sch98].

The network calculations are based on available experimental data and the rest is theoretically modeled. Typically, the cross sections of particle-induced reactions are estimated with a statistical model of compound reactions (Hauser-Feshbach). The statistical model is applicable for high level densities, which is true for the rp-process nuclei above  $A = 40$  [Sch98]. For lower-mass nuclei and near the drip line or closed shells, the level densities are quite low and reaction cross sections are dominated by single resonances and direct capture contributions. In order to estimate these proton capture rates depending exponentially on the resonance energies, the masses and excitation energies should be known better than 10 keV [Sch06]. Figure 2.5 shows time integrated reaction flow above Ga during an X-ray burst and for steady state burning where the theoretical reaction rates have been calculated with a Hauser-Feshbach based code SMOKER [Sch01a]. As it can be seen from fig. 2.5, almost all nuclei studied in this thesis are involved in the rp process. For example, the rp-process path proceeds via the beta decay of  $^{58}\text{Zn}$  through  $^{69}\text{Kr}$  and further to the mass  $A \approx 80$  region.

The rp process above  $A = 40$  is described by fast proton captures  $(p,\gamma)$  until they are inhibited by  $p$  decay (negative  $Q$  value) or by photodisintegration (low  $Q$  value) [Sch98]. In these situations, the reaction flow has to wait for slow  $\beta^+$  decay and the rp process is hindered for some time. These types of nuclei which cannot proceed by proton captures but decay slowly via  $\beta^+$  decay, are called *waiting points* of the rp process. These waiting points determine entirely the speed of the nucleosynthesis and isotopic abundances in the process and are thus of special interest. Usually waiting-point nuclei have even- $Z$  as the odd- $Z$  nucleus following a proton capture is not so well-bound.

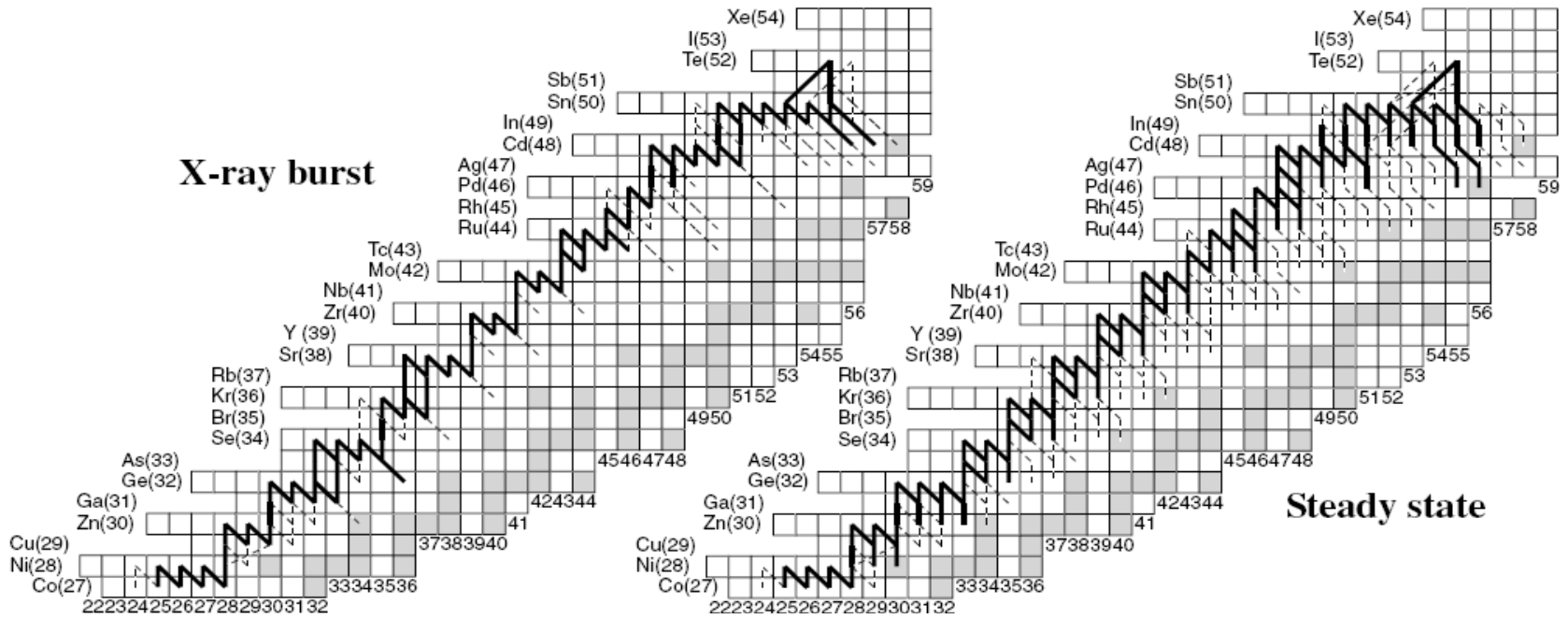


**Figure 2.5:** The path of the rp process above Ga for X-ray bursts and for steady state burning from ref. [Sch01a]. Time-integrated reaction flows of more than 10 % are shown by a solid line and the flows of 1 %–10 % by a dashed line.

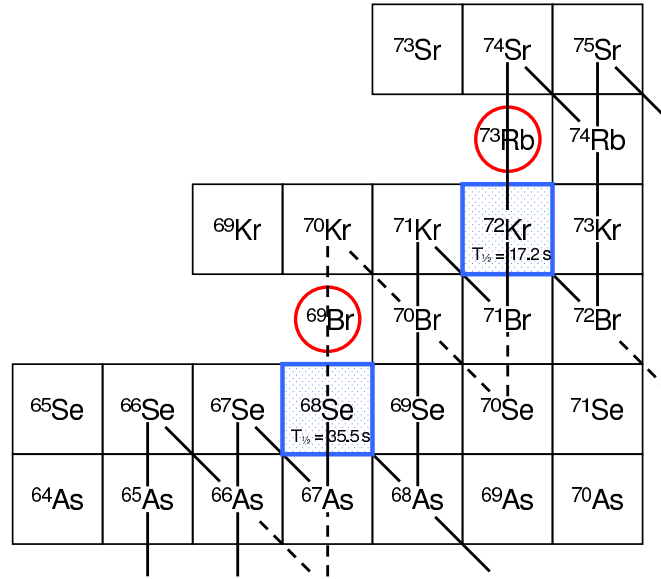


**Figure 2.6:** Two-proton captures on  $^{68}\text{Se}$  and  $^{72}\text{Kr}$ . Although  $^{69}\text{Br}$  and  $^{73}\text{Rb}$  are expected to be proton-unbound,  $2p$ -captures may be possible. If this is not the case, the rp process is forced to wait for the slow beta decays of  $^{68}\text{Se}$  ( $T_{1/2}=35.5 \text{ s}$ ) and  $^{72}\text{Kr}$  ( $T_{1/2}=17.2 \text{ s}$ ).

Rather long-lived even-even  $N = Z$  waiting-point nuclei  $^{56}\text{Ni}$ ,  $^{64}\text{Ge}$ ,  $^{68}\text{Se}$  and  $^{72}\text{Kr}$  determine the time needed to reach the region above Kr [Sch98]. However, the reaction flow can be substantially enhanced at high temperatures and densities where two-proton ( $2p$ ) captures can be significantly faster than the competing  $\beta^+$  decay. Figure 2.6 represents two-proton captures on  $^{68}\text{Se}$  and  $^{72}\text{Kr}$  which are the only nuclei for which the  $2p$ -capture may play a significant role [Sch98]. The total lifetime of these nuclei can be calculated from  $2p$ -capture rates and  $\beta^+$  decay lifetimes. At high temperatures of about 1.5–2 GK, photodisintegration causes a strong inverse  $2p$  capture rate and nuclei  $(Z, N)$  and  $(Z+2, N)$  are in equilibrium. In this case, the total lifetime of the waiting point is determined by the beta decays of  $(Z, N)$  and  $(Z+2, N)$ . Thus, the lifetime depends on temperature, density, nuclear masses and beta-decay rates but not on the  $p$ -capture rate. At lower temperatures, the total lifetime is determined by the beta decay of the waiting-point nucleus  $(Z, N)$  and the  $2p$ -capture rate.

In order to determine the lifetime of a waiting-point nucleus  $(Z, N)$ , the binding energy of the  $(Z+1, N)$  nucleus must be known. As the proton separation energy of  $^{69}\text{Br}$  or  $^{73}\text{Rb}$  corresponds to the proton capture  $Q$  value for the reactions  $^{68}\text{Se}(p, \gamma)^{69}\text{Br}$  or  $^{72}\text{Kr}(p, \gamma)^{73}\text{Rb}$  ( $S_p = -Q_p$ ), the proton separation energies for  $^{69}\text{Br}$  and  $^{73}\text{Rb}$  are essential for the estimation of the lifetimes of  $^{68}\text{Se}$  and  $^{72}\text{Kr}$ . Mohar *et al.* could identify  $^{69}\text{Br}$  in the projectile fragmentation of  $^{78}\text{Kr}$  [Moh91]. After that, several attempts have been made to measure these binding energies [Bla95a, Jok96, Pfa96, Lim02] but no events belonging to  $^{69}\text{Br}$  or  $^{73}\text{Rb}$  have been found. Some predictions on the proton separation energy of  $^{69}\text{Br}$  have been performed. In ref. [Bla95a] an upper limit of 100

ns was given for the half-life of  $^{69}\text{Br}$ , which suggests that  $^{69}\text{Br}$  is proton-unbound by at least 450 keV. Similarly, an upper limit of 30 ns for the half-life of  $^{73}\text{Rb}$  was obtained in [Pfa96], which indicates that  $^{73}\text{Rb}$  is proton-unbound by at least 680 keV. Recently, mass measurements of  $^{68}\text{Se}$  have provided new input data for the estimation of the  $S_p$  value of  $^{69}\text{Br}$  [Cla04, Wöh04]. The estimated proton separation energies have been collected in table 2.1. Although  $^{69}\text{Br}$  and  $^{73}\text{Rb}$  are expected to be proton-unstable, the lifetimes can be long enough due to the Coulomb barrier and the rp process may proceed via  $2p$ -captures in X-ray burst conditions. In addition, the low-energy  $0^+$  shape isomer in  $^{72}\text{Kr}$  and expected similar shape isomer configurations in  $^{68}\text{Se}$  may enhance the proton capture rates significantly [Wie05].

**Table 2.1:** Estimations on the proton separation energies  $S_p$  for  $^{69}\text{Br}$  and  $^{73}\text{Rb}$ .

Nuclide	$S_p$ (keV)	Reference
$^{69}\text{Br}$	$< -450$	From the upper limit of $\tau$ [Bla95a]
$^{69}\text{Br}$	$-730(320)$	Theoretical [Bro02]
$^{69}\text{Br}$	$-450(100)$	AME-2003 [Aud03b]
$^{69}\text{Br}$	$-766(350)$	$\beta$ -decay [Wöh04]
$^{69}\text{Br}$	$-809(130)$	Penning trap [Cla04]
$^{73}\text{Rb}$	$< -680$	From the upper limit of $\tau$ [Pfa96]
$^{73}\text{Rb}$	$-550(320)$	Theoretical [Bro02]
$^{73}\text{Rb}$	$-600(150)$	AME-2003 [Aud03b]

Despite the waiting points slowing down the rp process, large amounts of  $A = 80 - 100$  nuclei can be produced in typical X-ray bursts with densities of about  $10^6 \text{ g/cm}^3$  and temperatures between 1 and 2 GK [Sch98]. The next bottleneck after  $^{72}\text{Kr}$  occurs in the  $A = 80$  region (see fig. 2.7) where the calculated  $\alpha$  separation energies are very low. The nucleus  $^{84}\text{Mo}$  is even predicted to be  $\alpha$ -unbound, which can increase the  $^{83}\text{Nb}(p,\alpha)^{80}\text{Zr}$  rate considerably. At energies of about 1.5 GK, only a few percent of the reaction flow is processed via the  $^{83}\text{Nb}(p,\alpha)^{80}\text{Zr}$  reaction [Sch98]. The situation changes dramatically above 2 GK, when almost all material is processed back to  $^{80}\text{Zr}$  [Sch98]. The material is then stored in a Zr-Nb cycle (see eq. 2.28). After a while, the material will be converted into  $^{80}\text{Zr}$  and  $^{81}\text{Zr}$ , which have the slowest  $\beta^+$  decays in the cycle. The rapid changes in nuclear structure in this region make the extrapolation of masses and prediction of half-lives difficult as demonstrated in refs. [Sch98, Res00] for  $^{80}\text{Zr}$ . Also the isomers in the mass region around  $A = 80$  have to be taken into account in the network calculations. If the isomeric state has a different  $\beta^+$  lifetime compared to the ground state, the total lifetime can change considerably. Proton captures on isomeric states are also possible and can enhance total proton capture rates.

$$^{83}\text{Nb}(p, \alpha)^{80}\text{Zr}(\beta^+)^{80}\text{Y}(p, \gamma)^{81}\text{Zr} \left\{ \begin{array}{l} (\beta^+)^{81}\text{Y}(p, \gamma) \\ (p, \gamma)^{82}\text{Nb}(\beta^+) \end{array} \right\} ^{82}\text{Zr}(p, \gamma)^{83}\text{Nb} \quad (2.28)$$

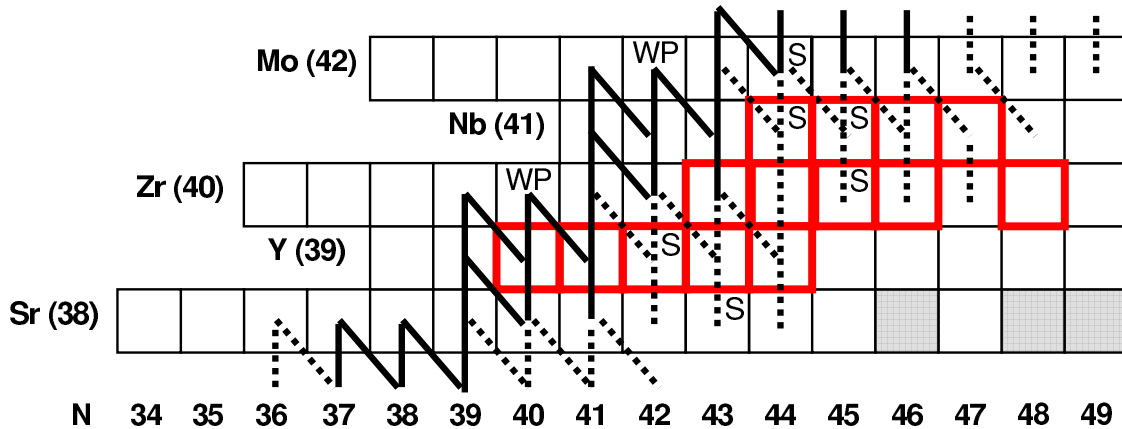


**Figure 2.7:** The rp process around the mass  $A = 80$  region for steady-state burning [Sch01b]. The reaction flow of more than 10 % is shown by the solid line and that of 1–10 % by the dashed line. The nuclei whose masses were measured in this work are highlighted by squares. The nuclei studied spectroscopically are marked with 'S' and the waiting-point nuclei  $^{80}\text{Zr}$  and  $^{84}\text{Mo}$  are labeled as 'WP'.

The end point of the rp process path has been explored in refs. [Sch01a] and [Sch01b]. The calculations show that the rp process can reach  $^{99-101}\text{Sn}$  isotopes in about 80 s after an X-ray burst peak. After that, the process proceeds towards more stable Sn isotopes until it reaches  $^{105}\text{Sn}$  at which a proton capture to  $^{106}\text{Sb}$  is possible. The process is stopped at  $^{107}\text{Te}$  following a proton capture on  $^{106}\text{Sb}$ . Namely, a strong photodisintegration rate of  $^{107}\text{Te}(\gamma, \alpha)^{103}\text{Sn}$  cycles the material back to  $^{103}\text{Sn}$ . The rp process flow cannot proceed beyond this SnSbTe-cycle in X-ray bursts or in steady-state burning due to  $\alpha$ -unbound  $^{106-108}\text{Te}$  isotopes. The SnSbTe-cycle affects the final abundance distribution and hydrogen consumption in the rp-process and leads to an increased energy generation. A factor of two in energy release is predicted if the rp process ends in the  $A = 80 - 100$  region instead of the Kr region [Sch98]. In the final abundance distribution, an overproduction of  $p$ -nuclei  $^{98}\text{Ru}$ ,  $^{102}\text{Pd}$  and  $^{106}\text{Cd}$  is obtained. However, this may not explain the origin of  $p$ -nuclei in the Universe because only a fraction of X-ray bursts can produce these nuclei. A so-called  $\nu p$ -process [Frö06] occurring in supernovae and possibly in gamma-ray bursts has also been proposed to explain the solar abundances of  $^{92,94}\text{Mo}$  and  $^{96,98}\text{Ru}$ . In this process, antineutrinos absorbed in a proton-rich environment produce neutrons that are immediately captured by neutron-deficient nuclei allowing a nucleosynthesis of elements with  $A \geq 64$ .

### 2.3.2 Nucleosynthesis in novae

In a nova, thermonuclear runaway occurs in the accreted envelope of a white dwarf in a binary system consisting of a white dwarf and a large main-sequence star. Hydrogen-rich matter from the main-sequence companion is transferred to the surface of the

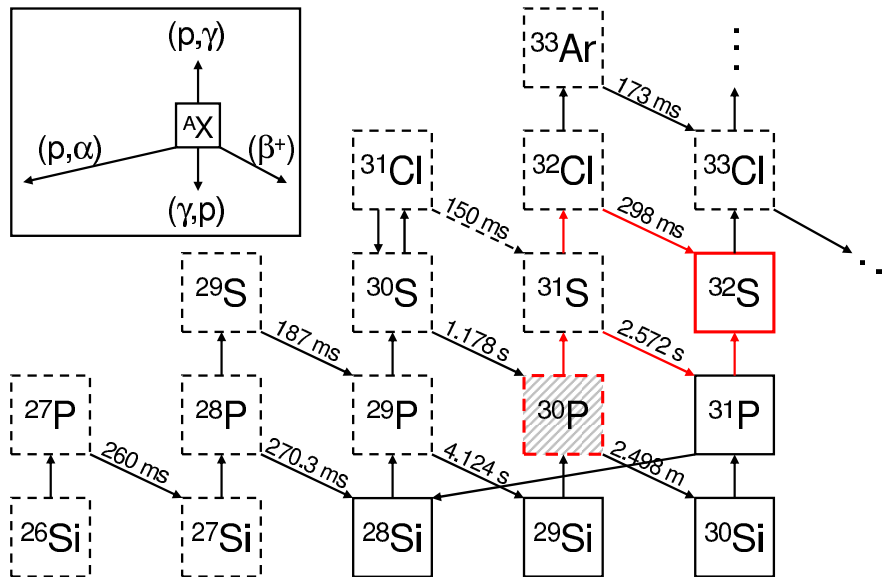


**Figure 2.8:** Nucleosynthesis in ONe novae.

white dwarf forming an ocean of hydrogen on the surface. As the accretion continues, the matter is compressed and heated so much that thermonuclear runaway is triggered. Finally, thermonuclear runaway will lead to a nova explosion in which the major part of the envelope is ejected. These explosions release huge amounts of energy and spread nuclear-processed material into the interstellar medium. Nova outbursts inject significant amounts of  $^{13}\text{C}$ ,  $^{15}\text{N}$  and  $^{17}\text{O}$  and also small amounts of other nuclei, such as  $^7\text{Li}$ ,  $^{19}\text{F}$  and  $^{26}\text{Al}$  [Jos05].

The thermonuclear runaway and the composition of the ejecta depend on the white dwarf type. The runaways are mainly powered by  $\beta^+$  decays of the short-lived  $^{13}\text{N}$ ,  $^{14,15}\text{O}$  and  $^{17}\text{F}$  nuclei produced in the hot CNO cycle. At nova peak temperatures of about  $T=3\times 10^8$  K, there is not enough energy to break-out from the CNO cycle towards heavier ( $A \geq 20$ ) elements. Instead, the nucleosynthesis can proceed via proton captures and  $\beta^+$  decays on seed nuclei available on the white dwarf, such as  $^{20}\text{Ne}$  in oxygen-neon (ONe) white dwarfs. Nuclear activity can go up to silicon in  $1.15 M_{\odot}$  ONe novae and up to argon in  $1.35 M_{\odot}$  ONe novae [Jos05] which contain not only CNO-group nuclei but also neon, sodium, aluminum and other intermediate-mass nuclei. Carbon-oxygen (CO) white dwarfs are less massive and contain CNO group nuclei due to which the nuclear activity does not extend much beyond oxygen [Jos05].

Nova outbursts have been modeled with a hydrodynamic code called SHIVA with an updated nuclear reaction network [Jos99, Jos01]. Proton captures on the seed nuclei in the NeNa-MgAl region [Jos99] drive the nuclear activity up to the Si-Ca mass region [Jos01]. The end point of nova nucleosynthesis is limited below the mass  $A = 40$  region [Jos05]. The most crucial point of the nucleosynthesis occurs at  $^{30}\text{P}$ . Namely,

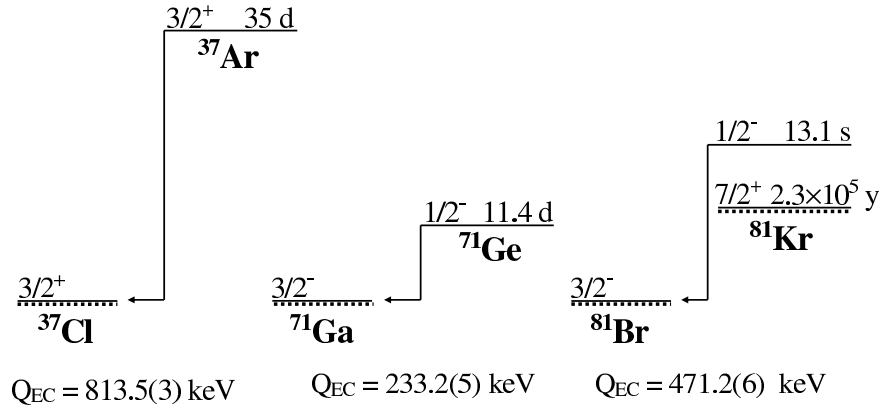


**Figure 2.9:** Isotopes proposed for solar neutrino detectors.

species beyond sulfur are produced via two paths, either  $^{30}\text{P}(p,\gamma)^{31}\text{S}(p,\gamma)^{32}\text{Cl}(\beta^+)^{32}\text{S}$  or  $^{30}\text{P}(p,\gamma)^{31}\text{S}(\beta^+)^{31}\text{P}(p,\gamma)^{32}\text{S}$  (see fig. 2.8). Thus,  $^{30}\text{P}$  is a mandatory passing point and it stops further nucleosynthesis unless proton captures to the states of  $^{31}\text{S}$  are fast enough. Therefore, the properties of the excited states in  $^{31}\text{S}$  are important for the studies of the nucleosynthesis in oxygen-neon (ONe) novae [Jos99, Jos01, Jos06].

Although several excited states above the proton separation energy in  $^{31}\text{S}$  have been measured quite accurately, the spins and the decay widths are not known so well. The reaction rate of  $^{30}\text{P}(p,\gamma)$  has been calculated using a statistical model calculation [Rau00]. However, this model requires a relatively high level density and thus, it may not work for a light nucleus such as  $^{30}\text{P}$  at low temperatures. Most likely single resonances and direct captures will dominate the reaction rate [Jos01]. In order to calculate the reaction rate for individual resonances, corresponding resonance energies, spins of the final states and proton and gamma decay widths should be known. Therefore, more spectroscopic information are needed. José *et al.* have emphasized the importance of this reaction rate and the effects of its uncertainty in ONe novae [Jos01]. If the rate is much higher than estimated, far less  $^{30}\text{Si}$  is left in the envelope of a nova. On the other hand, if the rate is much lower, it will lead to an enhancement of  $^{30}\text{Si}$  as the slow beta decay of  $^{30}\text{P}$  can compete favorably against proton captures. This will reduce the yields of nuclei above  $^{32}\text{S}$  significantly. The abundance pattern is important as it gives information on the underlying white dwarf and can explain nova origin of presolar grains and  $\gamma$ -rays observed from nova outbursts [Jos01].

### 2.3.3 $^{81}\text{Br}$ as a solar neutrino detector

Another astrophysical issue related to this thesis work is solar neutrino detection which evolved as a byproduct from an experiment where the properties of  $^{81m}\text{Kr}$  relevant for  $^{81}\text{Br}$  solar neutrino detector could be studied. After the experiment using the  $^{37}\text{Cl}$

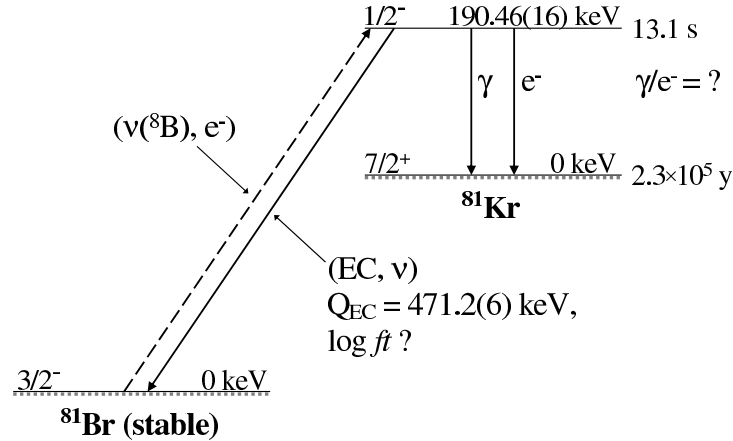


**Figure 2.10:** The principle of an  $^{81}\text{Br}$  solar neutrino detector.

detector [Dav68] had shown the discrepancy between expected and experimental solar neutrino fluxes, other detectors (see fig. 2.9), such as  $^{81}\text{Br}$  [Sco76], were proposed to measure the flux for lower neutrino energies. Although the solar neutrino flux puzzle has been explained by neutrino oscillations, more solar neutrino experiments are required to measure the CNO fusion cycle contribution in the solar luminosity and new types of detectors are desirable. According to current solar model calculations, 98.5 % of the solar luminosity is provided by the p-p chain and only 1.5 % by CNO reactions. At the moment, solar neutrino experiments have only set an upper limit of 7.8 % to the CNO fraction of the Sun's luminosity [Bah03].

It is assumed that a  $^{81}\text{Br}$  detector is most sensitive to  $^8\text{B}$  neutrinos [Kro87] but  $^7\text{Be}$  neutrinos as well as neutrinos from  $^{13}\text{N}$  and  $^{15}\text{O}$  decays from the CNO cycle can also contribute. In radiochemical experiments  $^{81}\text{Br}$  can be used for total solar neutrino flux measurements because its energy threshold allows the observation of neutrino-induced events from all main solar neutrino sources mentioned above. Meanwhile, a detailed investigation of Gamow-Teller and Fermi transition strengths for all allowed transitions from  $^{81}\text{Br}$  to the states below the particle emission threshold in  $^{81}\text{Kr}$  is needed to calculate contributions of different neutrino components [Kro87].

In order to obtain the neutrino capture cross section on  $^{81}\text{Br}$ , the probability for the inverse process of electron-capture (EC) of  $^{81}\text{Kr}$  must be measured. As shown in fig. 2.10, the neutrino capture on  $^{81}\text{Br}$  should predominantly populate the isomeric state at 190.5 keV in  $^{81}\text{Kr}$  because this allowed transition has to be six orders of magnitude stronger than the capture to the ground state of  $^{81}\text{Kr}$ , whose inverse rate is well known [Bag96]. Thus, the rates for all decay branches of  $^{81m}\text{Kr}$  (EC, internal conversion and  $\gamma$ -decay) are needed for the EC probability. The data for the  $K$ -electron capture channel, determined independently by two groups [Low87, Dav87], are in satisfactory agreement but the information on the internal transition is controversial. Therefore, the EC branching ratio has not been obtained with high accuracy.

# 3 Experimental method

## 3.1 Isotope Separator On-Line (ISOL) facilities

Exotic nuclei studied in this thesis were produced with the Isotope Separator On-Line (ISOL) method. In this method the isotopes of interest are produced by an ion beam hitting a target, after which the produced nuclei are stopped, ionized, accelerated to a few tens of keV and mass-separated in a continuous way on-line. The ISOL facilities used in this work, the Ion-Guide Separator On-Line (IGISOL) in Jyväskylä and the ISOLDE facility at CERN are described below. The main difference between these facilities is that ISOLDE uses thick targets in which the produced nuclei are stopped and an ion source is mandatory whereas IGISOL uses thin targets and the products are stopped in a helium gas cell after which most of the ions are in a charge state +1. Thus, no separate ion source is needed.

### 3.1.1 ISOLDE

The ISOLDE facility (see reviews [Jon00] and [Äys04]) is located at the CERN PS Booster which is a stack of four small synchrotrons [Kug00]. The PS Booster pre-accelerates protons from a linear accelerator to 1 GeV or to 1.4 GeV before an injection to CERN Proton Synchrotron (PS), which delivers protons to CERN's high energy experiments. The protons are delivered in pulses which have a particular time structure. A pulse with a maximum amount of  $3.2 \times 10^{13}$  protons is ejected out of the PS Booster in  $2.4 \mu\text{s}$  once in every 1.2 seconds. About six pulses in a normal PS supercycle of 14.4 s ( $12 \times 1.2$  s) is injected to ISOLDE which yields an average current of  $2.1 \mu\text{A}$  on the target. These short intense pulses might break down normal high voltage supplies and, therefore, the accelerating 60 kV high voltage is switched off  $35 \mu\text{s}$  before the beam impact and it is back on at original value after 5 ms.

The radioactive nuclei studied in this work were produced by spallation reactions induced by a 1.4 GeV proton beam in a thick target. A large variety of nuclei with a mass lower than the atomic mass of the target can be produced via spallation in which the target nuclei are broken into smaller nuclei, neutrons and other particles. The produced nuclei must diffuse from the target material and effuse out to an attached ion source which ionizes the products [Let97]. The target is resistively heated in order

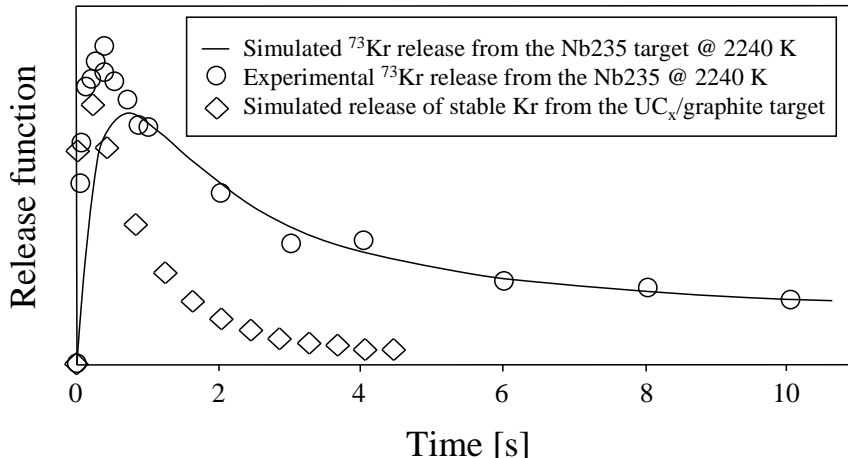


**Figure 3.1:** Release of Kr from Nb and  $UC_x$ /graphite targets. The data has been corrected for the decay of  $^{73}\text{Kr}$ . The simulations are based on a Monte Carlo code (see sec. 4.3).

to keep the reaction products volatile for fast release. The heating and diffusion sets limits for the targets and produced nuclei. Elements with high melting points, such as refractory elements, cannot be efficiently released at the temperatures suitable for the targets. Other disadvantages of thick targets are that several elements are too volatile and enriched targets are too expensive [Kös02a]. In addition, intense proton pulses stress the target so much that the yields decrease remarkably in a week or in a fortnight [Kös02a].

The losses occurred in the diffusion and effusion processes are described by a release function. It has usually a sharp rise followed by a steep fall and ending with a tail (see fig. 3.1). The release function is given in eq. 3.1, where  $N$  is a normalization factor,  $\alpha$  is the fast fraction of the release function and  $\lambda_r$ ,  $\lambda_f$  and  $\lambda_s$  stand for rise, fast and slow fall decay constants, respectively [Let97]. The decay losses are independent of the release process and the overall probability for an atom to survive from the decay and release is given by eq. 3.2, where  $\lambda_i$  is a decay constant for an isotope  $i$ . Release behavior can be measured with a beta counter and half-life detection. The release efficiency (released fraction) is the fraction of the produced atoms which have been released from the target and survived to the ion source. This can be calculated by integrating the overall probability density from zero to infinity.

$$P(t) = \frac{1}{N} \times (1 - e^{-\lambda_r t})(\alpha e^{-\lambda_f t} + (1 - \alpha)e^{-\lambda_s t}) \quad (3.1)$$

$$P(t, \lambda_i) = P(t)e^{-\lambda_i t} \quad (3.2)$$

The studied nuclides,  $^{58}\text{Zn}$  and  $^{69,71,73}\text{Kr}$  isotopes, were produced with a 1.4 GeV

proton beam on rolled 25  $\mu\text{m}$  thick Nb foil targets. For example, in order to produce krypton isotopes, 10 Nb foil rolls (diameter  $\approx 18$  mm, length  $\approx 15$  mm) spaced evenly using 3-mm-long spacers were put into a Ta target container. The target thickness was about 38 g/cm<sup>2</sup>. <sup>58</sup>Zn was produced with two identical targets with 10 rolls of Nb foil (diameter  $\approx 17$  mm, length  $\approx 17$  mm) in the experiment done in 2002. The targets had a thickness of about 40 g/cm<sup>2</sup> and the first target was changed to another target after the first week of the experiment. The targets were held at about 2100–2300 K and the transfer line at about 2400 K during the run. A released fraction of about 0.8 % was obtained for <sup>58</sup>Zn in this experiment. In the experiment done on <sup>58</sup>Zn in 2003, a target with 12 rolls of Nb foil and with a thickness of 54 g/cm<sup>2</sup> was used. Unfortunately, the temperature calibration of the target line was wrong and the experiment was run at too low temperatures which reduced the yields substantially. In addition, the proton beam from the PS Booster was too focused on the target which was not optimal for the production of radioactive isotopes.

The produced atoms were ionized in a separate ion source. As a noble gas, krypton is hard to be surface-ionized. Therefore, a plasma ion source with a water-cooled transfer line (MK7) was used to ionize the krypton isotopes [ISO06]. The transfer line was water-cooled in order to suppress the transport of less volatile elements and reduce the isobaric contamination. In the plasma ion source, electrons accelerated between the transfer line and the extraction electrode with an anode voltage of about 130 V ionize a gas mixture which then forms the plasma. A magnetic field is used to optimize this process. The ionization happens mainly by electron impact on the atoms. A gas mixture of He, Ne, Kr and Xe was used to optimize the Kr yields and an ionization efficiency of about 7.5 % was achieved. The target temperature was varied from about 2100 K to 2240 K and the transfer line was held at about 2300 K during the experiment.

The ionization of <sup>58</sup>Zn was done with the resonance ionization laser ion source (RILIS). The Zn yields are about 1–2 orders of magnitude higher with the RILIS than with a hot plasma ion source [Oin00]. In the RILIS method, the valence electron is resonantly excited by laser light into a continuum via several atomic levels. The laser system consists of dye lasers, copper vapor lasers (CVLs), nonlinear crystals and other optical elements. Three CVLs work with a repetition rate of 11 kHz and they can pump two or three dye lasers. Ultraviolet light needed for some transitions is obtained via frequency doubling or tripling. In the RILIS (see, *e.g.*, [Mis93],[Fed00],[Kös02b],[Fed03]), atoms are stored in a hot cavity for about 0.1 ms in order to gain a sufficient overlap in time and space with the pulsed lasers. Although laser ionization is very selective, a part of the atoms can be surface ionized in the hot cavity. For example in the case of <sup>58</sup>Zn, laser ionization reduces the contribution from the isobaric contaminants, <sup>58</sup>Cu and <sup>58</sup>Mn, but surface ionized <sup>58</sup>Mn is still clearly observed in the spectra.

The resonance ionization scheme for <sup>58</sup>Zn is shown in fig. 3.2. This three-step scheme

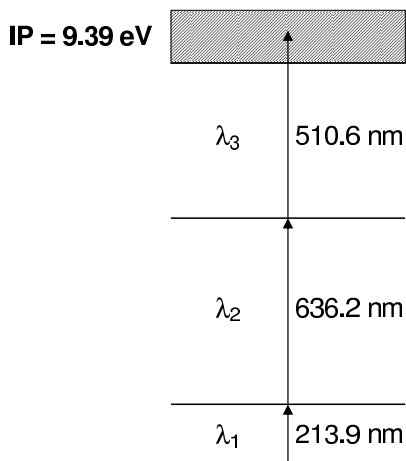


**Figure 3.2:** The resonance ionization scheme used for  $^{58}\text{Zn}$ . The strong ultraviolet transition is obtained with frequency tripling.

with an ionization efficiency of about 5 % was used for the first time in [Jok98]. In the beginning of the  $^{58}\text{Zn}$  experiment in 2002, only two dye lasers were used for the ionization. The frequency of the first laser was tripled for the first transition. The second and the third transition were obtained from the second dye laser. In the three color scheme, the third step into the continuum was achieved with 510.6 nm light from a CVL. The three step scheme was used from the middle of the experiment and it gave a 40 % increase in yield than the two color scheme. The two color scheme was chosen because it was more stable and only two beams had to be spatially aligned.

The ions were accelerated to 60 keV and guided to one of the mass separators at ISOLDE. The General Purpose Separator (GPS) has a  $70^\circ$  magnet with a bending radius of 1.5 m [Kug00]. It can serve a mass resolving power of about 2400. The GPS has an advantage that three different beams within a certain mass range can be delivered simultaneously into the experimental hall via three different beam lines (central mass, low mass and high mass beam lines). The other separator, High Resolution Separator (HRS) can achieve a resolving power of about 15 000 in a high resolution mode [Kug00] and it can routinely run with a mass resolution of 3000–4500 [Gil03]. It consists of two magnets with a bending radius of 1 m. The first magnet has a bending angle of  $90^\circ$  and the second magnet has an angle of  $60^\circ$ . Both separators were used in the experiments. The krypton isotopes were separated by the HRS. The  $^{58}\text{Zn}$  experiment was run with the HRS in 2002 and with the GPS in 2003.

### 3.1.2 IGISOL

Thick targets provide high yields of radioactive isotopes released from the target which are subsequently ionized with a separate ion source. However, this method depends

on the chemical properties of the elements of interest. This problem can be solved by using thin targets such that the produced isotopes have enough recoil energy to find their way out from the target. Outside the target these recoils must be stopped and moved to an experimental station. A method based on this principle is the He-jet technique, in which the recoiling reaction products are stopped in high-pressure helium and transported through a capillary system either to an ion source or directly to an experimental station [Äys76]. This technique has been used in various studies on nuclei close to the  $N = Z$  line, such as for  $^{31}\text{Cl}$  [Äys85, Ogn96]. However, a transport time of about 100 ms has made this method too slow for exotic nuclei.

The IGISOL (Ion Guide Isotope Separator On-Line) technique was developed in Jyväskylä over 20 years ago [Ärj81, Ärj86] and the results from the first on-line experiment were published in [Äys84]. In this method, the reaction products recoiling out of a thin target are thermalized in a helium gas cell just like in the He-jet method. The main difference is that in the ion guide a sufficient proportion of the recoils end up as  $1^+$  ions and there is no need for an external ion source, whereas in the He-jet method all recoils are neutralized. As the first ionization potential of helium is higher than the second ionization potential of most elements, slow highly charged ions produced in collisions related to nuclear reactions can only reach the  $2^+$  charge state in pure helium. Nevertheless, almost all recoil atoms leave the ion guide as  $1^+$  ions due to charge transfer reactions between the doubly-charged ions and impurity molecules of the helium gas ( $\text{H}_2$ ,  $\text{N}_2$ ,  $\text{O}_2$ ,  $\text{H}_2\text{O}$ ). The losses of produced atoms are mainly due to three-body recombination processes between electrons, ions and neutral gas atoms, diffusion to the walls of the target chamber and the formation of molecular ions with impurities in the gas [Äys01].

The ions formed in the ion guide are transported by a gas flow through a differential pumping system and by a weak electric field (skimmer) directly into the acceleration stage of a mass-separator (see fig. 3.3). After a typical acceleration to 40 keV, the ions are mass-separated by a  $55^\circ$  bending magnet and guided to an experimental station. The ion-guide method is fast (sub ms) and it does not depend on chemical properties of the elements. Therefore, this universal technique can be used even for refractory elements which are difficult for conventional ISOL-facilities.

During the years, the IGISOL facility has been improved several times [Den97, Pen97, Äys01, Hui04, Pen05]. A major upgrade of the IGISOL facility was done in 2003 [Pen05] in the middle of this thesis work. The  $^{31}\text{Cl}$  and  $^{58}\text{Zn}$  experiments were one of the first experiments done using the *light-ion ion guide* at the upgraded IGISOL. The light-ion ion guide designed for proton and He beams has a target inside a small stopping volume, which can be evacuated within one millisecond. Typical efficiencies of 1% to 10% have been obtained with this method for sub-ms activities. Due to impurities in the beam dump of the cyclotron beam, the high voltage of the IGISOL could not be held at 40 kV in these experiments and thus, IGISOL was run at 25 kV.

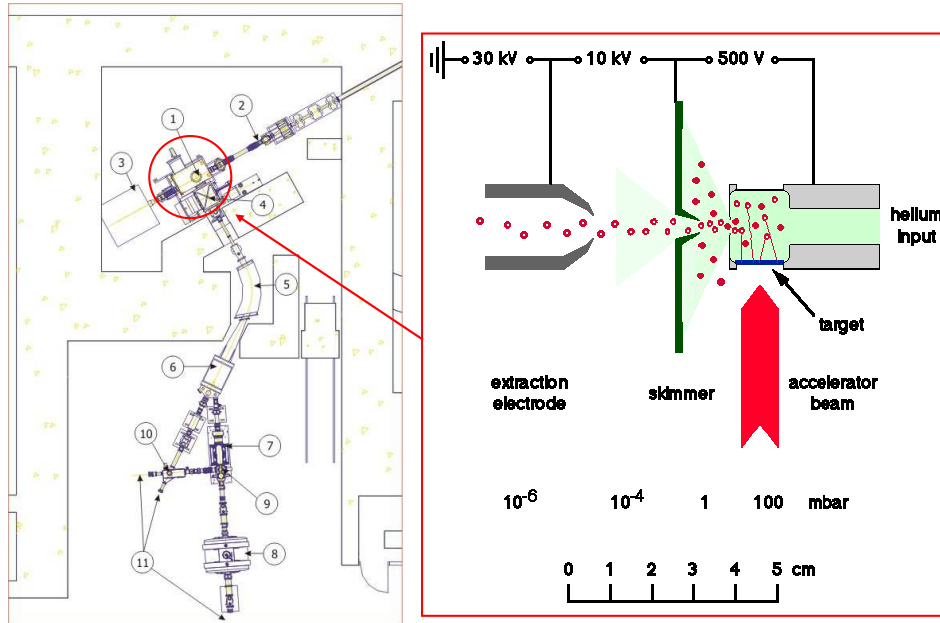


**Figure 3.3:** The IGISOL facility and the ion guide at IGISOL. The numbers refer to: 1. ion guide, 2. K-130 cyclotron beamline, 3. beam dump, 4. acceleration chamber, 5. dipole magnet, 6. switchyard, 7. RFQ cooler, 8. tandem Penning trap, 9. miniquadrupole deflector, 10. electrostatic deflector and the beamline upstairs and 11. experimental setups.

$^{31}\text{Cl}$  nuclei were produced via  $^{32}\text{S}(p,2n)$  fusion-evaporation reactions induced by a 40 MeV or 45 MeV proton beam on a ZnS target. The proton beam intensity was 10 – 20  $\mu\text{A}$  during the experiment. For calibration purposes,  $^{24}\text{Al}$  was produced with a 30 MeV proton beam and  $^{20}\text{Na}$  with a 45 MeV proton beam on a Mg target.

$^{58}\text{Zn}$  was produced via  $^{58}\text{Ni}(^3\text{He},3n)$  fusion-evaporation reactions by a 50 MeV  $^3\text{He}$  beam on a  $^{nat}\text{Ni}$  target. The beam current was about 1  $\mu\text{A}$ . A  $^3\text{He}$  beam on a Mg target was used to produce  $^{25}\text{Si}$  and a 45 MeV proton beam on a Mg target delivered  $^{20}\text{Na}$  for calibration purposes. The yields of nuclei produced via light-ion fusion-evaporation reactions in this work at IGISOL are summarized in table 3.1 which represents the average number of atoms per second at the experimental station.

In the heavy-ion induced fusion reactions, such as  $^{32}\text{S} + ^{54}\text{Fe}/^{nat}\text{Ni}$  used to produce nuclei in the  $A = 80$  region, the recoils are more energetic and thus, more difficult to stop in the helium gas than in the light-ion fusion evaporation reactions. In addition, plasma effect and ionization of the stopping gas by the primary beam lead to a much lower efficiency. The heavy-ion guide at IGISOL, also known as HIGISOL, has been described in refs. [Bér94], [Den98], [Oin98b] and [Hui04]. At HIGISOL, the targets are outside the stopping chamber. The so-called shadow method has been developed to minimize the effect of the primary beam. It is based on the difference between the angular distribution of the primary beam projectiles and reaction products after

**Table 3.1:** The yields of nuclei produced in the light-ion ion guide.

	$E_{beam}$ (MeV)	I ( $\mu$ A)	Yield (at/s)
$^{32}\text{S}(p,2n)^{31}\text{Cl}$	40	10–20	14
$^{32}\text{S}(p,2n)^{31}\text{Cl}$	45	10–20	12
$^{32}\text{S}(p,n)^{31}\text{S}$	40	10–20	$2.0 \times 10^4$
$^{32}\text{S}(p,n)^{31}\text{S}$	45	10–20	$1.5 \times 10^4$
$^{58}\text{Ni}(^3\text{He},3n)^{58}\text{Zn}$	50	2.5	0.6
$^{58}\text{Ni}(^3\text{He},3n)^{58}\text{Cu}$	50	2.5	500

**Table 3.2:** The yields of nuclei produced in the heavy-ion ion guide. A 150–170 MeV  $^{32}\text{S}^{7+}$  beam on an enriched  $^{54}\text{Fe}$  target (1.8 mg/cm<sup>2</sup>) was used for nuclei at mass  $A = 81$ . A  $^{nat}\text{Ni}$  target (2 mg/cm<sup>2</sup>) was used for nuclei at masses  $A = 85, 86$ . The beam intensity was around 500 nA. The fine tuning of the primary beam energy was done with degraders of Havar foil and/or  $^{nat}\text{Ni}$ .

Nuclide	$T_{1/2}$	Transitions used	Yield (at/s)
$^{81}\text{Zr}$	5.5 s	$\gamma$ 113 keV	< 0.2
$^{81}\text{Y}$	70.4 s	$\gamma$ 79 keV, $\gamma$ 124 keV	50
$^{81}\text{Sr}$	22.3 min	$\gamma$ 147.8 keV, $\gamma$ 186 keV	750
$^{81m}\text{Kr}$	13.1 s	$\gamma$ 190.5 keV	15
$^{85}\text{Nb}$	20.9 s	$\gamma+e$ 50 keV	2
$^{85m}\text{Nb}$	3.3 s	e 69 keV	1
$^{85}\text{Zr}$	7.86 min	$\gamma$ 416 keV, $\gamma$ 455 keV	200
$^{85m}\text{Zr}$	10.9 s	$\gamma$ 292.2 keV	5
$^{86}\text{Mo}$	19.6 s	$\gamma+e$ 47 keV, $\gamma+e$ 50 keV	15
$^{86}\text{Nb}$	88 s	$\gamma$ 752 keV, $\gamma$ 915 keV	25

scattering through a few mg/cm<sup>2</sup>-thick target [Bér94]. Whereas the angular spread of the primary beam is close to 0°, the reaction products are emitted as cone centered around 0° with an angle depending mainly on the target thickness. Hence, the primary beam entering a stopping chamber can be eliminated with a beam stopper. The position of the target with respect to the entrance window can be adjusted so that opening angle of the recoils varies from 7° to 63° [Hui04]. The fine tuning of the primary beam energy can be done with four degrader foils before the target.

The spectroscopic experiment on nuclei close to  $A = 80$  was done before the upgrade and the experiment on the masses in this region was performed after the upgrade. However, the production method was quite similar. In the first experiment, the isotopes of interest were produced by a 150–170 MeV  $^{32}\text{S}^{7+}$  beam with an intensity of about 500 enA on  $^{nat}\text{Ni}$  (2 mg/cm<sup>2</sup>) and  $^{54}\text{Fe}$  (1.8 mg/cm<sup>2</sup>) targets. The  $^{nat}\text{Ni}$  target was used to produce nuclides with mass numbers  $A = 85$  and 86, whereas enriched target material of  $^{54}\text{Fe}$  was optimal for the synthesis of  $A = 81$  isotopes. The fine tuning of the primary beam energy was performed with degraders of Havar foil and/or

$^{nat}\text{Ni}$ . The reaction products passing through a  $2.1 \text{ mg/cm}^2$ -thick Havar window were stopped in the gas cell. After extraction from the gas cell, the ions were accelerated to 40 keV, mass-separated and implanted into a collector tape. Experimental details after HIGISOL for the experiment on the masses in the  $A = 80$  region are given in detail in sec. 3.2.6. The yields of nuclei produced via heavy-ion induced fusion-evaporation reactions in this work are summarized in table 3.2. They represent the average number of atoms per second at the experimental station.

## 3.2 Experimental setups

This thesis work consists of a series of measurements performed at ISOLDE and at IGISOL. The beta decay of  $^{31}\text{Cl}$  was studied at IGISOL with double-sided silicon strip detectors and with the ISOLDE Silicon Ball. Measurements on the beta-delayed particles of  $^{58}\text{Zn}$  were performed with the ISOLDE Silicon Ball setup at ISOLDE and at IGISOL and beta-delayed  $\gamma$ -rays from  $^{58}\text{Zn}$  were detected with two MINIBALL Ge detectors at ISOLDE. In order to describe the ISOLDE Silicon Ball before the double-sided silicon strip detectors, the setups related to  $^{58}\text{Zn}$  are reviewed first. Studies on the beta-delayed particles of  $^{69,71,73}\text{Kr}$  were done with a  $\Delta E$ -E detector setup at ISOLDE. Neutron-deficient isomers of astrophysical interest close to  $A = 80$  were studied with an ELLI detector setup at IGISOL. The masses in the  $A = 80$  region were measured by using the JYFLTRAP setup. These setups are described carefully in the following subsections.

### 3.2.1 MINIBALL detectors for beta-delayed $\gamma$ -rays of $^{58}\text{Zn}$

Two MINIBALL Ge detectors [Ebe01] and a  $4\pi\beta$ -detector, which acted as a trigger, were used to detect beta-delayed  $\gamma$ -rays of  $^{58}\text{Zn}$  at ISOLDE. The two MINIBALL detectors were separated by 70 mm and the  $4\pi\beta$ -detector was positioned in the middle of the MINIBALL detectors (see fig. 3.4). MINIBALL detectors consist of three clusters which are further divided into six segments. The segmentation offers a good angular resolution which is crucial for the Doppler correction of the  $\gamma$ -rays from fast recoiling nuclei. There was no need for segmentation in this experiment and thus, altogether six Ge detectors (called as 12A, 12B, 12C, 13A, 13B and 13C, see fig. 3.4) were used. Unfortunately, the cluster 13C did not work very well and its energy resolution was poor. It was therefore rejected from the data analysis.

The beam from ISOLDE entered a  $4\pi\beta$ -detector through a small aperture and it was implanted into a tape. The beamgate from the target to ISOLDE was open for 300 ms after 5 ms from the proton pulse. The data were collected for about 800 ms and

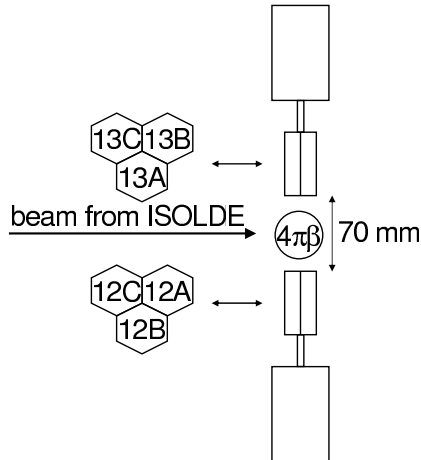


**Figure 3.4:** A schematic picture of the  $\beta - \gamma$  setup for the detection of beta-delayed  $\gamma$ -rays from  $^{58}\text{Zn}$  at ISOLDE. The view is from the top of the setup. The position of the clusters with respect to the beam and the  $4\pi\beta$ -detector is shown.

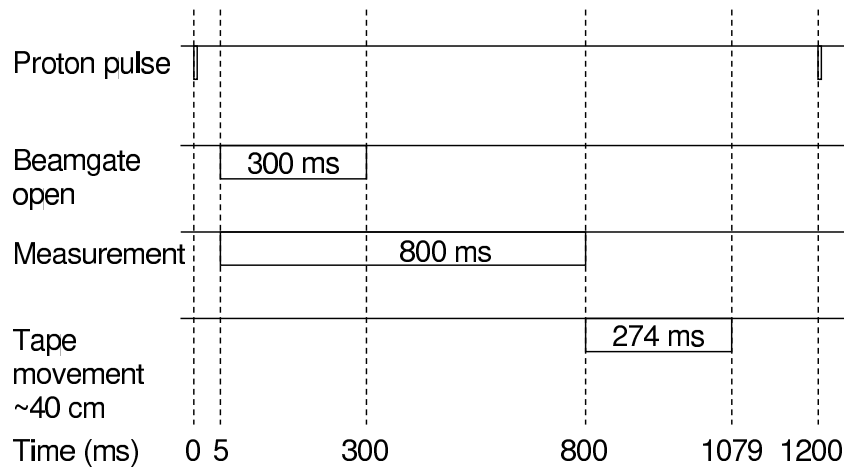


**Figure 3.5:** Time structure of the data collection with the MINIBALL detectors.

the tape was moved after the collection. The whole cycle was about 1079 ms which allowed data taking between the proton pulses (see fig. 3.5).

The time signals from the Ge detectors went through timing filter amplifiers, constant fraction discriminators and dual gate generators. The main trigger came from the time signal of the  $4\pi\beta$ -detector. The trigger condition was vetoed by the signal from the lasers in order to avoid noise from the 11 kHz lasers. The detectors were calibrated with  $^{152}\text{Eu}$  and  $^{228}\text{Th}$  sources.

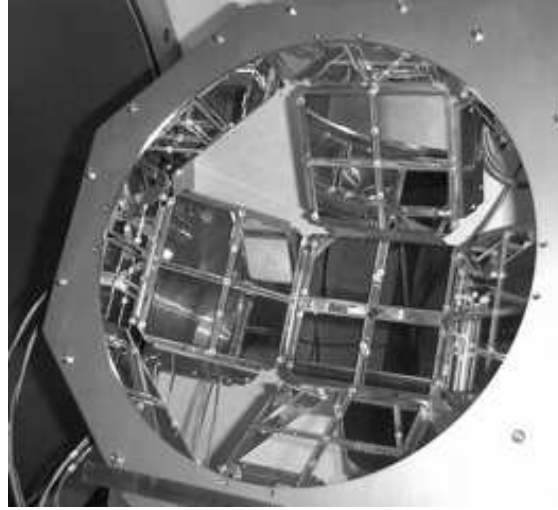
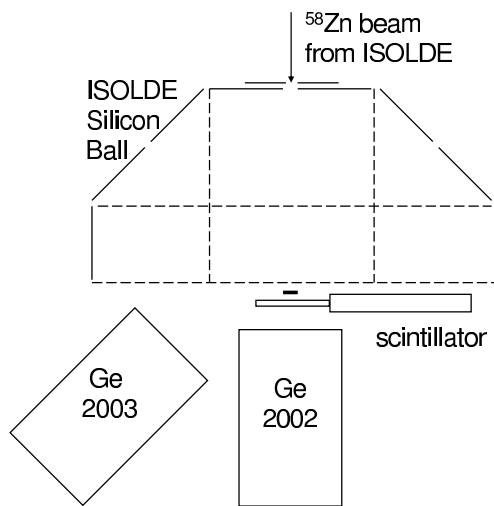


Figure 3.6: The ISOLDE Silicon Ball.

### 3.2.2 ISOLDE Silicon Ball for beta-delayed protons of $^{58}\text{Zn}$

The ISOLDE Silicon Ball [Fra03] is a novel charged-particle spectroscopy device which has a high efficiency and granularity. Presently, the Silicon Ball is a hemisphere consisting of 5 square faces with an inner area of  $119 \times 119 \text{ mm}^2$  and eight faces with an area of  $51 \times 119 \text{ mm}^2$  (see fig. 3.6). Each square is divided into four standard  $51 \times 51 \text{ mm}^2$  silicon detectors which are further segmented into four quadrants. The smaller rectangles are divided into two segmented  $51 \times 51 \text{ mm}^2$  detectors. Thus, the Silicon Ball has now  $5 \times 16 + 8 \times 8 = 144$  detectors with a size of  $25.5 \times 25.5 \text{ cm}^2$ . All standard detectors are provided by Micron Semiconductor Ltd. The radius of the ball is about 15 cm and the solid angle of one segmented detector is about 0.21 % if the implantation point is at the origin of the ball. Therefore, the total efficiency of the detector can be, presently, about  $144 \times 0.21\% \approx 30\%$ . In the future, the Silicon Ball will be a  $4\pi$  detector with a shape of a rhombicuboctahedron. It will consist of 18 square faces of  $119 \times 119 \text{ mm}^2$  and eight equilateral triangles with 119 mm sides.

The average active thickness of a Silicon Ball detector is  $988 \pm 6 \mu\text{m}$ , fully depleted at around 200 V. Protons with energies from 100 keV to 12 MeV are stopped in the detectors. Particle identification should be possible via measuring a time of flight (TOF) between a plastic scintillator at the implantation point and a Silicon Ball detector. Another option is to use the Pulse Shape Discrimination (PSD) technique which takes advantage of the sensitivity of the pulse shape to the density and length of the ionization track of the particles. The main difference comes from the finite drift time of the electrons and holes produced in the ionization track and the plasma effect. However, either of these techniques could be used in these experiments, and therefore, the particle identification was not possible.



**Figure 3.7:** The ISOLDE Silicon Ball setup used to detect beta-delayed protons from  $^{58}\text{Zn}$  at ISOLDE.

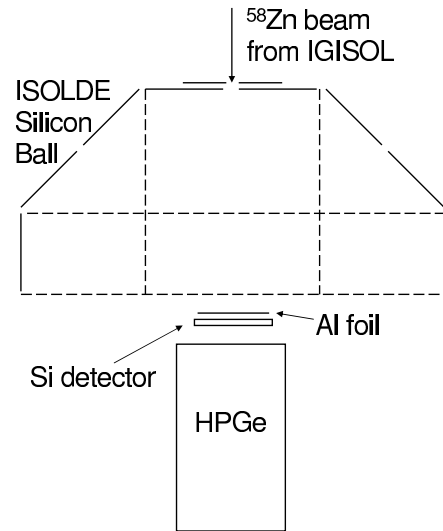


**Figure 3.8:** The ISOLDE Silicon Ball setup used to detect beta-delayed protons from  $^{58}\text{Zn}$  at IGISOL.

The signals from the Silicon Ball detectors went through Mesytec MSI-8 preamplifiers and Mesytec STM-16 shaping/timing filter amplifiers with discriminator and multiplicity triggers. CAEN V785 32 channel ADCs and V775 32 channel TDCs were used to convert analog signals into digital form.

The Silicon Ball was mainly used for the detection of the beta-delayed protons from  $^{58}\text{Zn}$ . Beta-delayed protons of  $^{58}\text{Zn}$  were studied twice at ISOLDE and once at IGISOL. The reason for so many experiments is that in the first experiment at ISOLDE the Silicon Ball had just been constructed and the setup was not totally ready for the experiment. For example, no time signals for the detectors were available. In addition, the target was already used for the  $\gamma$ -ray detection for a couple of days and its performance was not optimal. The second experiment at ISOLDE failed due to a wrong temperature calibration of the target line and due to a too focused proton beam. The yields were lower than in the first experiment. After two experiments at ISOLDE,  $^{58}\text{Zn}$  was produced at IGISOL in order to check whether the production via  $^{58}\text{Ni}(^3\text{He},3n)^{58}\text{Zn}$  with a  $^3\text{He}$  beam current around  $1\ \mu\text{A}$  is reasonable.

The time structure of the ISOLDE beam was similar to the MINIBALL setup. The delay after the proton pulse was 5 ms and the beamgate was open for 300 ms. The beam from ISOLDE came through an aperture into the Silicon Ball and it was implanted into a tape. The tape was moved only once in every PS supercycle (about 14.4 s) in 2002. In 2003, the tape was moved after each proton pulse. Right behind the tape there was a plastic scintillator with a photomultiplier tube for detecting beta particles. In order to relate proton intensities to  $\gamma$ -ray intensities, a Ge detector was used to detect beta-delayed  $\gamma$ -rays. In 2002 a coaxial Ge detector was used, while in

2003 a semiplanar Ge detector was employed. The Ge detector was placed behind the plastic scintillator in 2002 (see fig. 3.7), which had a disadvantage that beta-particles going through the scintillator triggered the data acquisition. A contribution of these beta particles is seen in the gamma spectrum. The trigger used was a hit in the scintillator or any pair of detectors in the Silicon Ball or three hits in the Silicon Ball. The data acquisition was vetoed by the laser signals in the same way as in the MINIBALL setup. To avoid the beta particle contribution in the gamma spectrum, the Ge detector was put in a different position in 2003 (see fig. 3.7). This reduced the efficiency as the detector was further away from the implantation point.

At IGISOL, the beam was implanted into an Al foil (thickness  $\approx 0.22 \text{ mg/cm}^2$ , diameter  $\approx 32 \text{ mm}$ ) which was in front of a beta detector. Thus, the activity was not removed from the implantation point and no timing data were available for the off-line analysis. The beta detector was a silicon detector with an area of  $600 \text{ mm}^2$  and a thickness of  $500 \text{ }\mu\text{m}$  (see fig. 3.8). The trigger was a hit in the Silicon Ball or a hit in the beta detector. A HPGe detector (Nordball) was again situated behind the beta detector.

### 3.2.3 Double-Sided Silicon Strip Detectors for the beta decay of $^{31}\text{Cl}$

Double-sided silicon strip detectors were used at IGISOL in an experiment on the beta decay of  $^{31}\text{Cl}$ . The beam from IGISOL was implanted into a  $30 \text{ }\mu\text{g/cm}^2$ -thick carbon foil placed at a  $45^\circ$  angle to the beam (see figs. 3.9 and 3.10). The beam entered the detector chamber through an aperture of the ISOLDE Silicon Ball. A collimator plate was put in front of the aperture as in the case of  $^{58}\text{Zn}$  at IGISOL. A 70 % HPGe detector measured gamma rays. Its nose was put into a tube going inside the detector chamber as close as possible to the implantation point. The HPGe detector was calibrated with  $^{60}\text{Co}$ ,  $^{134}\text{Cs}$  and  $^{228}\text{Th}$  sources and on-line with  $^{24}\text{Al}$ .

The carbon foil was also surrounded by three double-sided silicon strip detectors (DSSSDs), which were backed with three thick silicon detectors. Two DSSSDs were at a  $45^\circ$  angle with respect to the third one in order to maximize the solid angle covered by the detectors. The front side of a DSSSD consists of 16 strips (*front strips*) which are 50 mm long and 3 mm wide and separated by 0.1 mm and the back face has 16 similar but orthogonal strips (*back strips*) [Ber03, Ten04]. One of the DSSSDs was a MICRON design W detector with a dead layer of 600 nm [Ber03]. The rest were MICRON's new thin-window designed detectors with ultra-thin dead layers of 100 nm [Ten04]. As the DSSSDs were only about  $60 \text{ }\mu\text{m}$  thick, beta particles left very little energy in them. Therefore, the DSSSDs were ideal for detecting protons and alpha particles.

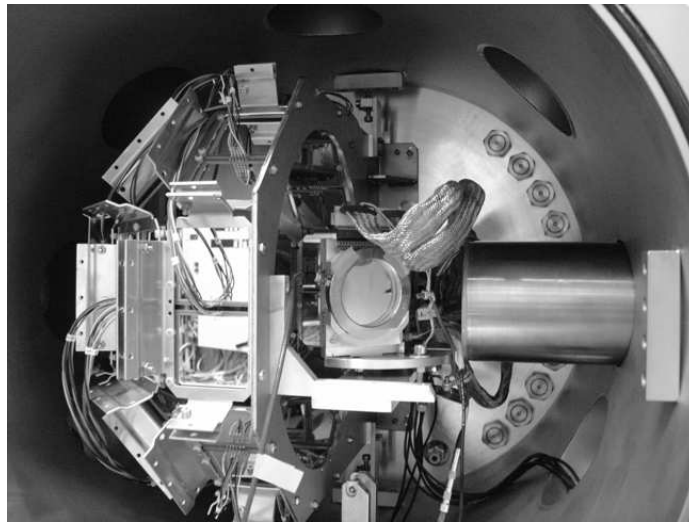


**Figure 3.9:** A photo of the experimental setup for the beta decay of  $^{31}\text{Cl}$  at IGISOL. The ISOLDE Silicon Ball, a thick silicon detector (E3) behind the detector DSSSD3 (see fig. 3.10) and the cap for the HPGe are shown in this figure. The beam from IGISOL enters the detector chamber from the left.

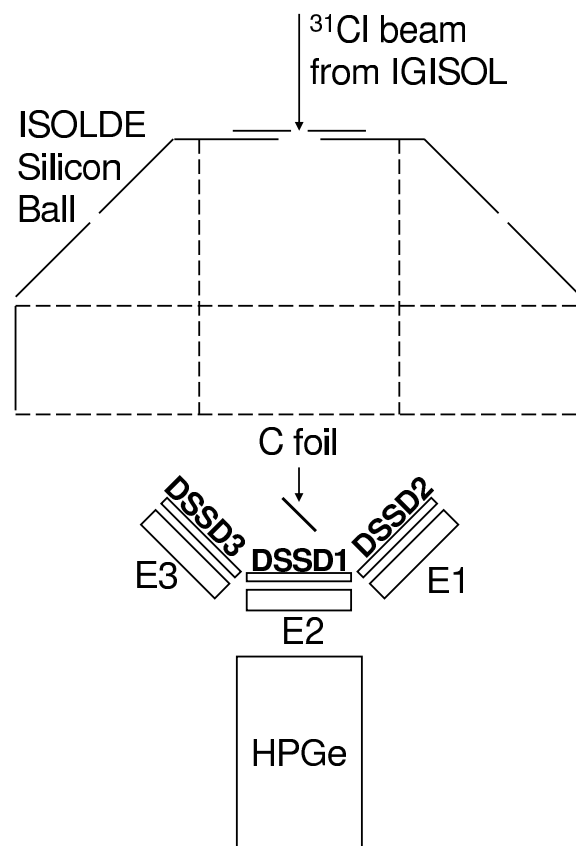


**Figure 3.10:** The experimental setup for the beta decay of  $^{31}\text{Cl}$  at IGISOL.

The data acquisition was triggered by beta particles which meant a hit in any of the three thick silicon detectors behind the DSSSDs or a hit in any of the detectors in the Silicon Ball. The measured total beta efficiency was 24.9(19) % based on the intensity ratio of the 1266 keV  $\gamma$ -peak from the beta decay of  $^{31}\text{S}$  in a beta-triggered spectrum and in a singles spectrum. The geometrical beta efficiency was little higher, about 37.5(10) %. The data acquisition suffered from noise, which was one reason for the rejection of the silicon detectors in the outer ring of the Silicon Ball frame. As a result, 80 Silicon Ball detectors were appropriate for detecting beta particles whereas the DSSSDs served as proton detectors. Artificial hits induced by sparks that dropped the accelerating high voltage at IGISOL were also problematic. Fortunately, most of the unwanted events in the DSSSDs could be rejected in the data analysis by requiring that for each event in a front strip there must be an event with a corresponding energy in one of the back strips. However, protons below 700 keV could not be observed with the DSSSDs due to noise.

The DSSSDs were calibrated in a similar manner as explained in ref. [Ber03]. At first, the position of the source with respect to the detectors was determined and the strips were calibrated with  $^{20}\text{Na}$  and  $^{148}\text{Gd}$ . In order to observe low-energy protons ( $E_p \approx 130$  keV) from the IAS of  $^{31}\text{S}$  with a good energy resolution, the amplification was set to about 1 keV/channel. Unfortunately, with this amplification only 2150 keV  $\alpha$  particles from  $^{20}\text{Na}$  and 3183 keV  $\alpha$  particles from the  $^{148}\text{Gd}$  source could be used for the calibration. Beta-delayed alphas from  $^{24}\text{Al}$  were not intense enough to calibrate each strip individually. The energy left in the dead layer and that deposited into the detector were calculated using the stopping power and range tables from SRIM2003 [SRIM03]. For each front (back) strip a coincidence with one central back (front) strip 8 or 9 was required. There were not enough data in one pixel for energy calibration with  $^{20}\text{Na}$  and therefore, the foil and dead energy effect were calculated as a solid-angle weighted average for each strip.

The original energy calibration gave too low energies for protons. This was expected from the lack of calibration points, which made the errors in the peak fits and deposited energies (caused by the uncertainties in dead layers, foil thicknesses and positions of the detectors) essential. The calibration was corrected with the most intense proton peak of  $^{31}\text{Cl}$  ( $E_p=986(10)$  keV [Äys85]). As this peak was not intense enough in individual strips, this was done by adding together all front strips for each DSSSD and all back strips for each DSSSD. The solid-angle weighted average energies deposited into the detectors from the 986 keV group were calculated and the energy calibration was corrected by adding the difference between the calculated values and the energies from the first calibration. The new calibration agreed with the earlier results for the known peaks.

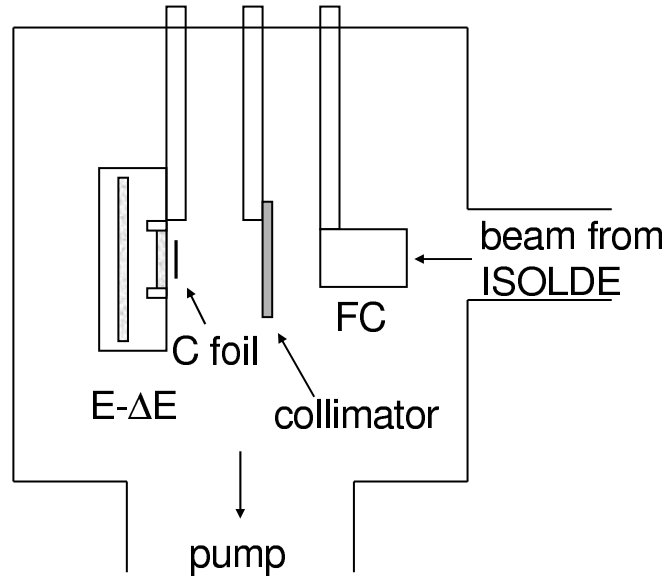


**Figure 3.11:** The experimental setup for beta-delayed protons of Kr isotopes.

### 3.2.4 $\Delta E$ -E detector setup for beta-delayed protons of Kr isotopes

Beta-delayed protons from  $^{69}\text{Kr}$ ,  $^{71}\text{Kr}$  and  $^{73}\text{Kr}$  were detected with a  $\Delta E$ -E telescope which consisted of two silicon detectors. The  $\Delta E$  silicon detector from Ortec had an area of  $300\text{ mm}^2$  and a thickness of  $24\text{ }\mu\text{m}$ . It was in front of the E detector which was a  $50 \times 50\text{ mm}^2$ ,  $992\text{ }\mu\text{m}$ -thick silicon detector from Micron. The beam from ISOLDE was implanted in a  $100\text{ }\mu\text{g}/\text{cm}^2$  thick carbon foil which was placed about 4 mm before the surface of the  $\Delta E$  detector (see fig. 3.11). The carbon foil had to be changed twice during the run. New foils were about  $75\text{ }\mu\text{g}/\text{cm}^2$  thick. The solid angle of the detector was determined as  $19.2(10)\%$ .

### 3.2.5 ELLI setup for the studies of isomers around $A \approx 80$

ELLI is a magnetic conversion-electron transporter spectrometer consisting of two coils [Par91]. It was used to detect conversion electrons from nuclei close to  $A = 80$  at IGISOL. The beam from IGISOL was implanted into a tape at the first detector station (see fig. 3.12). It consisted of two HPGe detectors situated face-to-face and a plastic scintillator which gated  $\gamma$ -radiation by  $\beta$ -particles. After some time of accumulation at the first station, the tape was moved and the source was delivered to the second detector station where an electromagnetic electron transporter and a low energy Ge detector (LeGe) were installed. The next source was prepared at the first station until the measurements were completed at the second station.

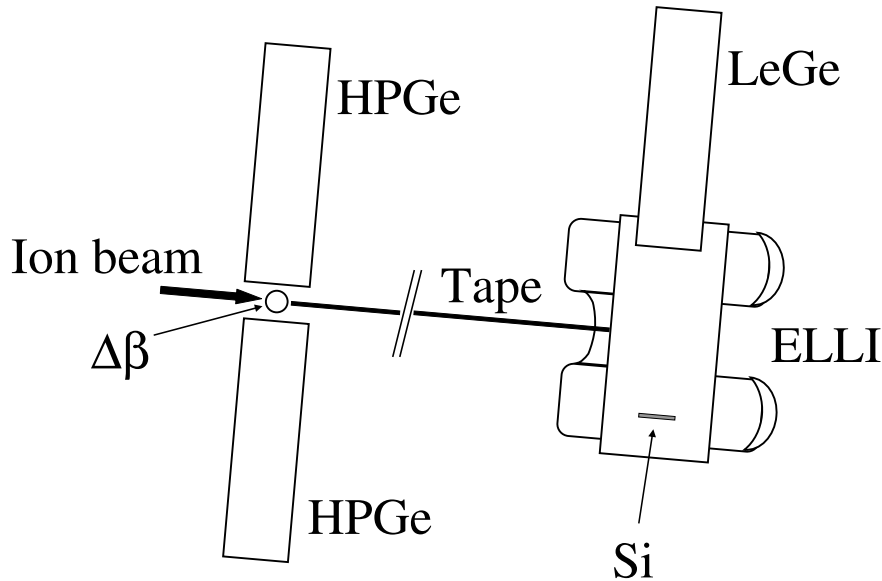


**Figure 3.12:** A schematic view of the experimental setup for the detection of isomers close to  $A = 80$ .

Conversion electron decays and low energy gamma radiation were studied at the second detector station. Electron spectra were measured by ELLI which transported electrons from the implantation point to a cooled Si(Au) surface barrier detector in a remote detection area. This helped to reduce the background considerably. A low energy Ge detector with a very thin entrance window (0.5 mm Be) was placed on the opposite side of the Si detector in close geometry with respect to the implantation point (see fig. 3.12). ELLI had a typical efficiency of about 5 % at electron energies less than 100 keV in this experiment. With this kind of setup one could measure both the absolute value for  $\alpha_K$  and the ratio  $\alpha_K/\alpha_{L+M}$ .

### 3.2.6 JYFLTRAP for high-precision mass measurements

JYFLTRAP is a Penning trap system for high-precision mass measurements at IGISOL. In this thesis, it was used to measure masses of neutron-deficient nuclides close to  $A \approx 80$  produced by a  $^{32}\text{S}$  beam on an enriched  $^{54}\text{Fe}$  or  $^{nat}\text{Ni}$  target. After extraction from the IGISOL gas cell and acceleration to 30 keV, the ions were mass-separated and injected into a radio frequency quadrupole (RFQ) ion beam cooler and buncher [Nie01]. The RFQ consists of four cylindrical rods and provides a transverse confinement of ions. Inside the RFQ, the ions lose their kinetic energy in collisions with the He buffer gas at a pressure of about  $10^{-2}$  mbar, and thus, the ions are cooled. The cooled ions accumulate to the trap axis and drift towards the exit hole. The ions can be released as short bunches by switching the last electrodes of the RFQ cooler.

After the RFQ cooler, the short bunches of ions are injected into the JYFLTRAP.

JYFLTRAP consists of two cylindrical Penning traps in a superconducting magnet ( $B=7$  T) [Kol04]. The two Penning traps are symmetrically located in two homogeneous  $1\text{ cm}^3$  regions about 10 cm from the center of the magnet. The first trap, a *purification trap*, is filled with helium buffer gas at a pressure of about  $10^{-4}$  mbar. It is used for isobaric purification by employing mass selective buffer gas cooling. Firstly, the possible contaminant ions are removed by applying an RF dipole excitation to the trap. After that, an RF quadrupole excitation at a mass dependent cyclotron frequency  $\nu_c$  is applied. This quadrupole excitation with buffer gas cooling centers the ions of interest and a mass resolving power of about  $10^5$  can be achieved with a total cycle time of 400 ms used in this experiment.

The isobarically purified and cooled ions were delivered to the second Penning trap, the *precision trap*, which operates in vacuum and is used for high precision mass measurements employing the time-of-flight ion cyclotron resonance technique [Kön95]. In this trap, an RF dipole excitation was applied to increase the magnetron radius of all ions. After that, an RF quadrupole excitation was applied to convert the slow magnetron motion to a fast reduced cyclotron motion. In this experiment, a full conversion from magnetron to the reduced cyclotron motion with a higher radial energy was achieved at a resonance frequency by using an excitation time of 900 ms with a corresponding excitation amplitude. Finally, ions were extracted from the trap to a set of drift tubes in a strong magnetic field gradient. The magnetic moments of ions interact with the magnetic field gradient and the ions experience an axial force converting radial kinetic energy to axial energy. The ions in resonance with the applied quadrupole field have a higher kinetic energy and therefore they gain more axial energy which reduces the time-of-flight to the micro channel plate (MCP) detector at the end of the trap line. By measuring the time-of-flight (TOF) as a function of excitation frequency, the cyclotron frequency ( $\nu_c$ ) of the ions of interest can be determined. The mass of the ions can then be calculated using eq. 3.3:

$$\nu_c = \frac{q}{2\pi m} B \quad (3.3)$$

where the magnetic field  $B$  is calibrated with a well-known reference mass,  $\nu_c$  is the cyclotron frequency of the ion,  $m$  is the mass of the ion and  $q$  is the charge state of the ion.

The atomic mass of the unknown ion can then be determined using equation 3.4:

$$m = \frac{\nu_c^{ref}}{\nu_c} (m_{ref} - m_e) + m_e \quad (3.4)$$

where  $\nu_c^{ref}$  is the cyclotron frequency of the reference ion,  $m_{ref}$  is the mass of the reference atom and  $m_e$  is the electron mass.



# 4 Results and discussion

## 4.1 Excited states of $^{31}\text{S}$ studied via beta decay of $^{31}\text{Cl}$

A relatively large  $Q_{EC}$  value of 11980(50) keV [Aud03b], measured in  $^{36}\text{Ar}(^3\text{He},^8\text{Li})^{31}\text{Cl}$  reactions [Ben77], provides an opportunity to study beta-decay strength of  $^{31}\text{Cl}$  over a broad energy range. However, beta decay of  $^{31}\text{Cl}$  is not very well known due to its weak proton decay branch. The heavily populated IAS in the daughter nucleus  $^{31}\text{S}$  lies at 6268(10) keV [End90], just above the proton separation energy  $S_p = 6133.0(15)$  keV [Aud03b]. Therefore, the IAS most likely decays by emitting high-energy gamma rays or low-energy protons which are hard to detect.

The beta decay of  $^{31}\text{Cl}$  leads to states in  $^{31}\text{S}$  whose energies and decay properties are intrinsically interesting in respect of the opportunity to study the mirror energy differences between these states and those in the mirror nucleus,  $^{31}\text{P}$ . A recent experiment studied the excited states of  $^{31}\text{S}$  and  $^{31}\text{P}$  populated via  $^{12}\text{C}(^{20}\text{Ne},n)$  and  $^{12}\text{C}(^{20}\text{Ne},p)$  reactions with the Gammasphere detector setup at the ATLAS accelerator at Argonne National Laboratory [Jen05]. The mirror energy differences have also been studied via one-neutron pickup reactions on  $^{32}\text{S}$  [Ver99] and via one or two nucleon transfer reactions, such as  $^{29}\text{Si}(^3\text{He},n(\gamma\gamma))^{31}\text{S}$  [Dav75]. Decay properties of the excited states in  $^{31}\text{S}$  are also important for the studies of the nucleosynthesis in ONe novae as discussed in sec. 2.3.2.

The beta decay of  $^{31}\text{Cl}$  has been studied previously by a He-jet method [Äys82, Äys83, Äys85, Ogn96]. A half-life of 150(25) ms has been determined from the most intense proton peak at 989 keV in [Äys82]. Proton groups at 989(15) keV and 1528(20) keV have been reported in [Äys83] and six additional proton peaks have been observed in the energy range of 845 keV – 2204 keV in [Äys85]. The beta-decay branching of the 986 keV protons has been estimated to be 0.44 % and the total branching of proton-emitting states to be 0.7 % in [Äys85]. Although several proton peaks have been carefully measured, the experiments have suffered from the lack of mass separation. For example, all peaks except those of 986 keV and 1520 keV observed in [Äys85] have later been claimed to arise from the beta decay of  $^{25}\text{Si}$  [Ogn96]. In addition, beta-delayed protons from  $^{32}\text{Cl}$  have dominated the spectra which has made it difficult to distinguish possible weak proton peaks of  $^{31}\text{Cl}$ . No beta-delayed  $\gamma$ -rays have been

observed in these experiments. Nevertheless, one  $\gamma$ -ray has been associated with the beta decay of  $^{31}\text{Cl}$  in an experiment on the beta decay of  $^{31}\text{Ar}$  [Axe98]. This 2235.5(5) keV gamma ray corresponds to the decay of the second excited state ( $5/2^+$ ) to the ground state of  $^{31}\text{S}$  ( $1/2^+$ ).

#### 4.1.1 Beta-delayed $\gamma$ -rays

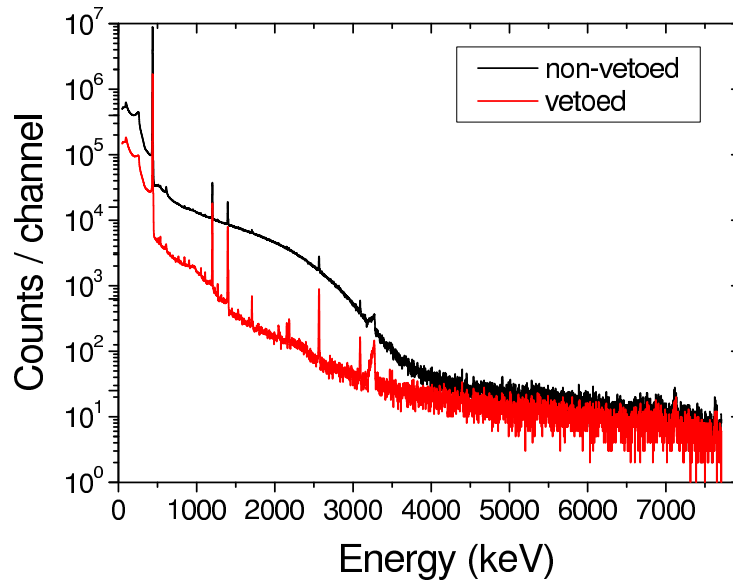
The isolation of beta-delayed  $\gamma$ -rays with the HPGe detector was experimentally challenging. Firstly, gamma spectra were dominated by the beta decay of  $^{31}\text{S}$  which is much longer-lived ( $T_{1/2} = 2.572$  s) and produced more abundantly (see table 3.1) than  $^{31}\text{Cl}$ . Secondly, the activity could not be removed from the setup as the beam was continuously implanted into the carbon foil. To get an idea of the  $^{31}\text{S}$  contribution, the beam was pulsed at the switchyard of the IGISOL facility for one day. The beam was on for the first 5 s and off for the last 5 s in the total cycle of 10 seconds. The data acquisition was on from 5.5 s to 10 s which guaranteed that there was no short-lived  $^{31}\text{Cl}$  left. The pulsed  $^{31}\text{S}$  spectrum was scaled based on the intensities of the 511 keV annihilation peaks in the  $^{31}\text{S}$  (pulsed) and  $^{31}\text{Cl}$  (not pulsed) spectra and subtracted from the  $^{31}\text{Cl}$  spectrum in order to check the peaks belonging to the beta decay of  $^{31}\text{Cl}$ . Thirdly, beta particles detected in the silicon detector (called as E2 in fig. 3.10) in front of the HPGe detector triggered the data acquisition and a contribution of these beta particles is seen in the  $\gamma$ -spectrum (see fig. 4.1). This could be overcome by requiring that every time a  $\gamma$ -ray is detected, there is no event in the E2 silicon detector. The veto requirement revealed most of the interesting gamma peaks.

A  $\gamma$ -peak at an energy of 2234.5(8) keV (see fig. 4.2) was observed both in the spectrum where the  $^{31}\text{S}$  contribution had been subtracted and in the spectrum vetoed by the E2 silicon detector. This peak at 2235.5(5) keV is the only  $\gamma$ -peak previously observed in the beta decay of  $^{31}\text{Cl}$  [Axe98]. As the energy gain was about 1.9 keV/channel, one could not distinguish between the 2235.5(5) keV peak of  $^{31}\text{Cl}$  and 2239.5(6) keV peak of  $^{31}\text{S}$ . Thus, the area of the 2239.5 keV peak was estimated based on the known  $\gamma$ -ray intensities and the area of the 1266.12 keV  $\gamma$ -peak from the beta decay of  $^{31}\text{S}$ . Other candidates for  $\gamma$ -rays from the beta decay of  $^{31}\text{Cl}$  were detected at energies of 1249.1(14) keV, 3536(2) keV and 4045(2) keV (see figs. 4.3, 4.4 and 4.5). These weak peaks could not be observed in the spectrum where the  $^{31}\text{S}$  contribution had been subtracted mainly due to too low statistics in the pulsed  $^{31}\text{S}$  spectrum.

The observed gamma rays can be expected from the known levels of  $^{31}\text{S}$  (see ref. [End90] and table 4.1). Assuming that the  $\gamma$ -transition with an energy of 3536(2) keV goes to the state at 2235.6 keV, an excitation energy of 5772(2) keV is obtained for the initial state. It agrees well with a  $5/2^+$  state at 5777(5) keV [Ver99]. If the 4045(2) keV  $\gamma$ -transition feeds the state at 2235.6 keV, it yields an energy of 6280(2) keV in agreement with the suggested energy of 6268(10) keV [End90] for the IAS in  $^{31}\text{S}$ .

**Table 4.1:** Observed gamma rays and corresponding literature values (from [Ver99] for the 5777 keV state, other values from [End98]).

$E_\gamma$ (keV) this work	$E_\gamma$ (keV) literature	Transition
1249.1(14)	1248.8(3)	1248.9(2) keV ( $3/2^+$ ) $\rightarrow$ 0 keV ( $1/2^+$ )
2234.5(8)	2235.5(5)	2235.6(4) keV ( $5/2^+$ ) $\rightarrow$ 0 keV ( $1/2^+$ )
3536(2)	3541(5)	5777(5) keV ( $5/2^+$ ) $\rightarrow$ 2235.6(4) keV ( $5/2^+$ )
4045(2)	4032(10)	6268(10) keV ( $3/2^+$ , IAS) $\rightarrow$ 2235.6(4) keV ( $5/2^+$ )

**Figure 4.1:** A beta-triggered gamma spectrum together with a spectrum vetoed by the E2 silicon detector in front of the HPGe detector.

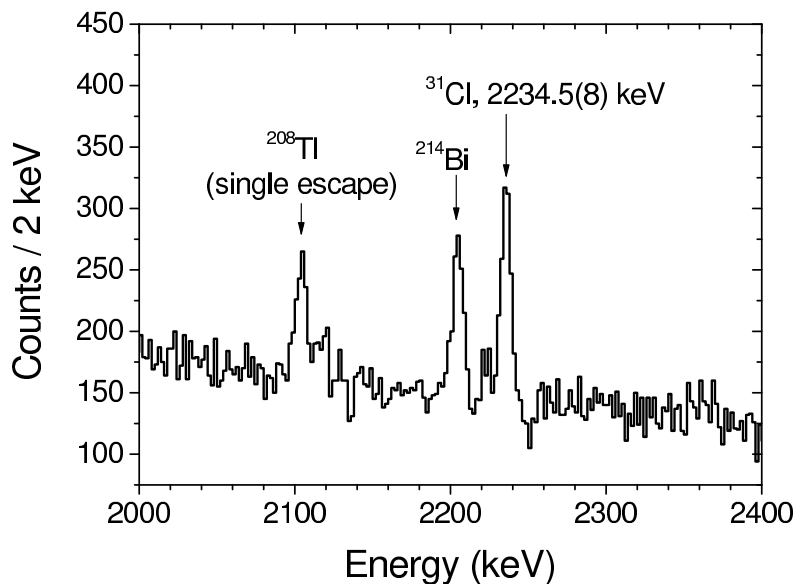


Figure 4.2: The 2234.5(8) keV  $\gamma$ -peak in the spectrum of  $^{31}\text{Cl}$  vetoed by the E2 silicon detector.

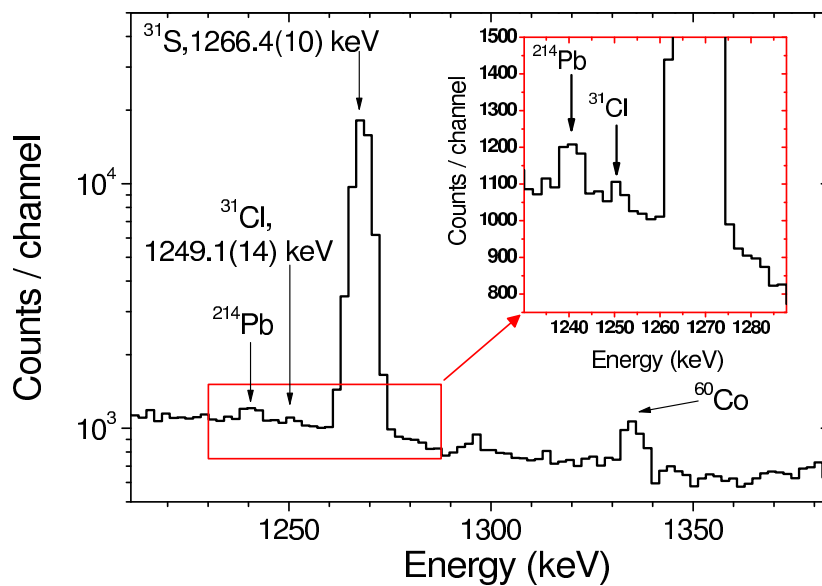
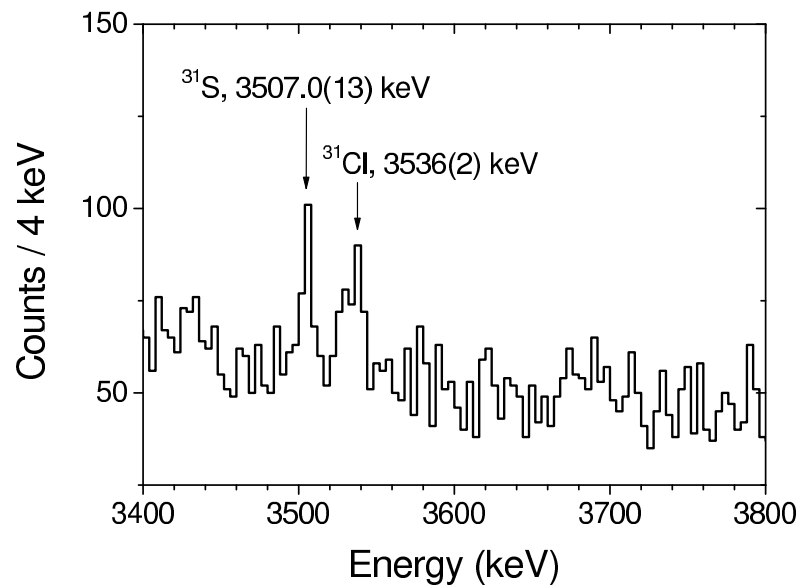
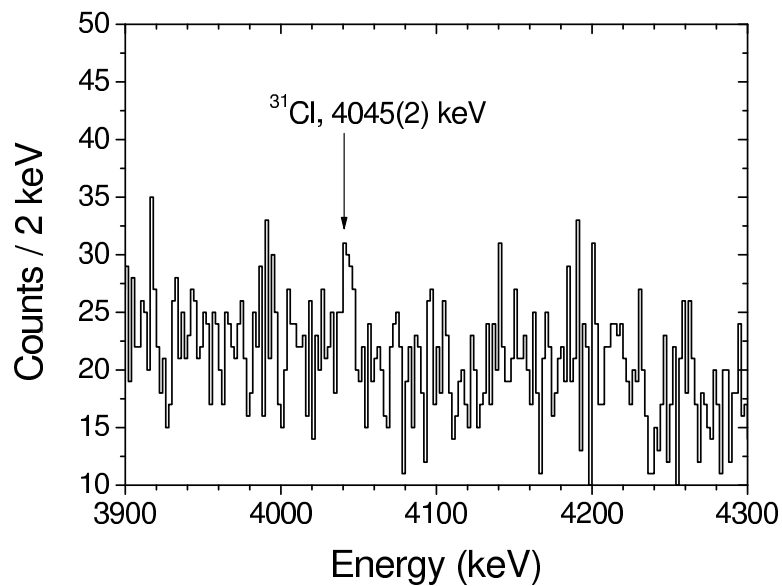


Figure 4.3: The 1249.1(14) keV  $\gamma$ -peak in the spectrum of  $^{31}\text{Cl}$  vetoed by the E2 silicon detector.



**Figure 4.4:** The 3536(2) keV  $\gamma$ -peak in the spectrum of  $^{31}\text{Cl}$  vetoed by the E2 silicon detector.



**Figure 4.5:** The 4045(2) keV  $\gamma$ -peak in the spectrum of  $^{31}\text{Cl}$  vetoed by the E2 silicon detector.

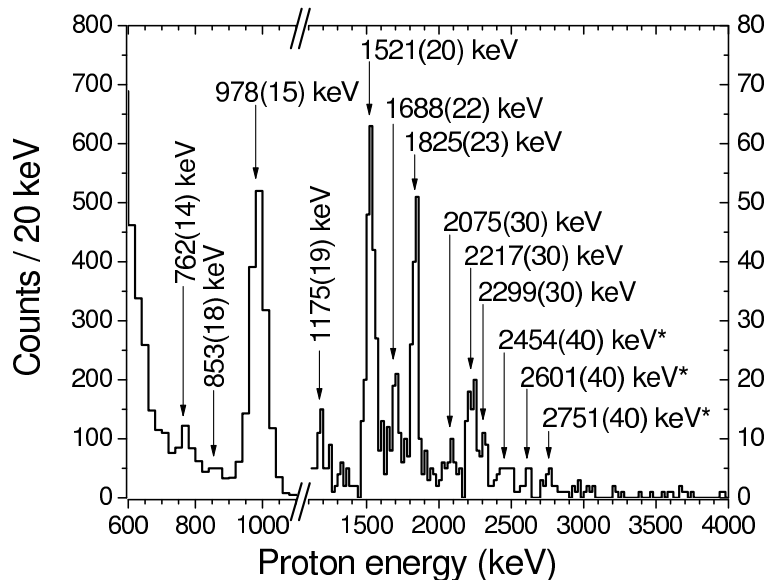


**Figure 4.6:** Beta-delayed protons from mass-separated  $^{31}\text{Cl}$ . The peaks marked with an asterisk are smaller than  $3\sigma$  peaks.

Although the energy difference between the 3536(2) keV and 4045(2) keV peaks is close to 511 keV, there should be no escape peaks or sum peaks. The relative intensity of the 4045 keV transition is about 50 % of the intensity of the 3536 keV transition (see table 4.2). Thus, the 3536 keV peak cannot be an escape peak from the 4045 keV peak. If the 4045 keV peak is due to random summing of 511 keV  $\gamma$ -rays and the 3536 keV  $\gamma$ -rays, it would mean that about 40 % of the 3536 keV  $\gamma$ -rays are summed with the 511 keV  $\gamma$ -rays. That intensive summing has not been observed with other known peaks in the spectrum, such as with the 1266 keV peak of  $^{31}\text{S}$ .

### 4.1.2 Beta-delayed protons

Beta-delayed protons were observed with the DSSSDs. The ISOLDE Silicon Ball and the thick silicon detectors behind the DSSSDs were used to detect beta particles which triggered the data acquisition. The energy calibration was done as described in sec. 3.2.3 and all valid calibrated DSSSDs were summed together. Figure 4.6 shows a proton spectrum in 20 keV bins. The proton energies agree well with the previous values [Äys85] after adjusting the energy calibration with the peak at 986 keV (see table 4.3). As this spectrum is measured from a mass-separated source, it can be concluded that the earlier controversial proton peaks are indeed from  $^{31}\text{Cl}$  and not from  $^{25}\text{Si}$  as was claimed in [Ogn96].

The biggest surprise in the spectrum is the peak at 762 keV which has not been observed before. This may be due to the fact that the previous experiments had no

**Table 4.2:** The relative peak intensities from the beta decay of  $^{31}\text{Cl}$ . The  $\gamma$ -peak at 2235 keV and the proton peak at 978 keV have been used for normalization. Corresponding values from refs. [Äys85] and [Ogn96] have been included for the known peaks. Peaks smaller than  $3\sigma$  have been marked with an asterisk.

E (keV)	$I_{\gamma+p}$ (%)	$I_p$ (%)	$I_p$ (%) [Äys85]	$I_p$ (%) [Ogn96]
$\gamma$ 1249.1(14)	32(7)			
$\gamma$ 2234.5(8)	100(12)			
$\gamma$ 3536(2)	26(8)			
$\gamma$ 4045(2)	14(6)			
p 762(14)	0.10(3)	9.1(22)		
p 853(18)	0.013(13)	1.2(12)	3(2)	
p 978(15)	1.08(14)	100(4)	100(2)	100
p 1175(19)	0.018(7)	1.7(6)	3(2)	
p 1521(20)	0.15(3)	13.6(14)	23(6)	11(5)
p 1688(22)	0.043(9)	3.9(7)	10(3)	
p 1825(23)	0.096(16)	8.8(11)	13(4)	
p 2075(30)	0.014(5)	1.3(5)	7(3)	
p 2217(30)	0.044(10)	4.1(8)	6(3)	
p 2299(30)	0.016(6)	1.5(5)		
p 2454(40)*	0.010(4)	1.0(4)		
p 2601(40)*	0.004(3)	0.4(3)		
p 2751(40)*	0.007(4)	0.6(3)		

mass separation and this peak has been identified to belong to the beta decay of  $^{32}\text{Cl}$ . The most intense proton peaks from the beta decay of  $^{32}\text{Cl}$  are 991(5) keV ( $I = 0.0113(17)$  %), 762(5) keV ( $I = 0.0052(8)$  %) and 1324(5) keV ( $I = 0.0052(8)$  %). As there is no peak at 1324 keV and there are no  $\gamma$ -rays belonging to the mass  $A = 32$ , this peak must originate from the beta decay of  $^{31}\text{Cl}$ . In addition, the proton energy of 762 keV corresponds to a known state at 6921(25) keV in  $^{31}\text{S}$  which has been observed via  $^{29}\text{Si} + ^3\text{He}$  reactions [Dav75] (see table 4.3).

The excitation energies of  $^{31}\text{S}$  were calculated from proton energies in the center of mass frame with a proton separation energy of 6133.0(15) keV and the latest mass values from [Aud03b]. Assuming that every decay goes to the  $^{30}\text{P}$  ground state, energy levels in agreement with the values from one or two nucleon transfer reaction data [Dav75, End78] are obtained. Beta-delayed alpha particles to the  $^{27}\text{Si}$  were considered as negligible due to a high alpha separation energy of 9085.3(15) keV [Aud03b]. The measured energies were averaged with the values from earlier beta decay experiments [Äys83, Äys85, Ogn96] and with the levels from transfer reactions [Dav75, End78] (see table 4.3). The energies from beta-decay experiments agree quite well with the energies from the transfer reactions except for the levels at 7347 keV and 8296 keV. The weighted averages of 7156(5) keV and 7713(7) keV levels are in agreement with

the values from one-nucleon pickup reactions by Vernotte *et al.* [Ver99], 7156(5) keV and 7725(5) keV. The latter level is suggested to be a multiplet of levels [Ver99].

### 4.1.3 Branching ratios

In the estimation of beta-decay branchings to the gamma-decaying states, a few things had to be considered. Firstly,  $\gamma$ - $\gamma$  coincidences could not be checked as only one HPGe detector was used. Secondly, the beta background was minimized by vetoing with the silicon detector in front of the HPGe detector. Although the veto condition revealed most of the interesting  $\gamma$  peaks hidden in the background, it removed also some relevant counts from the peaks due to random coincidences between beta particles and  $\gamma$  rays. In order to obtain the real number of counts for a peak visible only in the vetoed spectrum, the peak was scaled based on the 1266 keV  $\gamma$  peak from the  $^{31}\text{S}$  beta decay. The intensity ratio of the non-vetoed peak to the vetoed peak was 1.566(15). A very similar ratio of 1.56(3) was obtained with the 3134 keV gamma peak of  $^{31}\text{S}$ .

Previously, beta-decay branching to the 7156 keV state has been estimated to be 0.44 % based on the effective production cross section ratio of  $^{31}\text{Cl}$  and  $^{32}\text{Cl}$  at 45 MeV and 28 MeV and as given by the ALICE code [Äys85]. However, the latest ENSDF-files give a branching of 0.40(1) % to the 7.15 MeV state and 0.04(2) % to the 7.71 MeV state. This is based on [Ogn96] which claims that these are the only proton-emitting levels in  $^{31}\text{S}$ . In some of the older ENSDF-files the branching of 0.44 % has been taken as the total proton branching although an overall proton branching of about 0.7 % is given in ref. [Äys85]. In this work, absolute beta-decay branchings were obtained by fixing the intensity of the 978 keV protons to 0.44(3) %. This yielded a total proton branching of 0.65(5) %. Table 4.2 shows the relative intensities for protons (100 % for the 978 keV protons) and gammas (100 % for the 2235 keV gammas). The difference between the relative proton peak intensities of [Äys85] and this work may be explained by the lack of mass separation and possible unidentified activities in the previous work.

The absolute branchings are given in fig. 4.7. The branching to the IAS has been estimated to about 24.3 % with a complete *sd*-space shell model [Mut91]. In a similar manner, a pure single particle estimate for the Fermi and Gamow-Teller decay probabilities (see eqs. 2.11, 2.13 and 2.14) yields a  $\log ft$  of 3.20 and a branching of 23 % to the IAS as was calculated already in [Äys82]. The beta decay from  $^{31}\text{Cl}$  ( $T_Z = -3/2$ ) to the ground state of  $^{31}\text{S}$  ( $T_Z = -1/2$ ) was estimated with the analogous beta decay of  $^{31}\text{Si}$  ( $T_Z = +3/2$ ) to the ground state of  $^{31}\text{P}$  ( $T_Z = +1/2$ ) for which a  $\log ft$  of 5.52(2) [End98] and a beta-decay  $Q$ -value of 1491.88(19) keV [Aud03b] have been measured. The  $\log ft$  value for the beta decay of  $^{31}\text{Cl}$  to the ground state of  $^{31}\text{S}$  was determined with equation 4.1 [Har71]:

**Table 4.3:** The energy levels of  $^{31}\text{S}$ . The proton energies from [Äys83] (989(15) keV, 1528(20) keV) and from [Ogn96] (986(10) keV, 1524(10) keV) have been taken into account in the calculations of average proton energies  $\overline{E}_p$  and average excitation energies  $\overline{E}_x$ . The excitation energies from one or two nucleon transfer reactions are from [End78] for the states below 7.8 MeV and from [Dav75] for other levels. Peaks smaller than  $3\sigma$  have been marked with an asterisk.

$E_p$ (keV) this work	$E_p$ (keV) [Äys85]	$\overline{E}_p$ (keV)	$E_x$ (keV) this work	$E_x$ (keV) [Äys85]	$E_x$ (keV) [Dav75],[End78]	$\overline{E}_x$ (keV) protons	$\overline{E}_x$ (keV) all
762(14)			6921(15)		6921(25)		6921(13)
853(18)	845(30)	851(16)	7015(19)	7006(30)	6996(15)	7012(16)	7004(11)
978(15)	986(10)	985(6)	7144(16)	7152(10)	7165(9)	7151(6)	7156(5)
1175(19)	1173(20)	1174(14)	7348(20)	7345(20)	7310(11)	7347(14)	7324(9)
1521(20)	1520(15)	1523(8)	7705(21)	7704(15)	7730(12)	7707(8)	7713(7)
1688(22)	1695(20)	1692(15)	7878(23)	7885(20)	7888(25)	7882(15)	7884(13)
1825(23)	1827(20)	1826(15)	8019(24)	8021(20)	7985(25)	8021(16)	8011(13)
2075(30)	2113(30)	2092(20)	8278(30)	8317(30)	8362(25)	8296(21)	8322(16)
2217(30)	2204(30)	2211(20)	8425(30)	8411(30)	8453(25)	8418(21)	8432(16)
2299(30)			8509(30)				
2454(40)*			8669(40)*				
2601(40)*			8821(40)*				
2751(40)*			8977(40)*				

**Table 4.4:** A comparison of de-excitation of selected levels in  $^{31}\text{S}$  and  $^{31}\text{P}$ . The literature values are taken from [End98]. The subscripts represent the energies of the final states in keV. The energy and spin assignments marked with an asterisk have been taken from [Ver99].

$^{31}\text{S}$			$^{31}\text{P}$		
$E_x$ (keV)	$J^\pi$	$E_\gamma$ (keV), this work	$E_x$ (keV)	$J^\pi$	$E_\gamma$ (keV) ( $I_\gamma$ (%))
1248.9(2)	$1/2^+$	$\gamma_0$ 1249.1(14)	1266.15(10)	$3/2^+$	$\gamma_0$ 1266.12(100)
2235.6(4)	$5/2^+$	$\gamma_0$ 2234.5(8)	2233.7(2)	$5/2^+$	$\gamma_0$ 2233.6(100), $\gamma_{1266}$ 967.5(<0.1)
5777(5)*	$5/2^{+*}$	$\gamma_{2236}$ 3536(2)	5892.3(6)	$5/2^{+*}$	$\gamma_{2234}$ 3658.3(100), $\gamma_{3134}$ 2758.0(<11), $\gamma_{3415}$ 2477.5 (9.9), $\gamma_{1266}$ 4625.7(<5.5), $\gamma_0$ 5891.6(<5.5), $\gamma_{3295}$ 2597.1(<3.3)
6268(10)	$3/2^+$ , T=3/2	$\gamma_{2236}$ 4045(2)	6380.8(17)	$3/2^+$ , T=3/2	$\gamma_{2234}$ 4146.8(100), $\gamma_{3295}$ 3085.6(22), $\gamma_{1266}$ 5114.1(20), $\gamma_0$ 6380.0(20), $\gamma_{3415}$ 2966.0(<3.7)

$$\begin{aligned}\delta &= \frac{ft^+}{ft^-} - 1 \\ &= 5.2 \times 10^{-3}(W_0^+ + W_0^-)MeV^{-1}\end{aligned}\tag{4.1}$$

in which  $W_0^+$  and  $W_0^-$  are the total decay energies of the positron and electron decays, respectively.

Equation 4.1 yielded  $\delta = 0.07$  and  $\log ft^+ = 5.55(4)$ . As in ref. [Har71], a large error was assumed for  $\delta$ ,  $\delta = 0.07 \pm 0.10$ . With a  $\log f^+ = 5.22(5)$  taken from  $\log f$  tables [Gov71], a beta-decay branching of 7(2) % was estimated. A very similar procedure was used in [Axe98] in which an upper limit of 78 % for the beta-decay branching to the 2236 keV state was calculated.

The  $\log ft$  values obtained here are between 4.5–6.5 and thus, the observed transitions result most likely from allowed beta decays. Taking into account the ground-state spin of  $^{31}\text{Cl}$ ,  $3/2^+$ , spins of  $1/2^+$ ,  $3/2^+$  or  $5/2^+$  are suggested to these states in  $^{31}\text{S}$ . The spin of the state at 6996 keV has been fixed to  $1/2^+$ ,  $T = 1/2$  and the state at 7165 keV is  $(3/2^+, 5/2^+)$  according to [End78]. The state observed at 7015(19) keV has been taken as the 6996 keV state as in [Ays85] but it could also correspond to the state at 7039(10) keV  $(3/2^+, 5/2^+)$  [End78].

It should be taken into account that if the 3536 keV and 4045 keV transitions do not go to the state at 2236 keV, then the beta-decay branching to this state will change. If the 3536 keV gamma transition is excluded, the branching to the 2236 keV state is 35(7) % and the corresponding  $\log ft$  value will be 4.29(12). If the feeding from the IAS is neglected, the branching to the 2236 keV state will be 30(7) % and the  $\log ft$  4.35(13). If both transitions are rejected, then the branching and  $\log ft$  to the state at 2236 keV will be 41(6) % and 4.23(11), respectively. As a summary, the branching to the state at 2236 keV lies between 25–41 % and the  $\log ft$  is 4.23–4.44.

#### 4.1.4 Discussion

Shell-model calculations for  $sd$ -shell nuclei, such as  $^{31}\text{S}$ , have been carried out extensively in the past (see, *e.g.*, [Ver99]). According to the shell-model calculations, the beta decay of  $^{31}\text{Cl}$  has a strong Gamow-Teller feeding to the states around 8 MeV in  $^{31}\text{S}$  with a width of about 3–4 MeV [Äys85]. This is in agreement with the observation of beta decay to the proton-emitting states around 7–8 MeV in this experiment. The calculations [Äys85] also predict small Gamow-Teller decay strengths to the states at 1249 keV and at 2236 keV in agreement with the results of this work. Beta-decay feedings to the states around 3 MeV and 4.0–4.5 MeV have also been suggested in

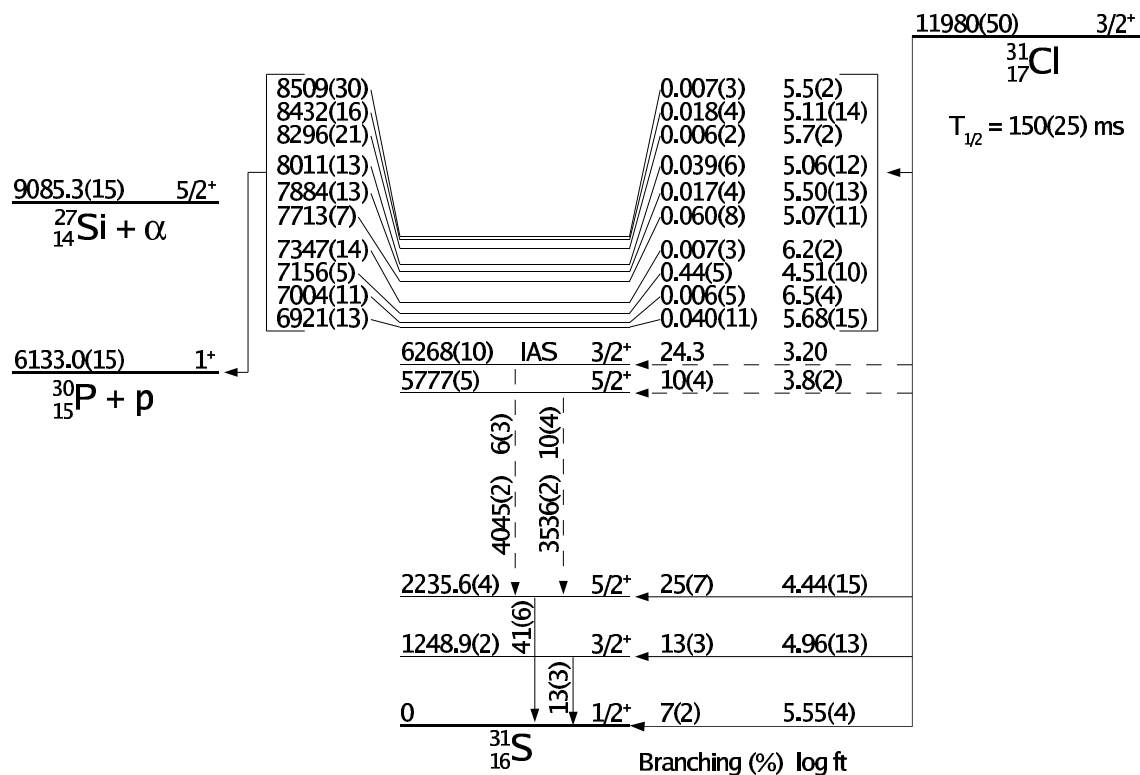


**Figure 4.7:** A beta-decay scheme of  $^{31}\text{Cl}$ . Only relevant energy levels of  $^{31}\text{S}$  are shown. The energies of proton-emitting levels have been averaged with the known values from refs. [Äys83], [Äys85], [Ogn96], [Dav75] and [End78]. The levels at 7347 keV and 8296 keV have been averaged only with the values from beta decay experiments [Äys85, Ogn96] due to too large energy differences to the values of [Dav75] and [End78]. The energies of the  $\gamma$ -emitting levels are from ref. [End90] except for the 5777(5) keV state [Ver99]. The branching to the ground state is an estimate based on the mirror decay. A theoretical estimation of the branching to the IAS [Mut91] is given together with a single particle estimate for the  $\log ft$  [Äys82]. Spins of the proton-emitting states are ( $1/2^+ - 5/2^+$ ) except  $1/2^+$  for the state at 7004 keV and ( $3/2^+$ ,  $5/2^+$ ) for the state at 7156 keV.

[Äys85]. The observed transitions of 3536 keV and 4045 keV fit into this region, but there are no known levels at these energies.

$^{31}\text{S}$  provides an opportunity to study mirror energy differences between the states of  $^{31}\text{S}$  and  $^{31}\text{P}$ . The 1249 keV and 2236 keV gamma transitions of  $^{31}\text{S}$  observed in this work were also detected in [Jen05]. The corresponding mirror states in  $^{31}\text{P}$  lie at energies of 1266 keV and 2234 keV (see table 4.4). Assuming that the observed 3536(2) keV transition goes to the state at 2236 keV, an energy of 5772(2) keV is obtained for the initial state in  $^{31}\text{S}$ . This agrees with the previous value of 5777(5) keV [Ver99]. The mirror state of the 5777 keV level is suggested to lie at 5892 keV in  $^{31}\text{P}$  [Ver99]. A spin of  $5/2^+$  is proposed for these states in  $^{31}\text{S}$  and  $^{31}\text{P}$  [Ver99] which differs from the spin assignments of  $(3/2^+, 5/2^+)$  and  $9/2^+$  adopted in [End98], respectively. The dominant decay mode of this state at 5892 keV in  $^{31}\text{P}$  is to the state at 2234 keV which agrees with the observation of the 3536 keV transition to the state at 2236 keV in  $^{31}\text{S}$ .

Based on the mirror states in  $^{31}\text{P}$ , one could expect that the IAS in  $^{31}\text{S}$  decays dominantly to the state at 2236 keV (see table 4.4). The decay to the ground state or to the state at 3286 keV (mirror to the state at 3295 keV in  $^{31}\text{P}$ ) were not observed in this experiment. The decay to the state at 1249 keV could be possible as this peak was observed but the feeding could not be checked due to the lack of  $\gamma$ - $\gamma$  coincidences. Assuming that the observed  $\gamma$ -transition with an energy of 4045(2) keV is from the IAS to the state at 2236 keV, an energy of 6280(2) keV is obtained for the IAS. This value does not agree with the literature value of 6268(10) keV at the  $1\sigma$  level, but is nevertheless in good agreement with predictions from the isobaric multiplet mass equation (IMME). Namely, IMME with the latest mass values of  $^{31}\text{Si}$ ,  $^{31}\text{P}$  and  $^{31}\text{Cl}$  [Aud03b] gives an energy of 6278(17) keV for the IAS and the IMME coefficients [Bri98] yield an energy of 6272(12) keV.

Since the energies and spins of the excited states of  $^{31}\text{S}$  have not been known so well, the reaction rate of  $^{30}\text{P}(p,\gamma)$  in ONe novae has been calculated using a statistical model calculation [Rau00]. However, the reaction rate will be most likely dominated by single resonances and direct captures [Jos01]. In order to calculate the reaction rate for individual resonances, corresponding resonance energies, spins of the final states and proton and gamma decay widths should be known. In this work, a new proton peak has been found at an energy of 762 keV (corresponding to a state at 6921 keV in  $^{31}\text{S}$ ), the controversial proton peaks have been confirmed and spin estimates for these states have been given based on the allowed beta decay. These can be later used for resonance calculations.

The observed 762 keV protons from the 6921 keV state may play a role in the proton capture rate on  $^{30}\text{P}$ . The Gamow window for the proton capture on  $^{30}\text{P}$  suggests that the proton captures to the IAS in  $^{31}\text{S}$  ( $E_{CM}=135$  keV) should be dominant at lower

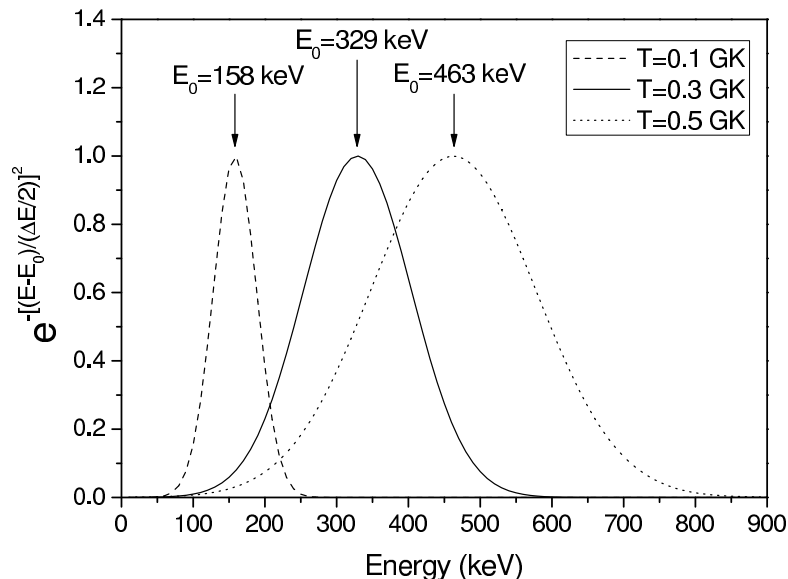


**Figure 4.8:** Gamow windows for proton capture on  $^{30}\text{P}$  at  $T=0.1$  GK,  $0.3$  GK and  $0.5$  GK. The peaks have been approximated with a Gaussian which has a maximum value of 1 at centroid  $E_0$  and a width  $\Delta E$  at  $1/e$  ( $\approx 0.37$ ) (see, *e.g.*, [Ang99]). At a typical temperature of  $T=0.3$  GK in ONe novae, the Gamow peak is centered at  $329$  keV and has a width of  $213$  keV at  $1/e$  of the maximum. The curves at  $T=0.1$  GK and  $T=0.5$  GK are plotted in order to show the effect of the temperature on the Gamow peak. The currently estimated peak temperature in novae is  $T \leq 0.4$  GK [Jos06].

temperatures whereas captures to the  $6921$  keV state ( $E_{CM}=788$  keV) can contribute more at higher temperatures as shown in fig. 4.8. On the other hand, proton captures to the IAS are isospin forbidden and possible only via isospin mixing. This may hinder strong population of the IAS via reactions other than beta decay. More experiments on the beta decay of  $^{31}\text{Cl}$  should be done with high-efficiency HPGe detectors in order to confirm the observed gamma decay and to search for other gamma decays from the IAS. Novel detectors for detecting low-energy protons from the IAS should be applied for the estimation of the proton width of the IAS. The resonance strength could then be determined from the gamma, proton and total widths of the IAS.

## 4.2 Beta decay of $^{58}\text{Zn}$ and isospin symmetry of transitions

Beta decay of  $^{58}\text{Zn}$  provides information on the Gamow-Teller strength of the transitions to the daughter nucleus  $^{58}\text{Cu}$ . This strength can be compared to the strength of analogous transitions from  $^{58}\text{Ni}$  to  $^{58}\text{Cu}$  studied via charge-exchange reactions (see sec. 2.2.4). Although beta decay of more exotic  $^{57}\text{Zn}$  has been thoroughly explored [Jok02], surprisingly little is known about the beta decay of  $^{58}\text{Zn}$ . Only one successful

experiment [Jok98] has been done before this thesis work. In that work, de-excitations of the 203 keV and 1051 keV levels in  $^{58}\text{Cu}$  were observed with  $\gamma$ -energies of 203 keV and 848 keV and the half-life was determined as 86(18) ms from the time behavior of the 203 keV  $\gamma$ -transition. Later, the half-life of 83(10) ms has been measured for  $^{58}\text{Zn}$  produced in the fragmentation of a  $^{78}\text{Kr}$  beam at GANIL [Lóp02]. The  $Q_{EC}$  value of 9370(50) keV for the beta decay of  $^{58}\text{Zn}$  has been determined via pion double charge-exchange reactions  $^{58}\text{Ni}(\pi^+, \pi^-)^{58}\text{Zn}$  several years ago [Set86].

Charge-exchange studies have revealed several strong GT transitions from  $^{58}\text{Ni}$  to the states in  $^{58}\text{Cu}$ . A strong feeding to the  $J^\pi = 1^+, T = 0$  state at 1051 keV is observed in a high-resolution  $^{58}\text{Ni}(^3\text{He}, t)^{58}\text{Cu}$  spectrum measured at  $0^\circ$  [Fuj02b] (see fig. 4.9). This state lies below the proton separation energy  $S_p = 2869.1(23)$  keV [Aud03b] and thus, can only decay via  $\gamma$  decay. The states at 3460 keV and 3678 keV above the proton separation energy are also quite strongly populated. As these states lie only slightly above the  $S_p$ ,  $\gamma$  decay may compete with the decay via proton emission from these states. For the states at higher energies, such as for the strongly fed state at 5160 keV, decay via proton emission is much more favorable. The expected proton energy should be around 2.2 MeV.

The decay properties of the states in  $^{58}\text{Cu}$  have been studied in a charge-exchange experiment via  $^{58}\text{Ni}(^3\text{He}, t + \gamma)$  and  $^{58}\text{Ni}(^3\text{He}, t + p)$  coincidences [Har03]. In that experiment,  $\gamma$  transitions with energies of 203 keV, 444 keV, 848 keV and 3475 keV were identified in coincidence with tritons. Peaks from the de-excitations of the states around 3.5 MeV in  $^{58}\text{Cu}$  could not be resolved. However, the coincidences were studied by gating with a lower part (3.17–3.62 MeV) and an upper part (3.62–4.20 MeV) of the unresolved peak at around 3.5 MeV in  $^{58}\text{Cu}$ . In this way,  $\gamma$  transitions with energies of 203 keV ( $0^+_{IAS} \rightarrow 1^+_{g.s.}$ ), 444 keV ( $3^+_1 \rightarrow 1^+_{g.s.}$ ), 3257 keV ( $1^+, 3460$  keV  $\rightarrow 0^+_{IAS}$ ) and 3475 keV ( $1^+, 3678$  keV  $\rightarrow 0^+_{IAS}$ ) were identified.

Proton decays from excited states above about 4 MeV in  $^{58}\text{Cu}$  were observed in  $^{58}\text{Ni}(^3\text{He}, t + p)$  coincidences [Har03]. For the states above about 8 MeV in  $^{58}\text{Cu}$ , proton decays to the  $3/2^-$  ground state,  $5/2^-$  state at 769 keV,  $1/2^-$  state at 1112 keV,  $7/2^-$  ( $T = 1/2$ ) state at 2578 keV and  $7/2^-$  ( $T = 3/2$ ) state at around 5.2 MeV in  $^{57}\text{Ni}$  were also observed as  $\gamma$  transitions de-exciting the corresponding states in  $^{57}\text{Ni}$ . However, protons from the states around 3.5 MeV in  $^{58}\text{Cu}$  could not be detected due to electronic noise threshold in [Har03]. The study of the excited states in the region from 3 MeV to 9 MeV in  $^{58}\text{Cu}$  via beta decay of  $^{58}\text{Zn}$  would give information on the decay properties and GT strengths of these states.

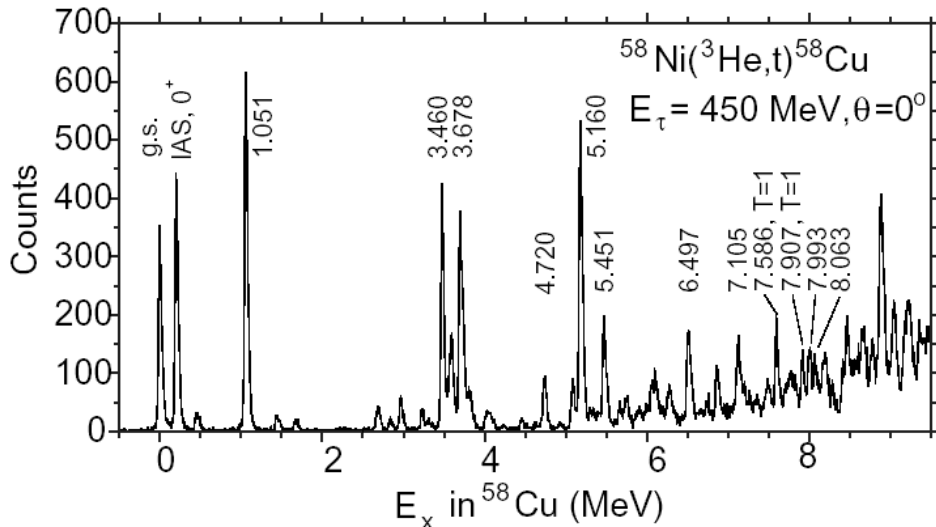


**Figure 4.9:**  $^{58}\text{Ni}(^3\text{He},t)^{58}\text{Cu}$  spectrum measured at  $0^\circ$  from [Fuj02b]. Excitation energies for the major states with  $L = 0$  character are indicated. The error of the excitation energies is  $\pm 10$  keV for the states below 5 MeV  $\pm 20$  keV for the states in the 8 MeV region.

#### 4.2.1 Beta-delayed $\gamma$ rays and half-life of $^{58}\text{Zn}$

Beta-delayed  $\gamma$  rays from  $^{58}\text{Zn}$  were detected with the setup described in sec. 3.2.1. Peaks at 203 keV and 848 keV already observed in [Jok98] were seen in a  $\gamma$  spectrum without any gates. With a time gate of 10–400 ms applied to a  $\gamma$  spectrum in coincidence with beta particles, the contribution of much longer-lived and better produced isobaric contaminants  $^{42}\text{ScO}$  and  $^{58}\text{Mn}$  could be reduced (see fig. 4.10). Unfortunately, no other  $\gamma$  transitions except those of 203.4(5) keV and 846.8(8) keV could be observed in the spectrum.

The expected high-energy  $\gamma$  transitions were searched for by subtracting from a beta-gated  $\gamma$  spectrum gated by time (10–400 ms) a corresponding spectrum gated by a later time (400–790 ms). In this way, the contribution of short-lived  $^{58}\text{Zn}$  should be seen easily. However, no other peaks than those of the 203 keV and 848 keV transitions were observed. The non-observation of the 444 keV  $\gamma$  peak ( $3_1^+ \rightarrow 1_{g.s.}^+$ ) could be explained as it is lying in the large Compton continuum below the 511 keV annihilation peak. The intensities of the other  $\gamma$  transitions observed in [Har03] (3257 keV and 3475 keV) were estimated based on the relative peak intensities, which were expected from the branching ratios of the higher-lying states (based on the  $B(\text{GT})$  values of [Fuj06]) and  $\gamma$  detector efficiencies for the peaks. The estimated number of counts in the 3257 keV and 3475 keV peaks and the number of counts per channel in the background showed that the visibility of these peaks should be around  $2\sigma$ . According to [Kan95], statistical fluctuations produce typically some tens of  $2\sigma$  peaks

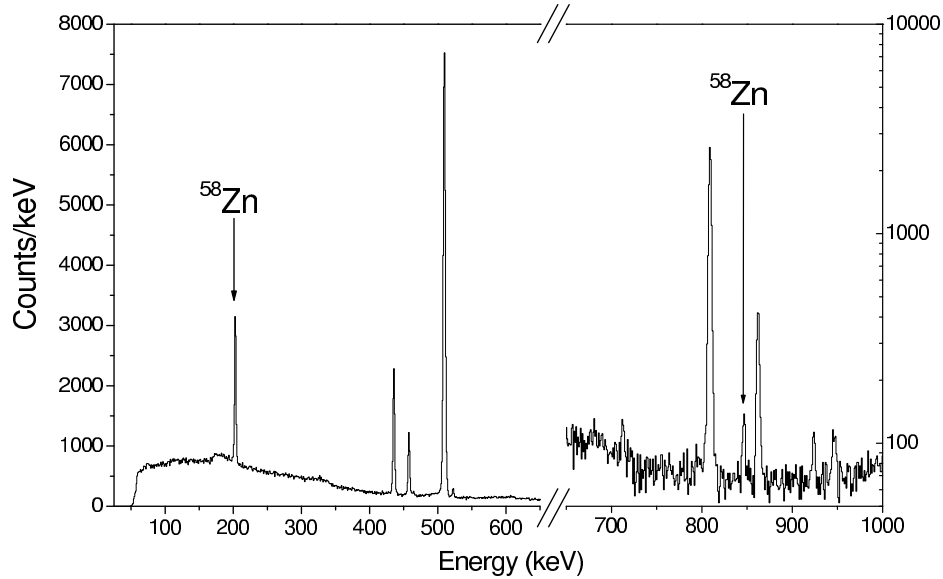


**Figure 4.10:** Beta- and time-gated (10–400 ms)  $\gamma$ -spectrum from the beta decay of  $^{58}\text{Zn}$ . The observed 203 keV and 848 keV peaks are labeled as  $^{58}\text{Zn}$ . The other peaks are from the beta decays of contaminant  $^{42}\text{ScO}$  and  $^{58}\text{Mn}$  or from the background. Note the logarithmic scale after the break at 650 keV.

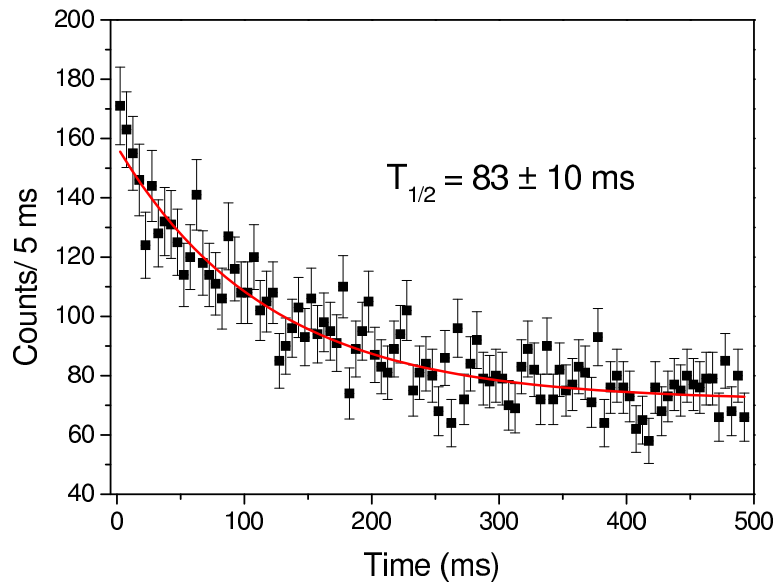


**Figure 4.11:** The time behavior of the 203 keV  $\gamma$  peak. The decay fit gave a half-life of 83(10) ms when the normalized  $\chi^2$  was optimized.

in this kind of spectrum. Therefore, it can be concluded that the peaks had too low intensities to be properly detected in the  $\gamma$  spectrum.

The half-life is crucial in the determination of  $\log ft$  values for the beta decay of  $^{58}\text{Zn}$ . In this experiment, a half-life of 83(10) ms ( $\chi^2=0.8$ ) was obtained by fitting

an exponential decay curve with a constant background to the time behavior of the 203 keV  $\gamma$  peak (see fig. 4.11). The adopted value was obtained from a fit with a minimum  $\chi^2$ . A simple exponential decay fit to the time behavior of the 203 keV peak after background subtraction from both sides of the peak gave larger errors. Half-life fits on the time behavior of  $\beta^+$  particles were not suitable due to the much more intense contaminant activity of  $^{42}\text{ScO}$ . The measured half-life agrees perfectly with the previous values of 86(18) ms [Jok98] and 83(10) ms [Lóp02]. An error-weighted average from these experiments, 83(7) ms, was used in the calculation of  $\log ft$  values. The corresponding  $\log f$  values were computed with the  $\log ft$  calculator found in [NNDC].

### 4.2.2 Branching ratios and GT strengths

The beta decay from the ground state of  $^{58}\text{Zn}$  ( $J^\pi=0^+$ ,  $T=1$ ) to the IAS ( $J^\pi=0^+$ ,  $T=1$ ) at 203 keV in  $^{58}\text{Cu}$  is a pure Fermi transition with  $B(F)=2$  and  $B(GT)=0$ . The beta-decay branching ratio to the IAS can be calculated from eq. 2.15,  $b_{IAS} = 72(7)\%$ . The branching ratio to the ( $J^\pi=1^+$ ,  $T=0$ ) state at 1051 keV can be derived from the relative intensities of the 203 keV ( $I_\gamma = 100(13)\%$ ) and 848 keV  $\gamma$  peaks ( $I_\gamma=9.9(21)\%$ ),  $b_{1051keV} = 7.9(20)\%$ . In the calculation of this branching ratio, it was assumed that the level at 1051 keV is not fed from higher states in  $^{58}\text{Cu}$ ,  $I_{848keV} = b_{1051keV}$ , and that the IAS at 203 keV is only fed from the 1051 keV state,  $I_{203keV} = b_{IAS} + b_{1051keV}$ . As a consequence, the branching ratio of the ground state must be  $b_{g.s.} \leq 20(9)\%$ . A proposed decay scheme is shown in fig. 4.12. The branching ratios are in agreement with  $b_{IAS}=74(16)\%$  and  $b_{1051keV}=12(6)\%$  from [Jok98].

In CE reaction studies, GT strengths to discrete states up to 8 MeV in  $^{58}\text{Cu}$  have been measured [Fuj02b, Fuj06]. The GT strength to the ground state used in CE reactions is based on the ground state  $\beta^+$  decay of  $^{58}\text{Cu}$  ( $J^\pi=1^+$ ,  $T=1$ ) [Per01b, Jan01]. From the measured GT strengths, beta-decay branching ratios can be estimated to the states in  $^{58}\text{Cu}$ . The branching ratios based on the GT strengths of [Fuj06] are  $b_{g.s.}=10.0(9)\%$  and  $b_{1051keV}=8.4(9)\%$  in agreement with the beta-decay values (see table 4.5). The total sum of the observed GT branching ratios is 21.1(21)% in [Fuj06] indicating a branching of 78.9(21)% to the Fermi decays in agreement with the branching ratio of 72(7)% obtained for the Fermi beta decay to the IAS in this work.

The GT strengths from [Fuj06], estimated branching ratios and proton energies for the states in  $^{58}\text{Cu}$  fed by more than 0.1% are collected in table 4.5. The energies for protons from the states below 3.8 MeV [Fuj06] are less than 900 keV and thus, the  $\gamma$  decay may compete with the proton decay channel. However, the estimated branching ratios to states in the region of 2655 keV–3783 keV are so small that the possible feeding of the IAS from these states can be neglected. The estimated total beta-decay branching above the proton separation energy is 2.5(3)%.

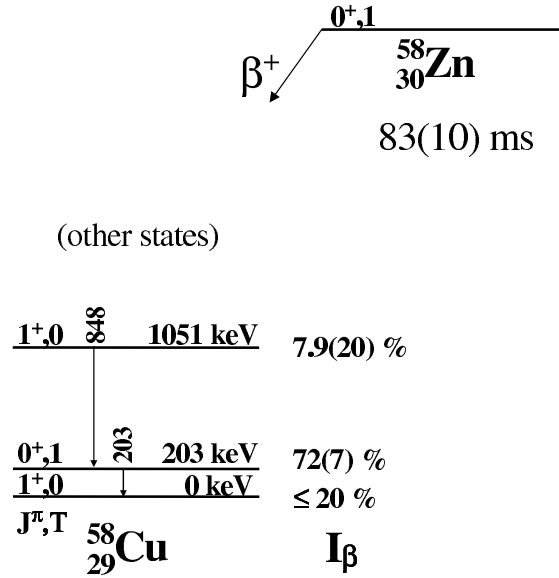


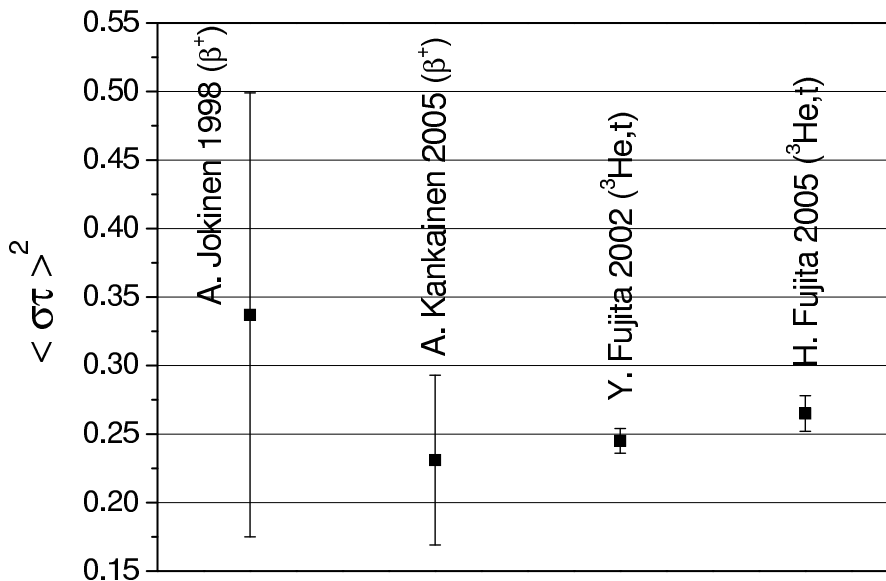
**Figure 4.12:** A decay scheme for the beta decay of  $^{58}\text{Zn}$  based on this experiment.

**Table 4.5:** The GT strength  $\langle \sigma\tau \rangle^2$  [Fuj06], estimated branching ratios and proton energies (in laboratory frame) to the states which should be fed by more than 0.1% in  $^{58}\text{Cu}$ . The error in the energies is about 10 keV according to [Fuj06]. The GT strength to the ground state is based on [Per01b, Jan01].

$E_x$ (keV) [Fuj06]	$\langle \sigma\tau \rangle^2$ [Fuj06]	b(%)	$E_p$ (keV)
0	0.155(1)	10.0(9)	-
1053	0.245(9)	8.4(9)	-
2655	0.015(1)	0.161(19)	-
2944	0.025(2)	0.21(3)	74
3451	0.164(7)	0.88(10)	572
3668	0.157(4)	0.68(7)	785
3706	0.047(2)	0.197(22)	822
3783	0.029(2)	0.112(14)	898
5143	0.250(2)	0.195(22)	2234

**Table 4.6:** The GT strength as  $B(GT)$  values and  $\langle \sigma\tau \rangle^2$  to the state at 1051 keV in  $^{58}\text{Cu}$ .

Reference	This work	[Jok98]	[Fuj02b]	[Fuj06]
$B(GT)$	0.37(10)	0.54(26)	0.393(15)	0.425(21)
$\langle \sigma\tau \rangle^2$	0.23(7)	0.34(17)	0.245(9)	0.265(13)

**Figure 4.13:** The GT strengths as  $\langle \sigma\tau \rangle^2$  from the beta decay of  $^{58}\text{Zn}$  and from  $^{58}\text{Ni}({}^3\text{He,t})^{58}\text{Cu}$  CE reactions.

The GT strength to the 1051 keV state can be calculated from eq. 2.15,  $B(GT)_{1051\text{keV}} = 0.37(10)$ . From the upper limit for the ground-state branching ratio, a GT strength  $B(GT)_{g.s.} \leq 0.50(22)$  can be estimated. If a corrected  $ft$  value (see eq. 2.12) is calculated using  $(1 + \delta_R) = 1.026$  [Ewa81] and  $(1 - \delta_C) = 0.997(3)$  [Wil78], branching ratios will be  $b_{IAS} = 74(7)\%$ ,  $b_{1051\text{keV}} = 8.1(21)\%$  and  $b_{g.s.} \leq 18(9)\%$ . These corrections do not change  $B(GT)_{1051\text{keV}}$  and  $B(GT)_{g.s.}$  is less than 0.45(22). As a summary, these corrections have only a small effect on the branching ratio to the IAS.

The  $B(GT)$  values in CE reaction studies refer to the square of the GT matrix element,  $\langle \sigma\tau \rangle^2$ . Thus, in order to compare the measured  $B(GT)$  values to the CE reactions,  $\langle \sigma\tau \rangle^2$  values have to be calculated with eq. 2.14. These values are collected in table 4.6. As it can be seen from fig. 4.13, the obtained GT strengths agree with each other. Although the precision of the GT strength from beta decay could be improved in this experiment, more precise measurements would be needed to show whether the isospin symmetry is broken in the  $A = 58$  triplet.

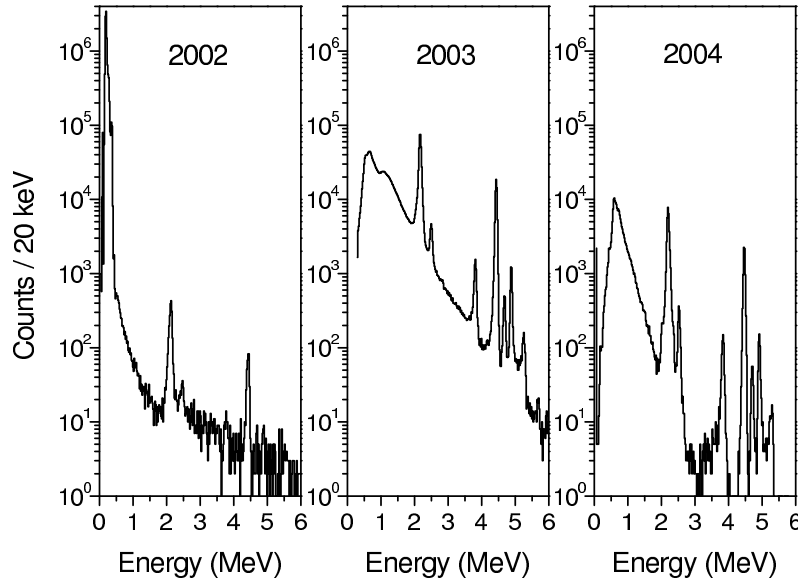


**Figure 4.14:** Beta-delayed  $\alpha$  particles from  $^{20}\text{Na}$  measured with the ISOLDE Silicon Ball in 2002 (ISOLDE), 2003 (ISOLDE) and 2004 (IGISOL). The peaks correspond to  $\alpha$  energies of 2150.4(19) keV, 2479.6(21) keV, 3799(3) keV, 4432.2(29) keV, 4675(3) keV, 4885(3) keV and 5249(4) keV of ref. [Cli89]. Only the most intense peaks at 2150 keV and 4432 keV were observed in 2002.

### 4.2.3 ISOLDE Silicon Ball and beta-delayed protons of $^{58}\text{Zn}$

Beta-delayed protons from  $^{58}\text{Zn}$  were searched for with the ISOLDE Silicon Ball and a single beta detector as described in sec. 3.2.2. The experiment was done twice at the ISOLDE facility, in 2002 and 2003, and once at IGISOL in 2004 mainly due to the problems with the  $^{58}\text{Zn}$  production.

For calibration purposes and for checking the performance of the ISOLDE Silicon Ball, beta-delayed alphas from  $^{20}\text{Na}$  produced on-line were measured with the Silicon Ball (see fig. 4.14). Well-known  $\alpha$  sources of  $^{148}\text{Gd}$ ,  $^{241}\text{Am}$ ,  $^{239}\text{Pu}$  and  $^{244}\text{Cm}$  were used for the primary calibration. At IGISOL, only  $^{148}\text{Gd}$  and  $^{241}\text{Am}$  sources were available. In the first experiment done with the Silicon Ball in 2002, only the two most intense peaks at 2150 keV and 4432 keV could be observed. In 2003 and 2004, altogether seven  $\alpha$  peaks could be detected. The full width at half maximum (FWHM) for the most intense peak at 2150 keV was 74(3) keV, 65(2) keV and 63(2) keV for the spectra in 2002, 2003 and 2004, respectively. However, the performance of the detector cannot be judged based on these spectra. The collection times and the silicon detectors included in the spectra were different in 2002, 2003 and 2004. In addition,  $^{20}\text{Na}$  was produced via spallation reactions in 2002 and 2003 and by fusion-evaporation reactions in 2004.

Proton spectra from  $^{58}\text{Zn}$  measured with the Silicon Ball are shown in figs. 4.15 and 4.16. The spectra are gated by the single beta detector opposite to the Silicon Ball.

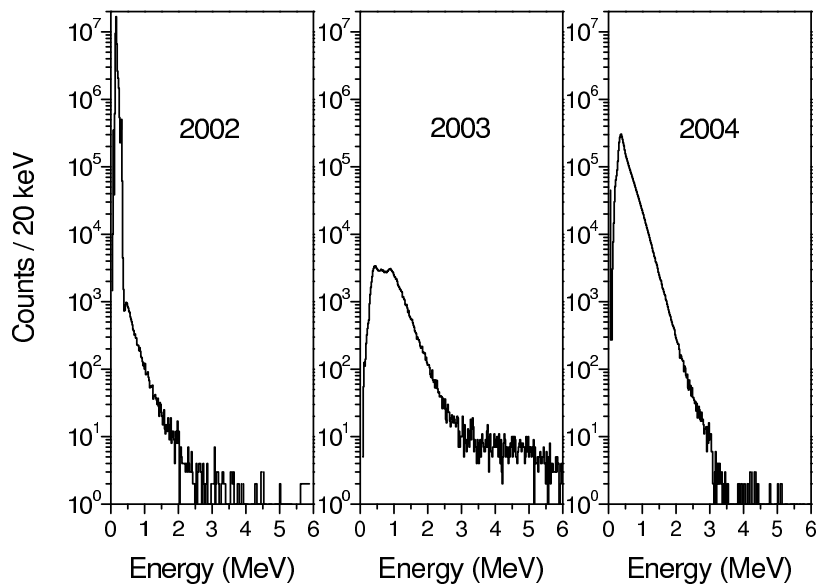


**Figure 4.15:** Beta-gated spectrum of  $^{58}\text{Zn}$  measured with the ISOLDE Silicon Ball in 2002 (ISOLDE), 2003 (ISOLDE) and 2004 (IGISOL). A time gate of about 10–400 ms was applied for the spectra in 2002 and 2003.

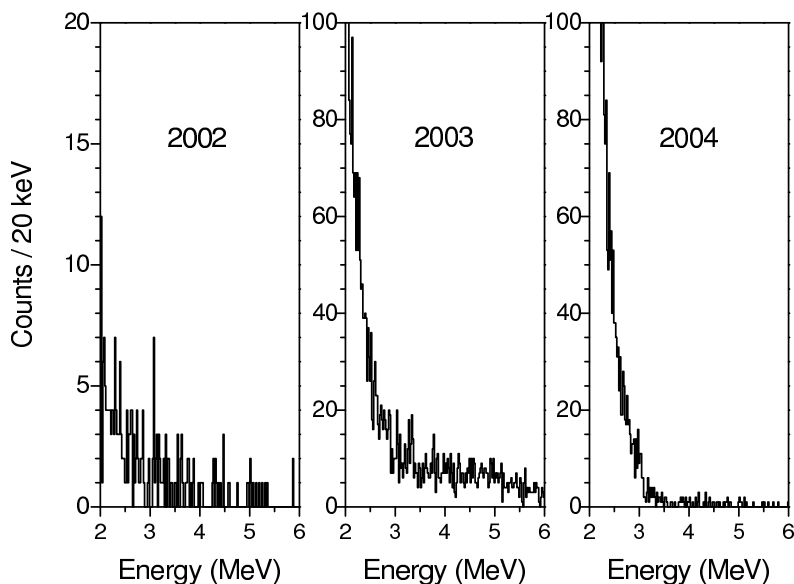


**Figure 4.16:** The spectra of fig. 4.15 above 2 MeV. No proton peak around 2.2 MeV was observed.

In 2002 and 2003, the spectra were also gated by time (about 10–400 ms). In 2004, the time gate was not possible as the beam was continuously implanted in an Al foil. As it can be seen in fig. 4.15, the spectrum has a continuum resulting from possible noise in the detectors and from  $\beta^+$  particles up to around 3 MeV. Partly due to this continuum, neither the expected proton peak around 2.2 MeV nor other proton peaks could be observed (see fig. 4.16).

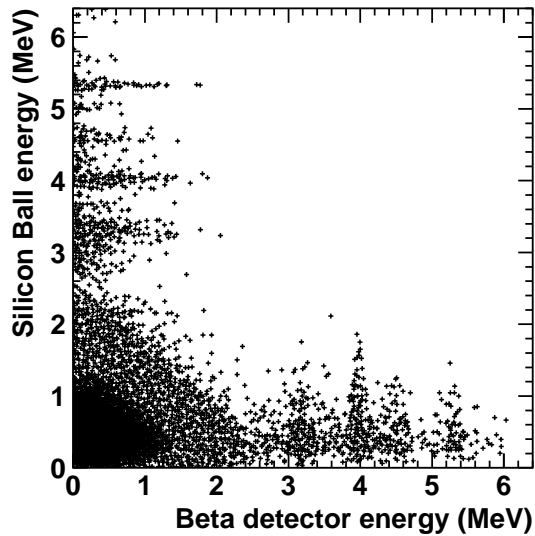


**Figure 4.17:** Events in the ISOLDE Silicon Ball versus the beta detector opposite to the Silicon Ball for  $^{25}\text{Si}$  in 2004 at IGISOL.

In order to distinguish  $\beta^+$  particles from protons, a 2D scatter plot of the events in the single beta detector versus the events in the Silicon Ball was plotted. An example of this kind of spectrum is shown for  $^{25}\text{Si}$  measured in 2004 at IGISOL (see fig. 4.17). By choosing only the events above the low-energy corner of the 2D spectrum, the  $\beta^+$  continuum could be rejected. However, this did not reveal any peaks below 2 MeV and an almost similar spectrum is obtained gating with the beta detector (see fig. 4.18). A similar 2D plot for  $^{58}\text{Zn}$  measured in 2004 is shown in fig. 4.19. The 2D plot does not show any potential peaks and applied 2D gates do not change the result.

The spectra from the experiments done in 2002 and 2003 could also be gated by time. The subtraction of a spectrum containing the longer-lived contaminant activities from the spectrum of short-lived  $^{58}\text{Zn}$  did not yield any new results. No proton peaks could be observed.

Based on the area of the 203 keV  $\gamma$  peak and on the estimated proton-decay branching, the amount of beta-delayed protons could be estimated. In the experiment done in 2004, about 150 protons could have been observed with the Silicon Ball. With the beta detector gate used, this reduces to about 40 protons. For the most probable proton peak at 2234 keV, this would mean only 3 counts with the beta gate and about 12 counts without the gate. The estimates for the experiments done in 2002 and 2003 are about the same. Taking into account the large continuums in the spectra, it would have been impossible to detect any proton peaks below 2.5 MeV. Above 3 MeV, the expected number of protons for individual peaks is much too small to be identified. In the future, pulse shape discrimination and time-of-flight techniques

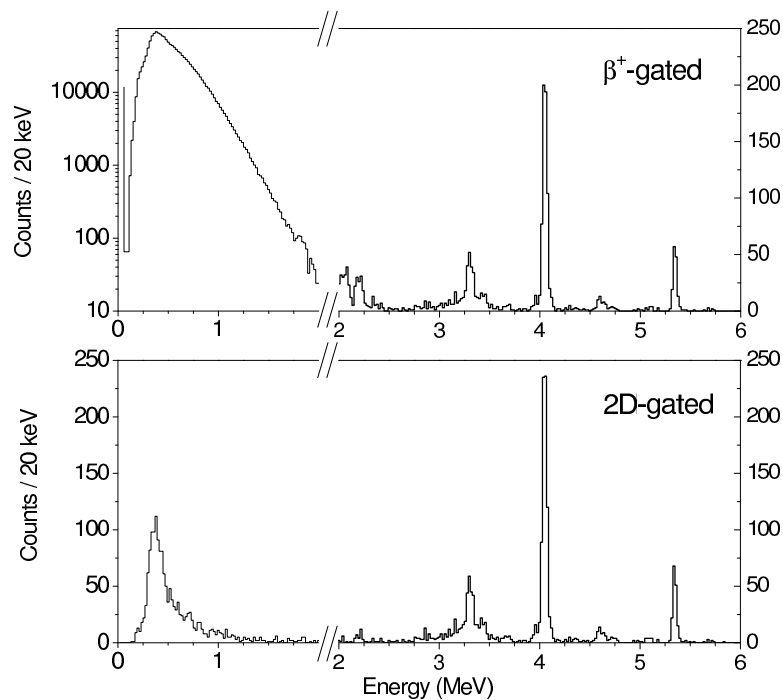


**Figure 4.18:** Beta-delayed protons from  $^{25}\text{Si}$  gated with the beta detector or with a 2D gate on fig. 4.17 in 2004 at IGISOL. Peaks corresponding the laboratory energies of 3323(3) keV, 4081(2) keV, 4654(6) keV and 5397(3) keV from ref. [Tho04] were observed.

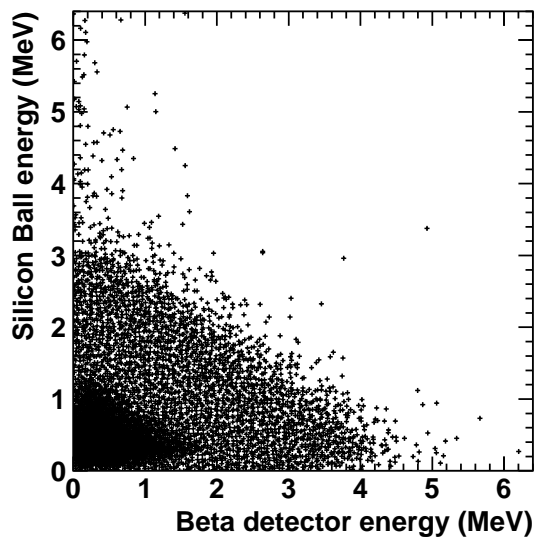


**Figure 4.19:** Events in the ISOLDE Silicon Ball versus the beta detector for  $^{58}\text{Zn}$  in 2004 at IGISOL.

suggested for particle identification in [Fra03] can help to identify protons from the large  $\beta^+$  background. The noise in the detectors could be reduced by cooling the Silicon Ball with  $\text{C}_3\text{F}_8$  liquid circulating in copper cooling pipes [Fra03]. The search for the protons from  $^{58}\text{Zn}$  could also be tried with Double-Sided Silicon Strip Detectors backed with thick Silicon detectors which could offer high granularity and identification of beta particles.

### 4.3 Search for $^{69}\text{Kr}$

In this thesis, the proton capture  $Q$ -value for  $^{68}\text{Se}$  was studied inversely by trying to determine the energies of the protons emitted from the states of  $^{69}\text{Br}$  populated by the beta decay of  $^{69}\text{Kr}$ . The proton capture  $Q$ -value is important for modeling the astrophysical rp process as described in sec. 2.3.1 and in fig. 2.6. Before this thesis work, beta decay of  $^{69}\text{Kr}$  had been observed only once [Xu97]. In that experiment, a single proton group with an energy of 4.07(5) MeV and a half-life of 32(10) ms was observed. The proton group was suggested to belong to the  $\beta$ -delayed proton decay from the  $T = 3/2$  IAS in  $^{69}\text{Br}$  to the ground state of  $^{68}\text{Se}$  and the beta-decay branching ratio to the IAS was deduced to be about 83 %. No protons from the ground-state proton decay of  $^{69}\text{Br}$  were observed in [Xu97] and thus, the proton separation energy could not be determined. Estimates on the proton separation energy show that  $^{69}\text{Br}$  should be proton unbound by at least 450 keV (see table 2.1).

With the  $\Delta\text{E}$ -E detector described in sec. 3.2.4, beta particles, protons and alpha particles can be identified as their energy losses in the  $\Delta\text{E}$  detector are different. In the data analysis, a 2D scatter plot of the events in the  $\Delta\text{E}$  detector versus the E detector were plotted and 2D gates for protons were applied. The energy calibrations were done on-line with protons of  $^{33}\text{Ar}$  and alpha particles from  $^{20}\text{Na}$  and off-line with a triple alpha source of  $^{239}\text{Pu}$ ,  $^{241}\text{Am}$  and  $^{244}\text{Cm}$ . Protons with energies roughly less than 1300 keV leave all of their energy in the  $\Delta\text{E}$  detector and thus, they are not in coincidence with the events in the E detector. Therefore, the events in the  $\Delta\text{E}$  detector were also checked in anticoincidence with the E detector.

No beta-delayed protons were observed with the  $\Delta\text{E}$ -E setup in about 22 hours of data acquisition. The beta-delayed protons from the IAS should have been observed with an energy of about 4.07 MeV [Xu97] and the protons from the ground state should have had an energy of less than 1 MeV (see table 2.1). The non-observation sets an upper limit of  $4.1 \times 10^{-4}$  atoms/ $\mu\text{C}$  (a  $3\sigma$  limit) for the yield of  $^{69}\text{Kr}$ .

The performance of the detector was also checked with  $^{71}\text{Kr}$  and  $^{73}\text{Kr}$ . The yields based on beta-delayed protons from these isotopes were 1.9 atoms/ $\mu\text{C}$  and  $7.4 \times 10^4$  atoms/ $\mu\text{C}$ , respectively. In the yield calculation, the branching of the beta-delayed

protons from  $^{71}\text{Kr}$  was taken as 2.1% [Oin97] and not as 5.2% [Bla95b]. The yields are consistent with the earlier reported values of  $2.6 \times 10^{-4}$  atoms/ $\mu\text{C}$  ( $^{69}\text{Kr}$ ) [Oin02], 1.7 atoms/ $\mu\text{C}$  ( $^{71}\text{Kr}$ ) [Oin97] and  $7.6 \times 10^4$  at/ $\mu\text{C}$  ( $^{73}\text{Kr}$ ) [Oin97].

The release parameters needed for the above yield calculations (see eq. 3.1) were fitted on data collected at a separate tape station for beta counting [Let97]. The released fractions for the isotopes were about 75% ( $^{73}\text{Kr}$ ), 1.3% ( $^{71}\text{Kr}$ ) and 0.2% ( $^{69}\text{Kr}$ ). The data were also corrected for the decay losses caused by the used beamgate (500 ms for  $^{73}\text{Kr}$ , 300 ms for  $^{71}\text{Kr}$  and 150 ms for  $^{69}\text{Kr}$ ).

The experiment on  $^{69}\text{Kr}$  provided also important information for the target development at ISOLDE. The Monte Carlo (MC) simulations on the Kr yields done by Santana Leitner could be compared to the experimentally measured released fractions. The MC simulations supported the conclusion that the used Nb target is not efficient enough for the production of  $^{69}\text{Kr}$ . The substitution of rolled Nb stripes with parallel thin Nb foils would at best double the yield of  $^{69}\text{Kr}$  mainly due to faster diffusion from the foils. Shorter average diffusion paths could be reached by using a fiber or powder target with a high cross section for  $^{69}\text{Kr}$ , such as  $\text{Y}_2\text{O}_3$ .

## 4.4 Isomers of astrophysical interest close to $A = 80$

Nuclei close to the  $A = 80$  region are particularly interesting because they are located at the rp-process path (see sec. 2.3.1 and fig. 2.7). In the following sections, spectroscopic results for masses  $A = 81$ , 85 and 86 are presented with an emphasis on the isomeric states. The masses of nuclei in this region are discussed separately in sec. 4.6.

### 4.4.1 $A=81$

The isotopes of interest at  $A = 81$  were produced via the reaction  $^{32}\text{S} + ^{54}\text{Fe} \rightarrow ^{86}\text{Mo}^*$ . The mass-separated beam from HIGISOL was implanted into a tape and accumulated for 15 s or 30 s at the first detector station (see sec. 3.2.5). A part of the low energy  $\gamma$ -spectrum measured by the LeGe detector at the second detector station is shown in fig. 4.20. This clean spectrum had no contaminants from neighboring masses and the most intense peaks used for the yield determination are easily seen.

Well-known  $K$ - and  $L$ -electron lines were identified in the internal conversion electron spectrum shown in fig. 4.21 and the 63.1 keV  $K$ -electron peak of the 79.2 keV transition in  $^{81}\text{Sr}$  was used for internal calibration. Conversion electrons from 43.0 keV and 221.0 keV transitions in  $^{81}\text{Sr}$  could be observed for the first time. The internal

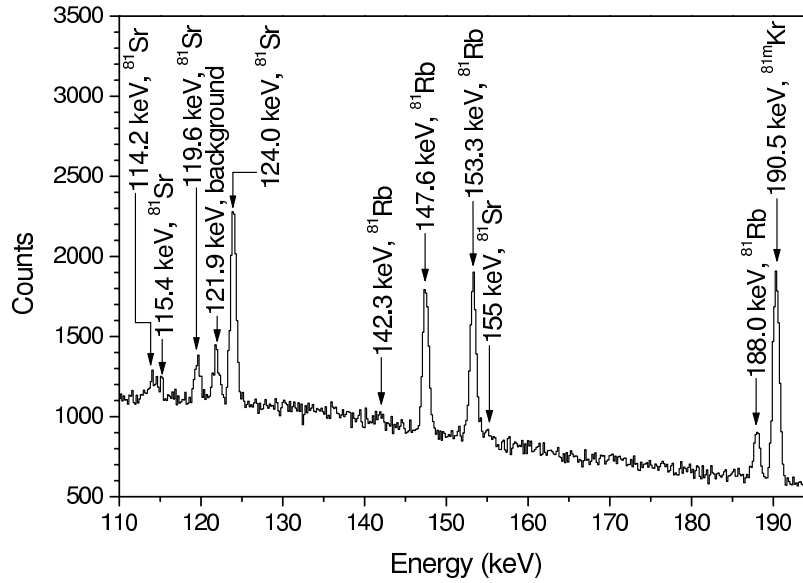


**Figure 4.20:** A low energy part of a  $\gamma$ -spectrum for  $A = 81$  measured by the LeGe detector. The peaks are labeled according to the transitions in daughter nuclei.

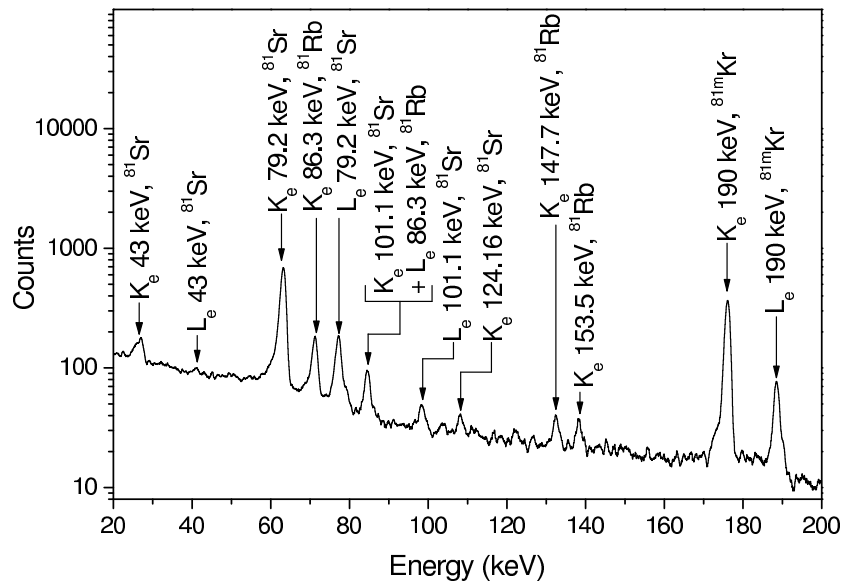


**Figure 4.21:** Internal conversion spectrum measured by the ELLI-spectrometer at  $A = 81$ .

conversion coefficient (ICC) for the 43.0 keV transition was  $\alpha_K = 1.5 \pm 0.3$  which supports an  $M1 + E2$  multipolarity for this transition.

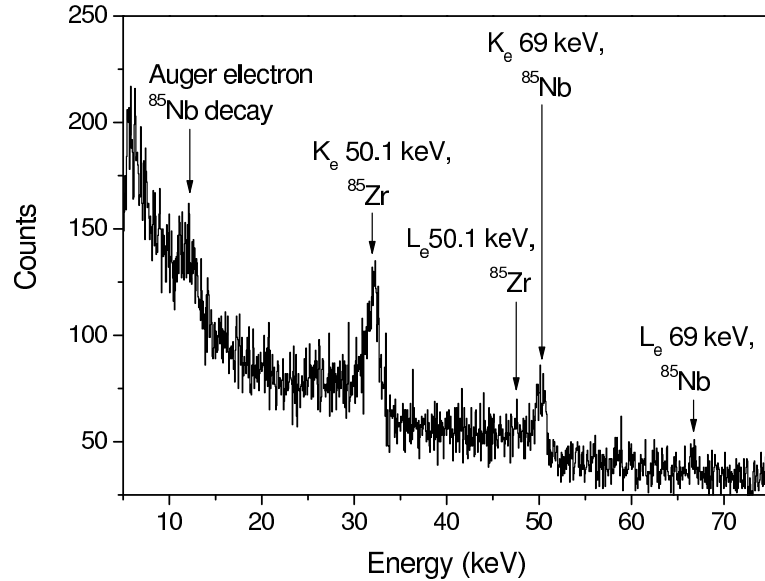


**Figure 4.22:** Internal conversion spectrum measured during the first 8 s of each measurement cycle at mass  $A = 85$ .

#### 4.4.2 $A=85$

The isotopes of interest at  $A = 85$  were produced via the reaction  $^{32}\text{S} + ^{nat}\text{Ni} \rightarrow ^{90}\text{Ru}^*$ . Nuclides with half-lives of seconds and minutes could be selected by using accumulation times of 15 s and 40 s at the first detector station. Indeed, peaks belonging to the decays of  $^{85}\text{Nb}$  (21 s),  $^{85}\text{Zr}$  (7.9 min) and  $^{85m}\text{Zr}$  (10.9 s) could be seen in  $\gamma$  and electron spectra.  $K$ -conversion electrons with an energy of 32.1 keV from a 50.1 keV transition in  $^{85}\text{Zr}$  were observed in the electron spectrum (see fig. 4.22). This 50 keV transition from the first excited state to the ground state is the only transition previously observed in the decay of  $^{85}\text{Nb}$  [Sie91]. The coincidence of this peak with Zr  $K$  X-rays supported the identification. In addition, the half-life based on this electron peak and the corresponding  $\gamma$  transition is  $17 \pm 2$  s which is a little less than the value  $20.9 \pm 0.7$  s attributed to  $^{85}\text{Nb}$  in [Kur88] (see fig. 4.23). ICCs for the observed transitions were determined for the first time (see table 4.7). The data suggest an  $M1 + E2$  mixture of multiplicities for the 50 keV transition.

An electron line with an energy of 50 keV in fig. 4.22 could not be attributed to any known transition at mass  $A = 85$ . The coincidence with the Nb  $K$  X-rays (see fig. 4.24) manifested that this electron line belongs to an unknown transition with an energy of 69 keV in  $^{85}\text{Nb}$ . The measured half-life of the transition was  $3.3 \pm 0.9$  s (see fig. 4.25). According to table 4.7 the preferable multipolarity for the transition is  $E2$  or  $M2$ , which cannot solely explain the half-life of the transition. However, the calculated Weisskopf estimates for the half-life ( $T_{1/2}(E2) = 1.6 \times 10^{-5}$  s,  $T_{1/2}(M2) = 1.0 \times 10^{-3}$  s,  $T_{1/2}(E3) = 380$  s and  $T_{1/2}(M3) = 2.4 \times 10^4$  s) suggest that the transition could be

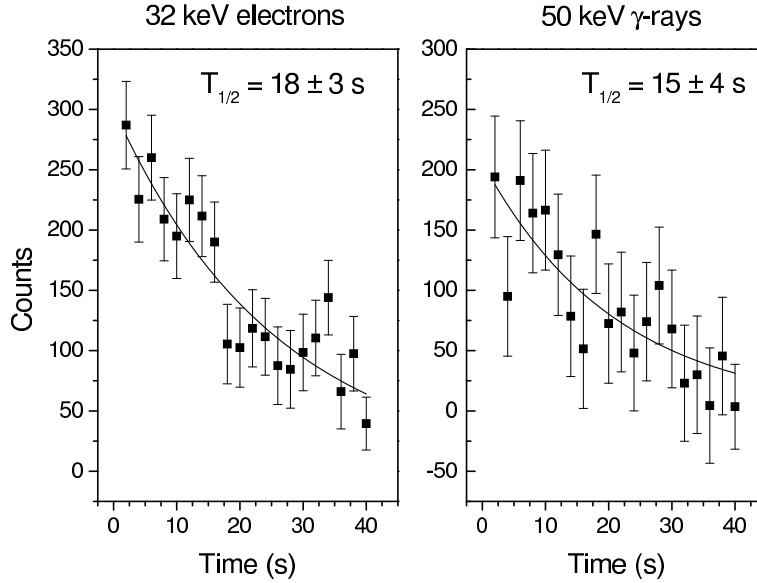


**Figure 4.23:** The time behavior of  $\gamma$ -rays and conversion electrons from the 50 keV transition in  $^{85}\text{Zr}$ . The average half-life of  $17 \pm 2$  s is little less than the value  $20.9 \pm 0.7$  s given in [Kur88].

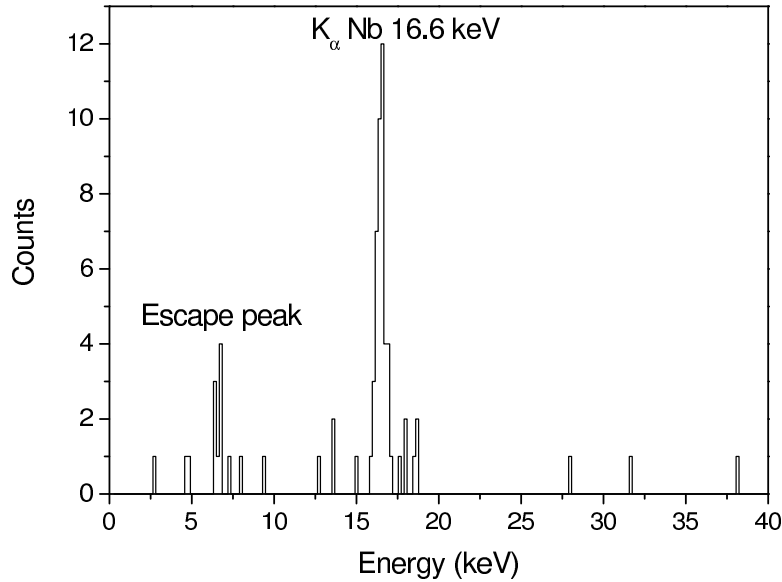


**Figure 4.24:** A low-energy part of the  $\gamma$ -spectrum in coincidence with the electrons of the 69 keV isomeric transition in  $^{85}\text{Nb}$ .

$M2$  with a significant mixture of  $E3$ . Another explanation for the observed half-life is that the isomeric state decays by a low-energy, highly-converted transition which feeds the 69 keV transition. A highly converted transition could not have been observed in coincidence with the electrons from the 69 keV transition.

The new 69 keV transition can originate either from the  $\beta^+$  decay of  $^{85}\text{Mo}$  or from a

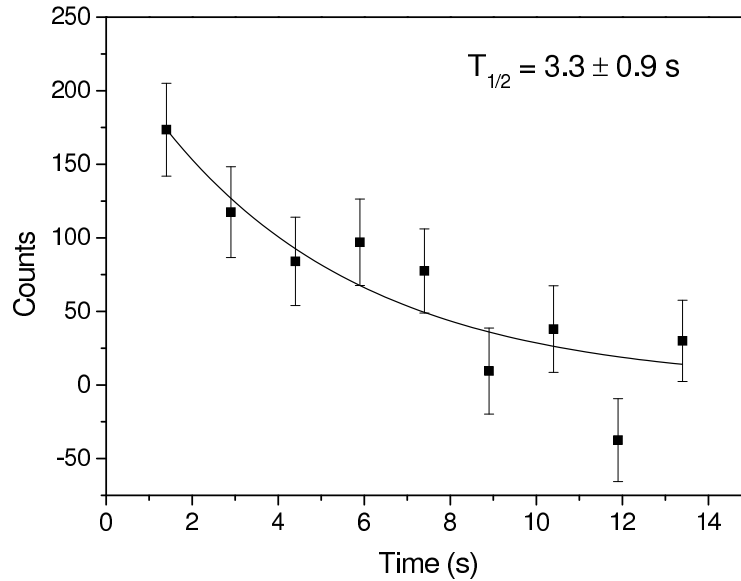


**Figure 4.25:** Background-corrected conversion electron intensities as a function of time for the 69 keV transition in  $^{85}\text{Nb}$ .

**Table 4.7:** ICCS and intensity ratios of K and L peaks ( $I_K/I_L$ ) for  $A = 85$  nuclei. The theoretical values are from [Ban02].

$\gamma$ -transition	$\alpha_K$ (exp.)	$\alpha_K$ (theor.)	$I_K/I_L$ (exp.)	$I_K/I_L$ (theor.)
$^{85}\text{Zr}$ , 50 keV	$1.7 \pm 0.2$	0.75 ( <i>E1</i> )	$9.0 \pm 1.8$	8.1 ( <i>E1</i> )
		1.3 ( <i>M1</i> )		8.1 ( <i>M1</i> )
		9.8 ( <i>E2</i> )		2.8 ( <i>E2</i> )
		23.7 ( <i>M2</i> )		5.2 ( <i>M2</i> )
$^{85}\text{Nb}$ , 69 keV	$> 2.6$	0.31 ( <i>E1</i> )	$4.1 \pm 1.3$	7.15 ( <i>E1</i> )
		0.57 ( <i>M1</i> )		7.0 ( <i>M1</i> )
		3.43 ( <i>E2</i> )		3.0 ( <i>E2</i> )
		7.83 ( <i>M2</i> )		3.86 ( <i>M2</i> )
		29.7 ( <i>E3</i> )		1 ( <i>E3</i> )
	83 ( <i>M3</i> )	2.54 ( <i>M3</i> )		

decay of a new isomeric state in  $^{85}\text{Nb}$ . No coincidence of this peak with the annihilation radiation was observed, which supports the latter option. In addition, the yield of this new transition is 0.8 transitions/s which is similar to the yield of  $^{85}\text{Nb}$  ground state (2 ions/s) shown in table 3.2. In addition, the yield ratio for  $^{85}\text{Mo}/^{85}\text{Nb}$  in the reaction  $^{32}\text{S} + ^{nat}\text{Ni}$  should be approximately the same as the yield ratio for  $^{81}\text{Zr}/^{81}\text{Y}$  in the reaction  $^{32}\text{S} + ^{54}\text{Fe}$ , which is less than 0.4 % (see table 3.2). This gives an upper limit of 0.01 ions/s for the expected yield of  $^{85}\text{Mo}$ , which disagrees strongly with the observed yield of the new transition and speaks in favor of the identification of  $^{85m}\text{Nb}$ . Figure 4.26 shows a proposed decay scheme of  $^{85}\text{Nb}$ .

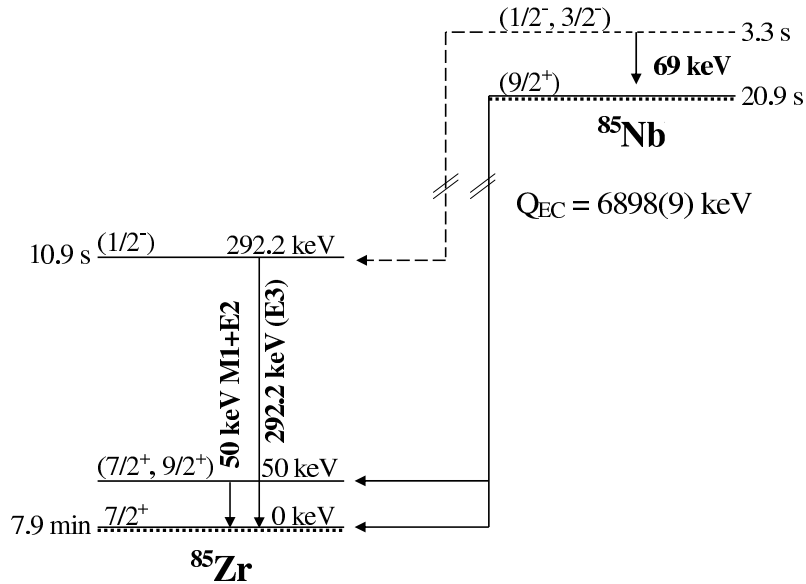


**Figure 4.26:** A proposed decay scheme of  $^{85}\text{Nb}$ . The  $Q$ -value is from the mass measurement performed at JYFLTRAP (see sec. 4.6). The suggested multipolarity  $E3$  is from [Sie91].

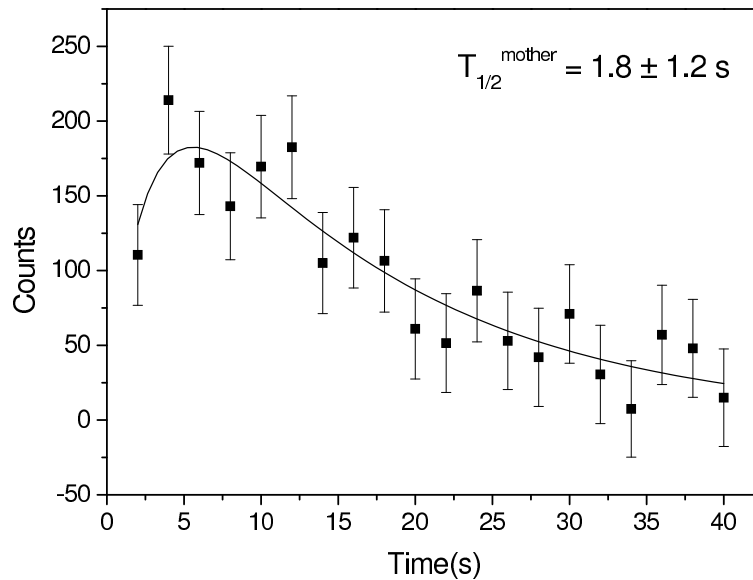


**Figure 4.27:** A fit of the time behavior of the 292 keV  $\gamma$ -transition of  $^{85m}\text{Zr}$  (normalized  $\chi^2 = 0.50$ ) assuming that the state is fed from a mother nucleus and the half-life of  $^{85m}\text{Zr}$  is fixed to 10.9 s [Sie91]. A half-life of  $1.8 \pm 1.2$  s obtained for the mother nuclide agrees with the half-life of  $^{85m}\text{Nb}$ . An exponential decay fit on the decay part yields a half-life of  $12 \pm 2$  s for  $^{85m}\text{Zr}$ .

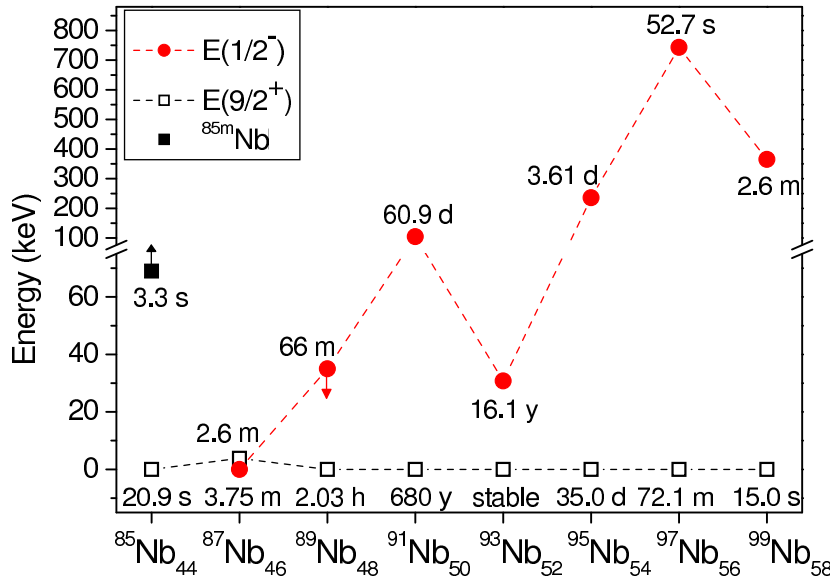


**Figure 4.28:** Isomeric states in odd-A Nb isotopes taken from refs. [Sie91], [Hel02], [Sin98], [Bag99], [Bag97], [Bur93], [Art93] and [Pek94] for  $A = 85$ – $99$ , respectively. The half-lives are marked next to the states. Spin and parity assignments are not certain for  $^{85}\text{Nb}$ ,  $^{87}\text{Nb}$  and  $^{89}\text{Nb}$ . The arrows show lower or upper limits for the states.

A  $\gamma$  transition with an energy of 292 keV belonging to a known isomeric state,  $^{85m}\text{Zr}$ , was also observed. Conversion electrons from this transition could not be detected since their energy was above the maximum energy of the ELLI detector. The measured half-life of  $12 \pm 2$  s was consistent with the average value of  $10.9 \pm 0.3$  s from [Sie91]. An indication of beta decay from  $^{85m}\text{Nb}$  to the 292 keV state of  $^{85m}\text{Zr}$  was seen in the time behavior of the 292 keV transition (see fig. 4.27). As the spin of the 292 keV state is tentatively  $1/2^-$  [Sie91], an allowed beta transition suggests spins of  $1/2^-$  or  $3/2^-$  for  $^{85m}\text{Nb}$  (see fig. 4.26).

An isomer in  $^{85}\text{Nb}$  was expected from the systematics of odd-A Nb isotopes between  $^{89}\text{Nb}$  and  $^{99}\text{Nb}$  all of which have a  $9/2^+$  ground state and a low-lying  $1/2^-$  isomeric state (see fig. 4.28). These states can be explained by an extreme single-particle shell model as having an odd proton in a  $1g_{9/2}$  or in a  $2p_{1/2}$  orbital. In NUBASE [Aud03a],  $^{85m}\text{Nb}$  is already stated to lie at 759 keV. This is based on the observation of 759 keV  $\gamma$  rays with a half-life of  $12 \pm 5$  s at mass  $A = 85$  [Oin98b]. However, those  $\gamma$  rays can also result from the  $\beta^+$  decay of  $^{85}\text{Mo}$  as was discussed in [Oin98b]. The 759 keV  $\gamma$  peak was also detected in this experiment with the  $\gamma - \gamma$  setup as well as the  $\gamma$ -rays at 272 keV, 484 keV, 532 keV, 538 keV, 590 keV, 660 keV and 709 keV observed at  $A = 85$  already in [Oin98b]. Unfortunately, none of these  $\gamma$  transitions could be identified to belong to the isomeric transition. Further studies on the isomeric state in  $^{85}\text{Nb}$  were carried out in the mass experiment at JYFLTRAP but the isomer could not be observed within about 900 keV from the ground state (see sec. 4.6). Nevertheless,

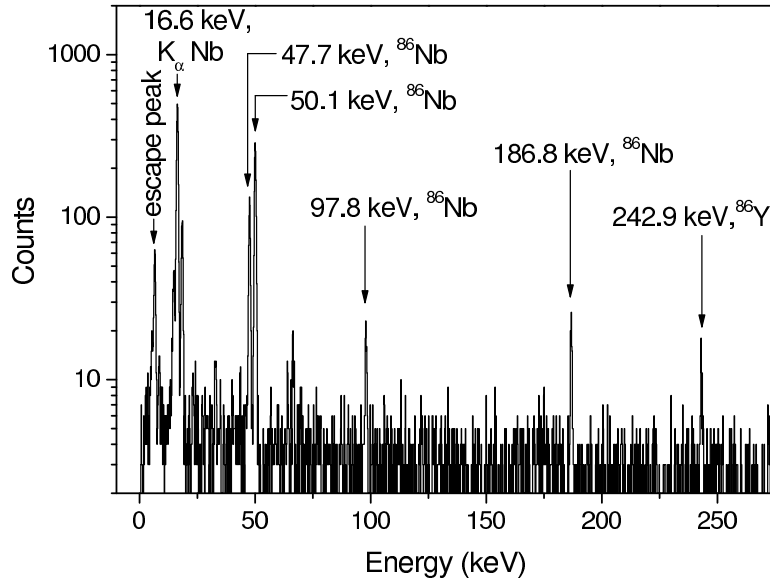


**Figure 4.29:** A  $\gamma$ -ray spectrum measured by the LeGe-detector gated by electrons at mass  $A = 86$ . The peaks are labeled according to the transitions in daughter nuclei.

the observation of a new isomer with a half-life of 3.3 s in  $^{85}\text{Nb}$  should be taken into account in the rp-process network calculations.

#### 4.4.3 $A=86$

The isotopes of interest at  $A = 86$  were produced via the reaction  $^{32}\text{S} + ^{\text{nat}}\text{Ni} \rightarrow ^{90}\text{Ru}^*$ . In order to observe both  $^{86}\text{Mo}$  and  $^{86}\text{Nb}$ , accumulation times of 40 s and 200 s were used at the first detector station. Gamma lines with energies of 47.7 keV and 50.1 keV as well as Nb and Zr  $K$  X-rays were seen in the  $\gamma$  spectrum gated by electrons (see fig. 4.29). These gamma peaks belong to a cascade de-excitation of the  $E_0+97.1$  keV level in  $^{86}\text{Nb}$  [Sin01] which is fed by the beta decay of  $^{86}\text{Mo}$  [Shi94]. The cascade nature was supported by strong coincidences between the electrons from one of the 47.7 keV and 50.1 keV transitions and the  $\gamma$  line of the other transition (see fig. 4.30). A new peak with an energy of 97.8 keV was also observed in fig. 4.29. This transition had no coincidence with the cascade peaks and could be considered as a crossover transition from the level with an energy of  $E_0+97.8$  keV in  $^{86}\text{Nb}$ . The observed 186.8 keV transition (see fig. 4.29) populates the level at  $E_0+50.1$  keV because it was in coincidence only with the electron line belonging to the 50.1 keV transition.

The proposed beta-decay scheme of  $^{86}\text{Mo}$  is shown in fig. 4.31. ICCs listed in table 4.8 support an  $M1$  character for the 47.7 keV transition and  $E1$  for the 50.1 keV transition. The multipolarities for the 97.8 keV and 186.8 keV transitions are most likely  $E1$ . The spin identification of the isomeric state at  $E_0$  is different from [Shi94], where  $M1$

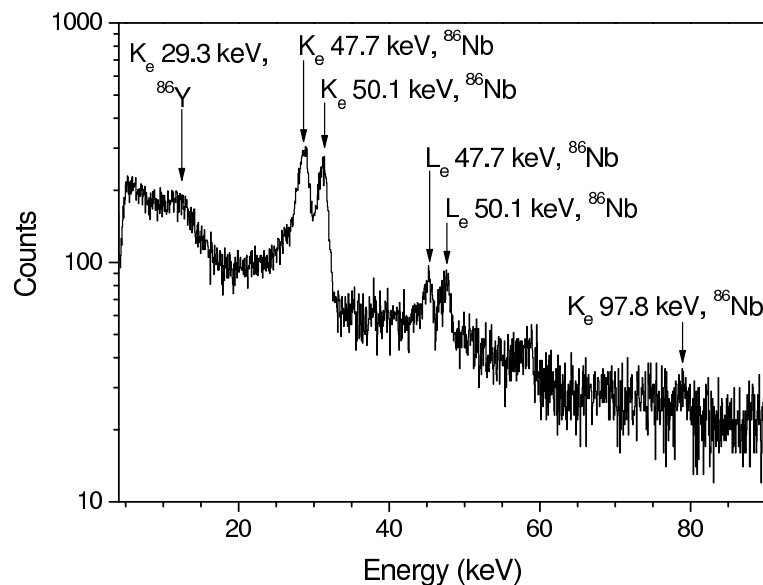


**Figure 4.30:** A part of the internal conversion electron spectrum measured by the ELLI-spectrometer at mass  $A = 86$ .

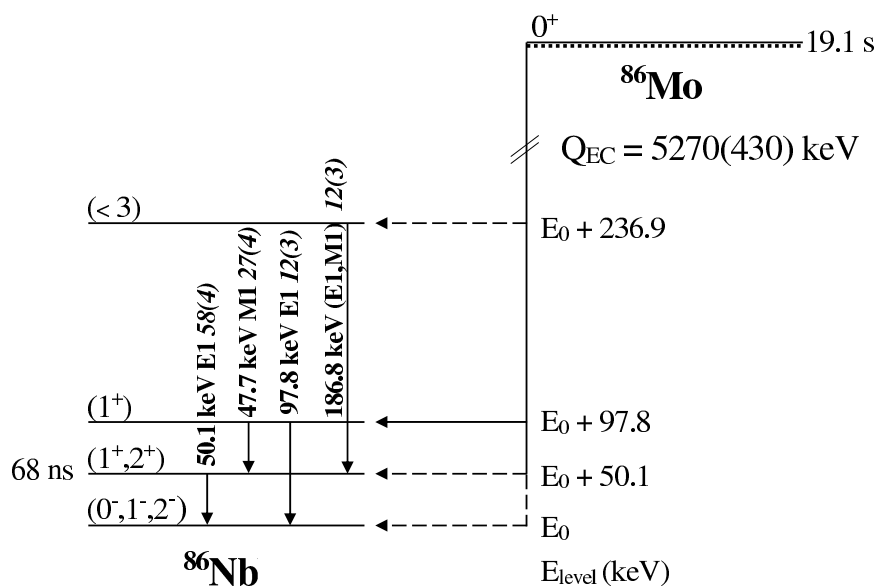


**Figure 4.31:** A proposed decay scheme of  $^{86}\text{Mo}$ . The  $\gamma$ -ray intensities are normalized by the 50.1 keV transition. The  $Q$ -value is taken from [Aud03b].

**Table 4.8:** ICCs and intensity ratios of K, L and M peaks ( $I_K/I_{L+M}$ ) for  $^{86}\text{Nb}$ . The theoretical values are from [Ban02].

$E_\gamma$ (keV)	$\alpha_K$ (exp.)	$\alpha_K$ (theor.)	$I_K/I_{L+M}$ (exp.)	$I_K/I_{L+M}$ (theor.)
47.7	$1.8 \pm 0.3$	0.89( <i>E1</i> )	$8.3 \pm 0.7$	8.3( <i>E1</i> )
		1.64( <i>M1</i> )		8.4( <i>M1</i> )
		11.4( <i>E2</i> )		2.6( <i>E2</i> )
		31.6( <i>M2</i> )		5.1( <i>M2</i> )
50.1	$0.65 \pm 0.10$	0.77( <i>E1</i> )	$6.5 \pm 0.6$	8.3( <i>E1</i> )
		1.4( <i>M1</i> )		8.4( <i>M1</i> )
		9.8( <i>E2</i> )		2.8( <i>E2</i> )
		26.2( <i>M2</i> )		5.2( <i>M2</i> )
97.8	$0.09 \pm 0.04$	0.11( <i>E1</i> )	-	-
		0.21( <i>M1</i> )		
186.8	$< 0.04$	0.017( <i>E1</i> )	-	-
		0.0036( <i>M1</i> )		

multipolarity was given for the 50 keV transition instead of *E1* and the multipolarity of the 187 keV transition was not determined. This also changes the de-excitation scheme in  $^{86}\text{Nb}$ . The new spin assignment implies that the beta decay to the  $E_0$  level should be weak. For the levels at  $E_0+50.1$  keV,  $E_0+97.8$  keV and  $E_0+236.9$  keV  $\log ft$  values between 4.5 and 5.0 were estimated assuming  $Q_{EC} = 5270 \pm 430$  keV [Aud03b] for the  $E_0$  level and negligible beta decay branchings to other levels. A spin less than 3 is expected from the  $\log ft$  estimate for the state at  $E_0+236.9$  keV.

No converted transitions from the state with an unknown energy  $E_0$  in  $^{86}\text{Nb}$  were observed in this work. Therefore, this state is either highly excited and decays by a high-energy transition or the main channel of de-excitation is the direct  $\beta^+$  decay to the states in  $^{86}\text{Zr}$ . Thus, the position of the level  $E_0$  remains still unknown.

The half-lives and isomeric level structures of  $^{86}\text{Mo}$  and  $^{86}\text{Nb}$  are of potential astrophysical relevance as during freezeout they can impact the final distribution of isotopic abundances in the  $A = 86$  mass region produced by the rp-process. In this thesis, the half-life of  $^{86}\text{Mo}$  was determined from the time behavior of  $\gamma$ , Nb *K* X-ray and electron peaks. The weighted average value of  $19.1 \pm 0.3$  s confirms the half-life of  $19.6 \pm 1.1$  s obtained in [Shi94]. However, no indication of the existence of an isomer in  $^{86}\text{Nb}$  with a half-life of 56 s [Shi94] was found. The existence of this isomer has already been considered as uncertain due to a possible mixed activity of the 88 s, ( $6^+$ ) isomer and a low-spin isomer of unknown half-life populated in  $^{86}\text{Mo}$  EC decay [Sin01]. This isomer was also searched in a mass experiment at JYFLTRAP but no isomer could be found within 450 keV from the ground state (see sec. 4.6).

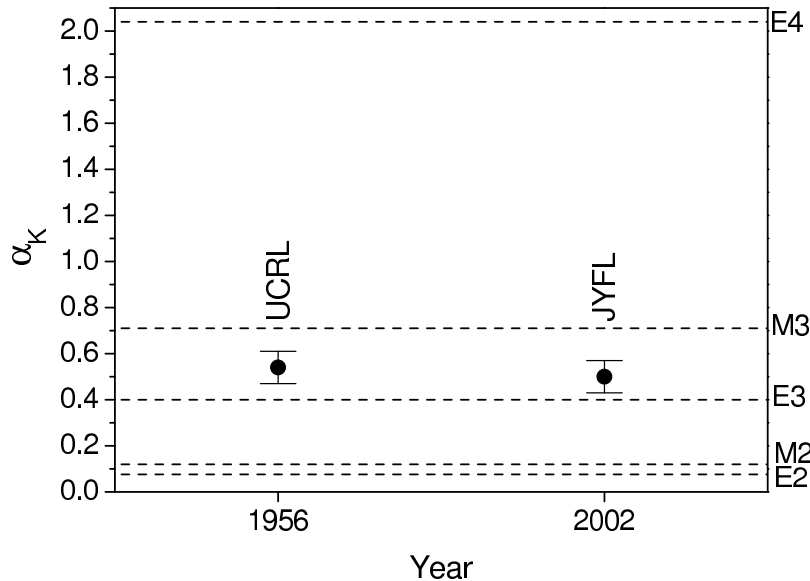


**Figure 4.32:** The ICC of the 190.5 keV isomeric transition in  $^{81}\text{Kr}$  measured in this work in comparison with the value from [Dog56]. The dashed lines show the theoretical values [Ban02].

## 4.5 The decay of $^{81m}\text{Kr}$ and $^{81}\text{Br}$ solar neutrino detector

As described in sec. 2.3.3, neutrino capture on  $^{81}\text{Br}$  should mainly populate the isomeric state at 190.5 keV in  $^{81}\text{Kr}$ . Therefore, the rates for all decay branches of  $^{81m}\text{Kr}$  are important for the calculation of the electron-capture probability. This electron-capture branching ratio has not been obtained with high accuracy as the data on the isomeric transition are controversial.

In the experiment on the isomers of astrophysical interest (see sec. 4.4.1) strong lines belonging to the 190.5 keV isomeric transition in  $^{81}\text{Kr}$  were observed in  $\gamma$  and electron spectra (see figs. 4.20 and 4.21). The measured  $\alpha_K$ -value agrees with the only existing experimental value [Dog56] shown in fig. 4.32. The experimental values of the ratio  $\alpha_K/\alpha_{L+M}$  [Han69, Väi75, Lip77, Toy79] have been controversial before this experiment, as can be seen in fig. 4.33. For the multipolarity determination, the latest ICC tables were used [Ban02]. The obtained coefficients,  $\alpha_K = 0.50 \pm 0.07$  and  $\alpha_K/\alpha_{L+M} = 4.7 \pm 0.1$ , favor an  $E3$  character for this transition. To identify the  $^{81m}\text{Kr}$  peak, its half-life was determined for  $\gamma$ - and  $e^-$ -decay channels (fig. 4.34). The average half-life of  $13.4 \pm 0.7$  s agrees well with the earlier value of  $13.10 \pm 0.03$  s [Bag96].

The measured ICCs are needed to calculate the electron-capture branching ratio  $\eta_e$  of the isomeric state  $^{81m}\text{Kr}$ . This branching ratio is important for the rate of the inverse

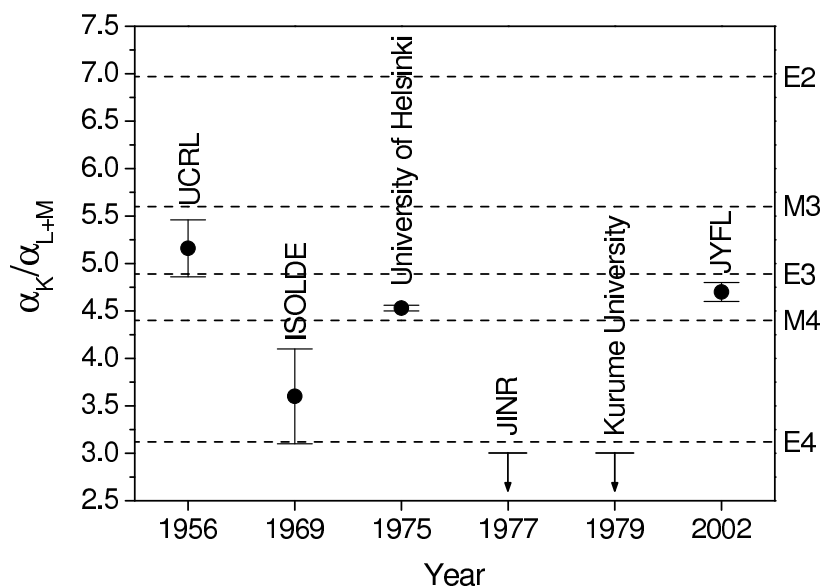


**Figure 4.33:** The values of  $\alpha_K/\alpha_{L+M}$  for the 190.5 keV isomeric transition in  $^{81}\text{Kr}$  from literature [Bag96] and the one measured in this work. The dashed lines show the theoretical values [Ban02].

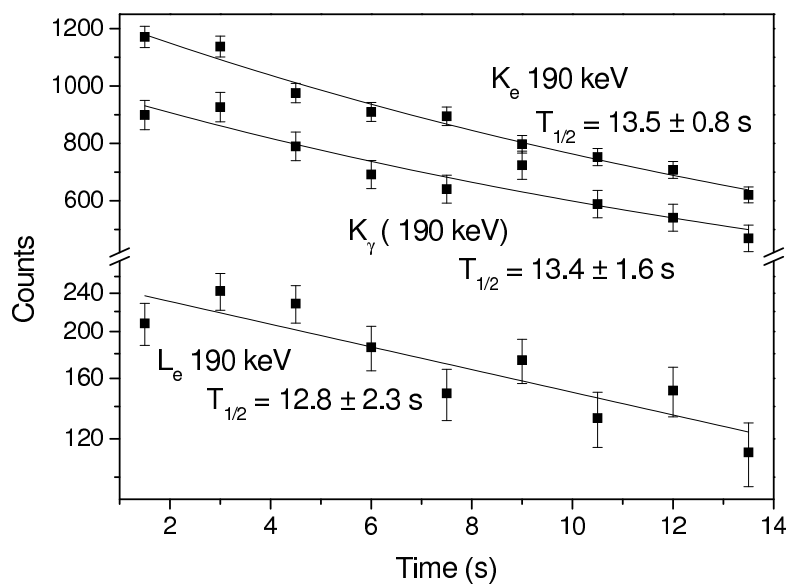


**Figure 4.34:** Time dependent areas for different peaks of the isomeric transition of  $^{81m}\text{Kr}$ . The determined half-lives are indicated near the corresponding lines.

**Table 4.9:** Neutrino capture probability for the  $^{81}\text{Br} \rightarrow ^{81m}\text{Kr}$  transition.

Group	Argonne [Dav87]	Princeton [Low87]	This work
$\eta_\varepsilon (\times 10^{-5})$	$3.14 \pm 0.58$	$2.26 \pm 0.32$	-
Average $\eta_\varepsilon (\times 10^{-5})$		$2.47 \pm 0.37$	$3.0 \pm 0.5$
$\alpha_K$	0.4	0.4	$0.50 \pm 0.07$
$\alpha_{tot}$	0.48	0.49	$0.61 \pm 0.09$
$\log ft (\nu \text{ capture})$		$5.19 \pm 0.07$	$5.13 \pm 0.09$

process of neutrino capture on  $^{81}\text{Br}$  (see fig. 2.10) and it can be deduced from the relation:

$$\begin{aligned} \eta_\varepsilon &= \frac{\lambda_\varepsilon}{\lambda_e + \lambda_\gamma + \lambda_\varepsilon} \\ &= \frac{\lambda_{\varepsilon_K} \left(1 + \frac{\lambda_{(\varepsilon_L + \varepsilon_M)}}{\lambda_{\varepsilon_K}}\right)}{\lambda_{\varepsilon_K} \left(1 + \frac{\lambda_{(e_L + e_M)}}{\lambda_{\varepsilon_K}}\right) \left(1 + \frac{\lambda_\gamma}{\lambda_e}\right) + \lambda_{\varepsilon_K} \left(1 + \frac{\lambda_{(\varepsilon_L + \varepsilon_M)}}{\lambda_{\varepsilon_K}}\right)} \end{aligned} \quad (4.2)$$

where  $\lambda_e$ ,  $\lambda_\gamma$  and  $\lambda_\varepsilon$  stand for internal conversion, gamma transition and electron-capture probabilities. Indices  $K$ ,  $L$  and  $M$  label the corresponding atomic shells.

If  $\eta_\varepsilon \ll 1$ , as it is expected for the decay of  $^{81m}\text{Kr}$ , the following expression can be deduced:

$$\eta_\varepsilon = \left(1 + \frac{\lambda_{(\varepsilon_L + \varepsilon_M)}}{\lambda_{\varepsilon_K}}\right) \times \frac{K_X(\text{Br})\omega_K(\text{Kr})}{K_X(\text{Kr})\omega_K(\text{Br})} \times \frac{\alpha_K}{(1 + \alpha_{tot})} \quad (4.3)$$

where  $K_X$  is the intensity of characteristic X-rays corresponding to the  $K$ -shell,  $\omega_K$  stands for the respective  $K$ -fluorescence yield and  $\alpha$  represents the ICC. As a summary, the electron-capture branching ratio depends on the ratio of electron-capture branches  $\lambda_{(\varepsilon_L + \varepsilon_M)}/\lambda_{\varepsilon_K}$ , on the intensity ratio of Br  $K$  X-rays to Kr  $K$  X-rays and on the ratio  $\alpha_K/(1 + \alpha_{tot})$

The ratio of electron-capture branches was calculated in this work with the values from [Dzh72]. The overlapping and exchange effects [Fae70] were taken into account, which lead to  $\lambda_{(\varepsilon_L + \varepsilon_M)}/\lambda_{\varepsilon_K} = 0.144$ . Groups at Princeton [Low87] and Argonne [Dav87] have measured the ratio for  $K$  X-rays and determined the electron-capture branching ratio. However, they used theoretical values for electron-capture branches ( $\lambda_{(\varepsilon_L + \varepsilon_M)}/\lambda_{\varepsilon_K} = 0.119$ ) and for ICCs ( $\alpha_K = 0.4$  and  $\alpha_{tot} = 0.48$ ) in the calculation.

In the present work the ICCs were measured and the ratio  $\alpha_K/(1 + \alpha_{tot})$  was determined. The neutrino capture rate of the  $3/2^- \rightarrow 1/2^-$  transition in the  $^{81}\text{Br}$  detector was then calculated with the intensity ratio of  $K$  X-rays [Low87, Dav87] and with the revised value for the ratio of electron-capture branches. The corresponding  $\log ft$  computed with the tabulated  $f$ -values from [Dzh72] is given in table 4.9 in comparison with the averaged value taken from [Bag96]. The obtained  $\log ft$  value is slightly lower than the earlier value leading to an increased neutrino capture cross section. Therefore,  $^{81}\text{Br}$  is suitable for a solar neutrino flux detector as was suggested in refs. [Dav87, Low87].

## 4.6 Masses of neutron-deficient nuclides near $A = 80$

Masses of 13 neutron-deficient nuclei in the  $A = 80$  region were measured using the JYFLTRAP setup at IGISOL (see sec. 3.2.6). The masses of these nuclei are important for the astrophysical rp process (see sec. 2.3.1 and fig. 2.7). The measured masses are presented in sec. 4.6.1. After that, the role of isomeric states in the measured nuclei is discussed. The results from the spectroscopy experiment on isomers in this mass region have already been given in sec. 4.4. The results for Y, Zr and Nb isotopes are reported nuclide by nuclide and compared to earlier experiments and the values of the 2003 Atomic Mass Evaluation (AME) [Aud03b].

### 4.6.1 Measured masses

The masses of  $^{80-83}\text{Y}$ ,  $^{83-86,88}\text{Zr}$  and  $^{85-88}\text{Nb}$  were measured during this experiment (see table 4.10). All measurements were done with 900 ms excitation time in the precision trap. The stable isotopes  $^{96-98}\text{Mo}$  were used as reference masses. In order to test the reliability of the system,  $^{96}\text{Mo}$  and  $^{98}\text{Mo}$  were measured relative to  $^{97}\text{Mo}$ . As shown in table 4.10, the reference masses agree nicely with the tabulated value of [Aud03b]. Except for the stable Mo references, all nuclei were measured as oxides formed with  $^{16}\text{O}$  in the HIGISOL. Figure 4.35 shows an example of time-of-flight resonance spectrum measured for  $^{84}\text{Zr}$  in this work.

Apart from the uncertainty of the reference masses, 1.9 keV for  $^{96,97,98}\text{Mo}$ , and in the case of oxides that of  $^{16}\text{O}$  (0.0001 keV), three systematic uncertainties were taken into account in the analysis. Firstly, in an offline study comparing  $^{129}\text{Xe}$  to  $^{16}\text{O}_2$  the resonance frequency was found not to be perfectly linear in mass, but to have a slight offset of  $7 \times 10^{-10}$  per mass unit difference between the compared masses. This shift was taken into account by quadratically adding it to the uncertainty of the final average for each studied nucleus. Secondly, large numbers of ions in the trap

**Table 4.10:** The measured mass excesses (ME) compared to the tabulated values [Aud03b]. The number of measurements (N) and the reference nuclide are indicated for each nuclide. All masses are for the ground states (see sec. 4.6.2).

Nuclide	Reference	N	ME(JYFL) (keV)	ME(AME) (keV)	AME-JYFL (keV)
$^{80}\text{Y}$	$^{96}\text{Mo}$	3	-61144(7)	-61220(180)	-76
$^{81}\text{Y}$	$^{97}\text{Mo}$	3	-65709(6)	-66020(60)	-311
$^{82}\text{Y}$	$^{98}\text{Mo}$	7	-68060(6)	-68190(100)	-130
$^{83}\text{Y}^\dagger$	$^{98}\text{Mo}$	3	-72170(6)	-72330(40)	-160
$^{83}\text{Zr}$	$^{98}\text{Mo}$	2	-65908(7)	-66460(100)	-552
$^{84}\text{Zr}$	$^{98}\text{Mo}$	4	-71418(6)	-71490(200)	-72
$^{85}\text{Zr}$	$^{98}\text{Mo}$	3	-73170(6)	-73150(100)	20
$^{86}\text{Zr}$	$^{98}\text{Mo}$	3	-77958(7)	-77800(30)	158
$^{88}\text{Zr}$	$^{98}\text{Mo}$	3	-83624(7)	-83623(10)	1
$^{85}\text{Nb}^\dagger$	$^{98}\text{Mo}$	3	-66273(7)	-67150(220)	-877
$^{86}\text{Nb}$	$^{98}\text{Mo}$	5	-69129(6)	-69830(90)	-701
$^{87}\text{Nb}^\dagger$	$^{98}\text{Mo}$	2	-73868(7)	-74180(60)	-312
$^{88}\text{Nb}^\dagger$	$^{98}\text{Mo}$	3	-76149(7)	-76070(100)	79
$^{96}\text{Mo}$	$^{97}\text{Mo}$	3	-88789(6)	-88790.5(1.9)	-1.5
$^{98}\text{Mo}$	$^{97}\text{Mo}$	3	-88111(6)	-88111.7(1.9)	-1.0

$^\dagger$  The possible contributions from  $^{83m}\text{Y}$  at 61.98(11) keV,  $^{85m}\text{Nb}$  at  $\geq 69$  keV,  $^{87m}\text{Nb}$  at 3.84(14) keV and  $^{88m}\text{Nb}$  at 40(140) keV have not been taken into account. For a possible treatment of mixtures of isomeric and ground states, see ref. [Wap03] p. 174-180.

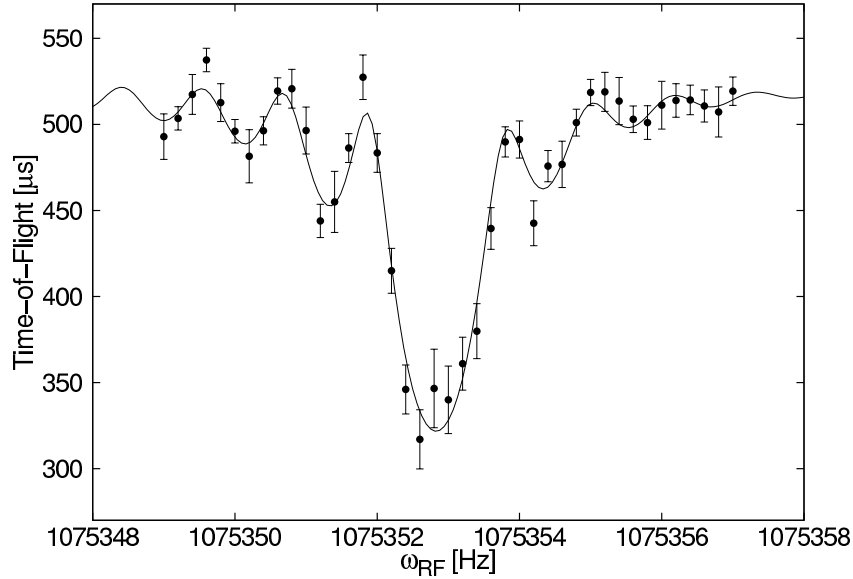


**Figure 4.35:** Time-of-flight resonance of  $^{84}\text{Zr}$  with an excitation time of 900 ms. The fit of the experimental data points is shown by a solid line.

can cause the frequency to shift. To estimate the resulting uncertainty, an analysis of the frequency depending on the countrate was done for all measurements of  $^{98}\text{Mo}$ . In the final analysis the maximum number of ions in the trap was therefore limited to three, and an uncertainty of 0.04 Hz was quadratically added to the uncertainty of the final average for each nucleus, corresponding to about 3 keV in this mass range. Thirdly, to compensate for fluctuations of the magnetic field and of the electronics, the fluctuation of the measured frequency of  $^{98}\text{Mo}$  from one measurement to the next was examined. The average discrepancy was found to be of the order of 0.04 Hz. Since the fluctuation is assumed to be completely random, this value was quadratically added to the statistical uncertainty of each measured frequency.

## 4.6.2 Isomers

Several of the measured nuclei have isomeric states (see table 4.11). The observation of these isomers is experimentally limited by the half-life, the excitation energy and by their relative production rate. With the typical production rates in this experiment, isomers with a half-life of less than 500 ms could not be measured due to the excitation time of 900 ms in the precision trap and a total cycle time of  $\sim 1.5$  s. The FWHM of the time-of-flight resonance was about 1.2 Hz, or about 100 keV in this mass region. Thus, isomers with low excitation energies could not be resolved.

Due to half-life and excitation energy limitations, only the isomeric states of  $^{80}\text{Y}$ ,  $^{85}\text{Zr}$ ,  $^{85}\text{Nb}$ , and possibly  $^{86}\text{Nb}$  and  $^{88}\text{Nb}$ , are interesting for further studies. Larger frequency

**Table 4.11:** Isomeric states as listed in the NUBASE compilation [Aud03a]. Given are the excitation energies, the half-lives and the spins and parities ( $J^\pi$ ) for the isomeric and ground states.

Isomer	$E_x$ (keV)	$T_{1/2}$	$J^\pi$	$J^\pi_{g.s.}$
$^{80m1}\text{Y}$	228.5(1)	4.8 s	$1^-$	$4^-$
$^{80m2}\text{Y}$	312.5(10)	4.7 $\mu\text{s}$	$(2^+)$	$4^-$
$^{82m}\text{Y}$	402.63(14)	268 ns	$4^-$	$1^+$
$^{83m}\text{Y}$	61.98(11)	2.85 min	$3/2^-$	$9/2^+$
$^{83m}\text{Zr}$	52.72(5)	530 ns	$(5/2^-)$	$(1/2^-)$
$^{85m}\text{Zr}$	292.2(3)	10.9 s	$(1/2^-)$	$7/2^+$
$^{85m}\text{Nb}^\dagger$	$\geq 69$	3.3 s	$(1/2^-)$	$(9/2^+)$
$^{86m}\text{Nb}$	250#(160#)	56 s	-	$(6^+)$
$^{87m}\text{Nb}$	3.84(14)	2.6 min	$(9/2^+)$	$(1/2^-)$
$^{88m}\text{Nb}$	40(140)	7.8 min	$(4^-)$	$(8^+)$

<sup>†</sup> The energy and halflife of  $^{85m}\text{Nb}$  are from this work. The appearance of a 759.0(10) keV isomer with  $T_{1/2}=12$  s in ref. [Aud03a] is based on a misinterpretation of the result of ref. [Oin98b] where a  $\beta$ -coincident  $\gamma$  ray with an energy of 759 keV was reported.

ranges were scanned to find a second resonance. For  $^{80m1}\text{Y}$ ,  $^{85m}\text{Zr}$  and  $^{85m}\text{Nb}$  the excitation energies are known according to [Aud03a], but no second resonance could be found at the corresponding distance from the measured resonance frequency. For  $^{86}\text{Nb}$ , no second resonance was observed within about 450 keV and for  $^{88}\text{Nb}$  the limit was about 310 keV.

Since in all of these cases only one state was observed, it is not possible to determine whether the measured nucleus was the ground state or the excited state. In the case of  $^{85}\text{Nb}$ , the measured mass would agree better with the tabulated value of the excited state than with the ground state (see [Aud03a]). This is also the case for the other Nb isotopes. For Zr and Y isotopes, however, the measured mass is closer to the ground state. On the other hand, the isomers  $^{80m1}\text{Y}$ ,  $^{85m}\text{Zr}$  and  $^{85m}\text{Nb}$  are less produced than the ground state at HIGISOL. As only primary ions are mass-separated at IGISOL, the observed yields represent the isomeric and ground states as well. The isomeric to ground state ratios at HIGISOL are about 1:4 for  $^{80}\text{Y}$  [Nov01, Hui04], 1:40 for  $^{85}\text{Zr}$  and 1:2 for  $^{85}\text{Nb}$  (see table 3.2).

### 4.6.3 Y isotopes

The results of the Y isotopes are presented in fig. 4.36 in comparison with the earlier results and the AME values. Most of the masses are based on measurements of the

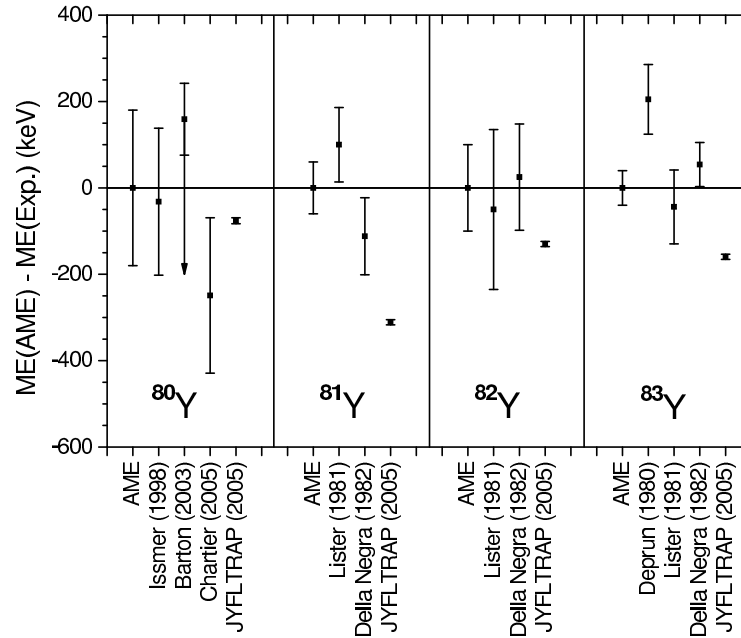


**Figure 4.36:** Mass excesses of the measured Y isotopes relative to AME values [Aud03b]. The labels refer to beta-decay experiments of Barton *et al.* [Bar03], Lister *et al.* [Lis81], Della Negra *et al.* [Del82a], Deprun *et al.* [Dep80] and to the TOF experiments at SARA by Issmer *et al.* [Iss98] and at CSS2 by Chartier *et al.* [Cha05]. The  $Q_{EC}$  value of  $^{80}\text{Y}$  in [Bar03] is only a lower limit which is indicated by an arrow in the figure.

end-point energies of  $\beta^+$  spectra. The corresponding mass excesses have been calculated from the  $Q_{EC}$  values with the tabulated mass excesses of the daughter nuclei  $^{80,81,82,83}\text{Sr}$  [Aud03b]. The measured mass excesses agree with the AME values reasonably. The best agreement is observed with  $^{80}\text{Y}$  for which a direct time-of-flight measurement has been performed.

### $^{80}\text{Y}$

The mass of  $^{80}\text{Y}$  is important for rp-process calculations as it is the beta-decay daughter of the waiting-point nucleus  $^{80}\text{Zr}$ . The uncertainties in nuclear masses close to the  $N = Z$  waiting points lead to large uncertainties in the rp-process calculations of the reaction and decay rates in this mass region. In addition, this region close to  $A = 80$  shows rapid changes in nuclear shape and structure which makes the extrapolation of nuclear masses of unknown nuclei uncertain.

Partly due to astrophysical motivation, the mass of  $^{80}\text{Y}$  has been measured several times. The early beta-decay experiments yielded  $Q_{EC}$  values of 6952(152) keV [Lis81], 6934(242) keV [Del82a] and 6200(600) keV [Shi96]. Although these values were consistent, the calculated mass excesses were more than 2 MeV too low compared to the

AME value based on the systematics of neighboring isotopic and isotonic chains. A direct mass measurement of  $^{80}\text{Y}$  using the second cyclotron of SARA of the ISN as a time-of-flight spectrometer gave a  $Q_{EC}$  value of 9120(170) keV [Iss98] which proved that the earlier  $Q_{EC}$  values were too low. Due to this discrepancy, the results from [Del82a, Lis81, Shi96] have been left out from fig. 4.36. The  $Q_{EC}$  value has also been recently measured via beta-gamma coincidence spectroscopy and a lower limit for the  $Q_{EC}$  value was measured to be 8929(83) keV [Bar03] which corresponds a mass excess bigger than  $-61379(84)$  keV. The large disagreement with the earlier  $\beta^+$  end-point measurements is suggested to arise from the assumptions about  $\beta^+$  feeding in the  $^{80}\text{Y}$  decay scheme. The  $\beta^+$  spectrum was earlier measured in coincidence with the two lowest-lying  $\gamma$  transitions from the levels at 386 keV and 981 keV [Del82a, Lis81] but in [Bar03], the gating  $\gamma$  transition was from the highest fed level observed at 3284 keV. Thus, the  $\beta^+$  decay of  $^{80}\text{Y}$  should primarily feed a level or a set of levels above  $\approx 3$  MeV and not the low-lying levels.

There have also been two time-of-flight measurements using the second cyclotron of GANIL, CSS2, as a mass spectrometer of high resolution [Lal01, Cha05]. Due to a number of experimental difficulties in [Lal01], the measured mass excess of  $-62097(80)$  keV, differs from the other existing experiments and is not included in fig. 4.36. The mass was remeasured at CSS2 resulting a new mass excess of  $-60971(180)$  keV [Cha05] which agrees well with the values of  $-61188(171)$  keV [Iss98], the adopted AME value of  $-61220(180)$  keV and  $-61144(7)$  keV from this work. The mass measured in this work corresponds to the ground state as the well-known isomer at 228.5 keV in  $^{80}\text{Y}$  is much less produced than the ground state and no second resonance was found in a wider frequency range (see sec. 4.6.2). The other isomeric state at 312.5 keV in  $^{80}\text{Y}$  ( $4.7 \mu\text{s}$ ) was too short-lived for JYFLTRAP.

## $^{81}\text{Y}$

The measured mass excess of  $-65709(6)$  keV does not agree with the AME value which is based on beta-decay experiments of [Del82a] and [Lis81]. In [Lis81], a  $Q_{EC}$  value of 5408(86) keV was determined from coincidences with 124 keV and 408 keV  $\gamma$  rays in  $^{81}\text{Sr}$  and the deduced mass excess is  $-66120(87)$  keV. In [Del82a], the mass and the 124 keV  $\gamma$  transition measured with a plastic scintillator were used to gate the  $\beta^+$  spectrum, which resulted in a  $Q_{EC}$  value of 5620(89) keV and a mass excess of  $-65908(90)$  keV. Although the adopted  $Q_{EC}$  value of [Del82a] disagrees with the value from this work, the  $Q_{EC}$  value with the 124 keV  $\gamma$ -ray gate in a Ge detector ( $Q_{EC}=5704(128)$  keV [Del82a]) yields a mass excess of  $-65824(129)$  keV in agreement with the mass excess measured in this work. As a summary, the differences in the mass excesses can be explained by the uncertainties in the determination of  $\beta^+$  end-point energies.

$^{82}\text{Y}$ 

The isomer at 402.63 keV (268 ns) in  $^{82}\text{Y}$  was too short-lived for JYFLTRAP and was not observed. The measured mass excess for the ground state,  $-68060(6)$  keV, disagrees slightly with the AME value,  $-68190(100)$  keV. In [Lis81], a 574 keV  $\gamma$  transition in  $^{82}\text{Sr}$  was used to gate the  $\beta^+$  spectrum and the measured  $Q_{EC}$  value was 7868(185) keV. The calculated mass excess of  $-68140(186)$  keV agrees with the present value. However, the  $Q_{EC}$  value of 7793(123) keV [Del82a] with a mass excess of  $-68215(124)$  keV disagrees with it. Similar to  $^{81}\text{Y}$ , the  $\gamma$ -transition gate in the Ge detector gives a higher  $Q_{EC}$  value of 7820(162) keV [Del82a] and a mass excess of  $-68188(163)$  keV in agreement with the value measured in this work.

 $^{83}\text{Y}$ 

The measured mass excess of  $^{83}\text{Y}$ ,  $-72170(6)$  keV, deviates from the AME value,  $-72330(40)$  keV.  $^{83}\text{Y}$  has an isomeric state at 61.98 keV (2.85 min) which could not be resolved in the JYFLTRAP. The  $Q_{EC}$  value of 4571(85) keV for the isomeric beta decay was derived from the  $\beta^+$  spectrum gated by a 422 keV transition in  $^{83}\text{Sr}$  in [Lis81]. It yielded a mass excess of  $-72286(86)$  keV for the ground state.  $Q_{EC}$  values of 4260(80) keV [Dep80] and 4411(50) keV [Del82a] based on  $\beta^+$  spectra in coincidence with a 36 keV  $\gamma$  transition in  $^{83}\text{Sr}$  correspond to the ground-state mass excesses of  $-72535(81)$  keV and  $-72384(51)$  keV, respectively. In [Del82a], a  $Q_{EC}$  value of 4644(84) keV for the isomeric beta decay was also measured. The mass excesses for the isomeric state,  $-72151(85)$  keV [Del82a] and  $-72224(86)$  keV [Lis81], agree with the measured JYFLTRAP value but the ground state values from all beta-decay experiments deviate from it. On the other hand, the errors in the end-point energies are so large that it cannot be concluded that the isomeric state had been measured. In fact, the ground state ( $9/2^+$ ) should be more populated in heavy-ion fusion-evaporation reactions than the isomeric state ( $3/2^-$ ) which suggests that the ground-state mass has been measured.

#### 4.6.4 Zr isotopes

In this experiment, the mass of  $^{84}\text{Zr}$  was measured for the first time. It agrees with the AME value based on systematics. The measured masses of  $^{85}\text{Zr}$  and  $^{88}\text{Zr}$  are also in agreement with the AME values (see fig. 4.37). The discrepancies in the mass excesses of  $^{83}\text{Zr}$  and  $^{86}\text{Zr}$  are discussed in the following subsections.

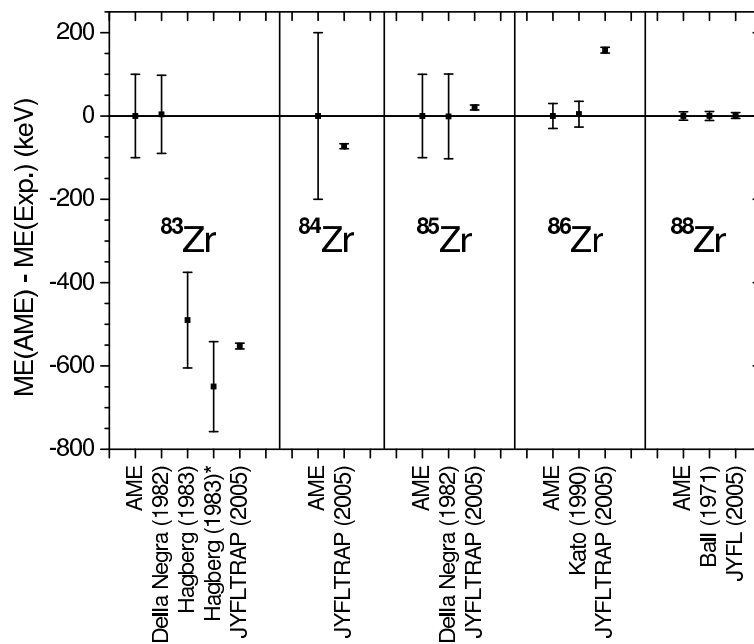


**Figure 4.37:** Mass excesses of the measured Zr isotopes relative to AME values [Aud03b]. The labels refer to beta-decay experiments of Della Negra *et al.* [Del82a] and Hagberg *et al.* [Hag83] and to reaction studies done by Kato *et al.* [Kat90] and Ball *et al.* [Bal71]. The  $^{83}\text{Zr}$  value marked with an asterisk has been calculated with the mass excess of the daughter nucleus  $^{83}\text{Y}$  measured in this experiment at the JYFLTRAP. The other mass excesses have been calculated with the respective AME values.

**$^{83}\text{Zr}$** 

The isomeric state at 52.72 keV (530 ns) in  $^{83}\text{Zr}$  is too short-lived to be observed at JYFLTRAP. The measured ground-state mass excess of  $-65908(7)$  keV was 552 keV higher than the AME value of  $-66460(100)$  keV. The AME value is based on the end point of a  $\beta^+$  spectrum in coincidence with 56 keV, 255 keV, 304 keV and 360 keV  $\gamma$  transitions in  $^{83}\text{Y}$  [Del82a]. The resulting  $Q_{EC}$  value for the beta decay to the  $^{83m}\text{Y}$  (2.85 min) state was 5806(85) keV which converts to a mass excess of  $-66464(94)$  keV when the AME value for  $^{83m}\text{Y}$  is applied. The  $Q_{EC}$  value of [Del82a] was already commented to be too low in [Hag83]. Namely, in [Hag83] the end-point energy of the beta-delayed proton spectrum from  $^{83}\text{Zr}$  was determined. The measured  $Q_{EC} - B_p$  was 2750(100) keV corresponding to a mass excess of  $-65970(115)$  keV where the proton binding energy and the mass excess of  $^{83}\text{Y}$  have been taken from the AME tables. With the mass of  $^{83}\text{Y}$  measured in this work, this results in a mass excess of  $-65810(108)$  keV, still in agreement with the value measured in this work.

The  $Q_{EC} - B_p$  value calculated from the  $Q_{EC}$  value of [Del82a] is only 2196(90) keV which is clearly too low for the beta-delayed proton spectrum presented in [Hag83]. Probable isomerism and complex decays of the nuclides were suggested to explain this discrepancy in [Hag83]. Further support for the work by Hagberg *et al.* [Hag83] comes from this experiment. The mass excess measured at JYFLTRAP agrees with [Hag83] and not with [Del82a]. In addition, the  $Q_{EC}$  value determined from the mass excesses of  $^{83}\text{Y}$  and  $^{83}\text{Zr}$  in this experiment is 6263(9) keV which is much higher than  $Q_{EC}=5868(85)$  keV from [Del82a].

 **$^{84}\text{Zr}$** 

The mass of  $^{84}\text{Zr}$  was measured for the first time. The obtained mass excess agrees well with the AME value based on the systematics. As  $^{84}\text{Zr}$  is situated in the rp process region, its mass is useful, *e.g.*, for the estimation of proton capture reaction rates on  $^{83}\text{Y}$  and  $^{84}\text{Zr}$ . The beta decay  $Q_{EC}$  value for  $^{84}\text{Zr}$  can now be calculated from the AME mass excess of  $^{84}\text{Y}$ ,  $Q_{EC} = 2740(90)$  keV. The proton separation energy for  $^{84}\text{Zr}$  can be determined from the experimental masses of  $^{83}\text{Y}$  and  $^{84}\text{Zr}$  for the first time,  $S_p = 6536(9)$  keV.

 **$^{85}\text{Zr}$** 

The AME value for the mass excess of  $^{85}\text{Zr}$  is  $-73150(100)$  keV. It is based on the end point of the  $\beta^+$  spectrum in coincidence with 416 keV and 453 keV  $\gamma$  transitions in  $^{85}\text{Y}$  [Del82a]. The mass excess obtained at JYFLTRAP,  $-73170(6)$  keV, agrees nicely

with the AME value. The measured mass corresponds to the ground state as it is about 40 times more produced at HIGISOL than the isomeric state at 292.2 keV (see table 3.2) and no second resonance was observed when scanning a wider frequency range.

### <sup>86</sup>Zr

The measured mass excess of <sup>86</sup>Zr,  $-77958(7)$  keV, differs significantly from the AME value,  $-77800(30)$  keV. The AME value is based on a  $Q$ -value of  $-40136(30)$  keV for the reaction  $^{90}\text{Zr}(\alpha, ^8\text{He})^{86}\text{Zr}$  [Kat90]. The difference can be explained with low statistics in the momentum (position) spectrum in [Kat90]. Namely, there were only 7 counts in 80 channels (with a maximum of 2 counts/10 channels) in the momentum spectrum. A peak centroid with an accuracy of  $\pm 8.1$  channels ( $\pm 26$  keV) was fitted on this spectrum. The estimated total error of the reaction  $Q$ -value was given as 30 keV which took into account the errors caused by the uncertainties in the incident energy ( $\pm 14$  keV), in the target thickness ( $\pm 5$  keV) and in the masses of <sup>90</sup>Zr ( $\pm 2$  keV) and  $\alpha$  (less than 1 keV) [Kat90]. A more realistic error estimation with an error for the peak centroid of about  $\pm 40$  channels summed with the systematic errors would give roughly an error of  $\pm 150$  keV for the reaction  $Q$ -value which would be in agreement with the JYFLTRAP value.

### <sup>88</sup>Zr

The measured mass excess of  $-83624(7)$  keV agrees very well with the AME value: the difference is only 1 keV. The AME value is based on a  $Q$ -value of  $-12805(10)$  keV for the reaction  $^{90}\text{Zr}(p, t)^{88}\text{Zr}$  [Bal71].

## 4.6.5 Nb isotopes

Figure 4.38 shows the measured Nb isotopes together with the AME values and previous mass measurements. The large deviations from the AME mass excesses in <sup>85</sup>Nb and <sup>86</sup>Nb might be explained if the masses of isomeric states instead of ground states had been measured, as discussed in sec. 4.6.2. However, the mass excess of <sup>87</sup>Nb also differs significantly from the AME value although the isomeric state should lie at 4 keV which is within the error bars. Only the mass of <sup>88</sup>Nb agrees with the AME value. The mass measurements of <sup>85,86,88</sup>Zr make it possible to determine  $Q_{EC}$  values for the beta decays of <sup>85,86,88</sup>Nb. With the mass of <sup>84</sup>Zr, a proton separation energy for <sup>85</sup>Nb can be experimentally determined for the first time. The measured Zr masses have

been taken into account in the derivation of the Nb mass excesses from beta-decay experiments for these nuclides.

### $^{85}\text{Nb}$

The measured mass excess,  $-66273(7)$  keV, is 877 keV higher than the AME value,  $-67150(220)$  keV. The AME value is based on the end point of a  $\beta^+$  spectrum in coincidence with a 50 keV  $\gamma$  transition in  $^{85}\text{Zr}$  [Kur88]. The  $Q_{EC}$  value of 6100(200) keV [Kur88] yields a mass excess of  $-67050(224)$  keV with the AME value for  $^{85}\text{Zr}$  and  $-67070(224)$  keV with the mass excess of  $^{85}\text{Zr}$  measured in this work, still about 800 keV off from the present value.

The AME value for the mass excess of  $^{85}\text{Nb}$  is based on the  $Q_{EC}$  value given incorrectly in the abstract of [Kur88]. A  $Q_{EC}$  value of 6000(200) keV is given in the abstract instead of the correct 6100(200) keV. The  $Q_{EC}$  value determined from the mass excesses of  $^{85}\text{Nb}$  and  $^{85}\text{Zr}$  measured in this experiment is 6898(9) keV, about 900 keV from the adopted AME value. Also the proton separation energy determined from the measured masses of  $^{84}\text{Zr}$  and  $^{85}\text{Nb}$ ,  $S_p = 2144(9)$  keV differed about 800 keV from the adopted AME value.

The differences in mass excesses and  $Q_{EC}$  values can have several sources. Firstly, the energy calibration of the beta detector in [Kur88] was done with the  $Q_{EC}$  values of  $^{83}\text{Y}$  (4.411 MeV),  $^{83}\text{Zr}$  (5.806 MeV) and  $^{82}\text{Y}$  (7.793 MeV) which were found to be about 214 keV, 395 keV and 155 keV too low in this experiment. Another explanation for the discrepancy in the masses could be that the beta decay of  $^{85}\text{Nb}$  feeds mainly higher-lying levels which then decay to the first excited state at 50 keV in  $^{85}\text{Zr}$ . The high-spin studies of  $^{85}\text{Zr}$  have revealed a  $11/2^+$  state at 854 keV and a  $13/2^+$  state at 872 keV [Jun95, Tan02]. These states decay to the state at 50 keV by 804 keV and 822 keV  $\gamma$  transitions, respectively.

The third possibility is that the mass excess measured in this work is for an isomeric state in  $^{85}\text{Nb}$  instead of the ground state. In a spectroscopic experiment [Oin98b], a 759 keV  $\gamma$  transition with a half-life of 12(5) s was observed at mass  $A = 85$  and it was suggested to originate either from a  $\beta$ -decaying isomer in  $^{85}\text{Nb}$  or in  $^{85}\text{Mo}$ . In addition, a 69 keV isomeric transition with a half-life of 3.3(9) s was observed at mass  $A=85$  in the spectroscopy experiment (see sec. 4.4.2). As a summary, the energy of the isomeric state in  $^{85}\text{Nb}$  is uncertain. The energy range covered in the JYFLTRAP was about  $\pm 900$  keV from the resonance and no indication of an isomer was found. Therefore, the isomeric state suggested by the systematics of odd- $A$  Nb isotopes (see fig. 4.28) should lie above 900 keV, its half-life is below 500 ms or it is much less produced than the ground state. The production ratio of isomeric state to the ground

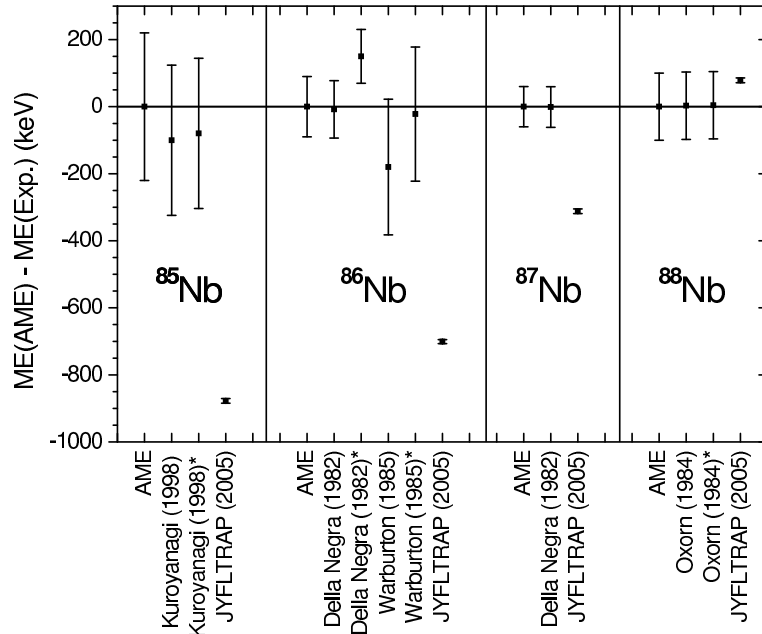


**Figure 4.38:** Mass excesses of the measured Nb isotopes relative to AME values [Aud03b]. The labels refer to beta-decay experiments of Kuroyanagi *et al.* [Kur88], Della Negra *et al.* [Del82b], Warburton *et al.* [War85] and Oxorn and Mark [Oxo84]. The values of  $^{85,85,88}\text{Nb}$  marked with an asterisk have been calculated with the mass excesses of the daughter nuclei  $^{85,86,88}\text{Zr}$  measured in this work. The other mass excesses have been calculated with AME values for daughter nuclei.

state was roughly 1:2 which supports the last option. Most likely the isomeric state was not produced enough for the observation in the trap.

## $^{86}\text{Nb}$

The measured mass excess of  $^{86}\text{Nb}$ ,  $-69129(6)$  keV, differs  $-701$  keV from the AME value of  $-69830(90)$  keV. The AME value is based on [Del82b] which measured the end point of a  $\beta^+$  spectrum in coincidence with 752 keV, 914 keV and 1003 keV  $\gamma$  transitions in  $^{86}\text{Zr}$ . The adopted  $Q_{EC}$  value was 7978(80) keV which converts to a mass excess of  $-69822(86)$  keV with the AME mass excess for  $^{86}\text{Zr}$ . With the JYFLTRAP mass excess of  $^{86}\text{Zr}$ , the resulting mass excess is  $-69980(81)$  keV, which is still far away from the measured mass excess of  $^{86}\text{Nb}$ . The  $Q_{EC}$  value determined from the mass excesses of  $^{86}\text{Zr}$  and  $^{86}\text{Nb}$  measured in this work is 8829(9) keV.

The  $Q_{EC}$  value of [Del82b] was claimed to be wrong already in [War85]. Namely, an erroneous 100 % beta feeding was assumed to the 2670 keV level in  $^{86}\text{Zr}$  in [Del82b]. In [War85] almost equally strong beta feedings to states at 3254 keV and 3418 keV were observed and the  $Q_{EC}$  value was calculated from the weighted average for the final  $^{86}\text{Zr}$  states. By using 752 keV, 916 keV and 1003 keV  $\gamma$ -transition gates for the

$\beta^+$  spectrum, a  $Q_{EC}$  value of 8150(200) keV was concluded in [War85]. The deduced mass excesses of  $^{86}\text{Nb}$ ,  $-69650(203)$  keV (from the AME mass excess of  $^{86}\text{Zr}$ ) and  $-69808(201)$  keV (from the mass excess of  $^{86}\text{Zr}$  measured in this work), are still too low compared to the value measured in this work. Thus, the discrepancy cannot solely be explained by the neglected beta-decay feedings to higher states than 2670 keV unless possible beta-decay feedings to even higher states of  $^{86}\text{Zr}$  have been missed in [War85].

An isomer with a half-life of 56 s in  $^{86}\text{Nb}$  was suggested in [Shi94] based on the time behavior of Zr  $KX$  rays in coincidence with the sum of the 752 keV, 915 keV and 1003 keV  $\gamma$  transitions in  $^{86}\text{Zr}$ . This isomeric state with an unknown energy was not confirmed in the spectroscopy experiment (see sec. 4.4.3). In [Sin01], the existence of this isomer was considered as uncertain as the result has not been confirmed in later experiments. It is also surprising that the ground state assignment of  $^{86}\text{Nb}$  is not experimentally verified, and thus, the lowest observed state with a half-life of 88 s ( $6^+$ ) is considered as an isomer at an energy of  $0 + X$  keV [Sin01]. In this experiment, no isomeric state was found within 450 keV from the resonance in the JYFLTRAP. This means that the suggested isomer is located above 450 keV or is much less produced than the ground state.

### $^{87}\text{Nb}$

The measured mass excess of  $^{87}\text{Nb}$ ,  $-73868(7)$  keV, is significantly larger than the corresponding AME value,  $-74180(60)$  keV. This discrepancy cannot be explained by the known isomeric state as it is located at 4 keV which falls within the error bars of the determined resonance. The AME mass excess is based on the end point of a  $\beta^+$  spectrum in coincidence with 201 keV and 617 keV  $\gamma$  transitions of  $^{87}\text{Zr}$  [Del82b]. The  $Q_{EC}$  value of 5169(60) keV [Del82b] is 311 keV lower than the  $Q_{EC}$  determined from the masses of  $^{87}\text{Zr}$  [Aud03b] and  $^{87}\text{Nb}$  from this work,  $Q_{EC} = 5480(11)$  keV. Either the energy calibration of the  $\beta^+$  detector in [Del82b] is off or the beta decay of  $^{87}\text{Nb}$  to higher-lying states has been underestimated. Note that the mass excess of  $^{86}\text{Nb}$  derived from [Del82b] was also too low compared to this work.

### $^{88}\text{Nb}$

The measured mass excess of  $^{88}\text{Nb}$  agrees with the AME value. The AME mass excess is based on a measurement of the end point of a  $\beta^+$  spectrum in coincidence with a 503 keV transition in  $^{88}\text{Zr}$  [Oxo84]. The  $Q_{EC}$  of 7550(100) keV [Oxo84] is in agreement with the value based on  $^{88}\text{Zr}$  and  $^{88}\text{Nb}$  masses measured in this work,  $Q_{EC} = 7476(9)$  keV. The isomer suggested to lie at 40(140) keV (7.8 min) was not observed within

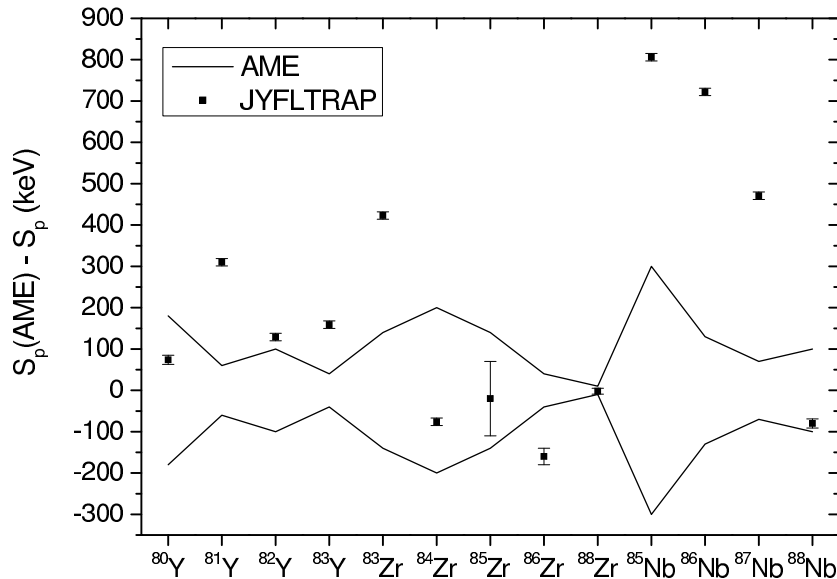


**Figure 4.39:** Proton separation energies for the measured nuclides relative to AME values. The two lines show the corridor of uncertainties taken from ref. [Aud03b]. The mass of the (Z-1,N) nucleus is from this experiment for  $^{83}\text{Zr}$ ,  $^{84}\text{Zr}$ ,  $^{85}\text{Nb}$ ,  $^{86}\text{Nb}$  and  $^{87}\text{Nb}$ . For the others, the AME mass [Aud03a] of the (Z-1,N) nucleus has been used.

310 keV from the resonance. Either the production rate of the isomer was too low or its energy is so close to the ground state that it could not be resolved.

#### 4.6.6 Discussion

Almost all of the studied nuclei lie on the path of the rp process and are involved in the proton captures (see, *e.g.*, ref. [Sch98] and fig. 2.7). The masses of these nuclides have been measured with uncertainties of less than 10 keV required for detailed rp-process calculations [Sch06]. Large deviations to the adopted AME values have been found except for  $^{80}\text{Y}$ ,  $^{84,85,88}\text{Zr}$  and  $^{88}\text{Nb}$  which all agree with the AME values. With the measured absolute masses, the accuracies of proton separation energies and  $Q_{EC}$  values for 12 neutron-deficient nuclei have been improved significantly (see fig. 4.39 and tables 4.12 and 4.13). The  $Q_{EC}$  value for  $^{84}\text{Zr}$  and proton separation energies for  $^{84}\text{Zr}$  and  $^{85}\text{Nb}$  have been experimentally determined for the first time.

The measured masses have also an effect on other masses in the  $A \approx 80$  region. For example, the masses of  $^{81}\text{Zr}$ ,  $^{83}\text{Nb}$  and  $^{85,86,87}\text{Mo}$  are based on beta-decay  $Q$ -values. The masses of the corresponding beta-decay daughters have been measured in this work and found to differ substantially from the adopted AME values. Thus, the masses of the mother nuclides will shift accordingly although the changes will not be very significant due to large errors in the  $Q_{EC}$  values. Of these nuclides, the masses of

**Table 4.12:** Proton separation energies for the measured nuclei. The mass of the (Z-1,N) nucleus is from this experiment for  $^{83}\text{Zr}$ ,  $^{84}\text{Zr}$ ,  $^{85}\text{Nb}$ ,  $^{86}\text{Nb}$  and  $^{87}\text{Nb}$  (marked with †). For the others, the AME mass of the (Z-1,N) nucleus is used [Aud03b]. The last column lists the difference between the determined  $S_p$  value and the corresponding AME value [Aud03b].

Nuclide	$S_p$ (keV) this work	$S_p$ (keV) [Aud03b]	Difference (keV)
$^{80}\text{Y}$	2956(11)	3030(180)	-74
$^{81}\text{Y}$	2690(9)	3000(60)	-310
$^{82}\text{Y}$	3821(9)	3950(100)	-129
$^{83}\text{Y}$	3451(9)	3610(40)	-159
$^{83}\text{Zr}$	5137(9)†	5560(140)	-423
$^{84}\text{Zr}$	6536(9)†	6460(200)#	76
$^{85}\text{Zr}$	6300(90)	6280(140)	20
$^{86}\text{Zr}$	7410(20)	7250(40)	160
$^{88}\text{Zr}$	7895(7)	7893(10)	2
$^{85}\text{Nb}$	2144(9)†	2950(300)#	-806
$^{86}\text{Nb}$	3248(9)†	3970(130)	-722
$^{87}\text{Nb}$	3199(9)†	3670(70)	-471
$^{88}\text{Nb}$	4090(11)	4010(100)	80

**Table 4.13:**  $Q_{EC}$  values for the measured nuclei. The mass of the daughter nucleus is from this experiment for  $^{83}\text{Zr}$ ,  $^{85}\text{Nb}$ ,  $^{86}\text{Nb}$  and  $^{88}\text{Nb}$  (marked with †). For the others, the mass of the daughter nucleus is from ref. [Aud03b]. The last column lists the difference between the determined  $Q_{EC}$  value and the adopted AME value [Aud03b].

Nuclide	$Q_{EC}$ (keV) this work	$Q_{EC}$ (keV) [Aud03b]	Difference (keV)
$^{80}\text{Y}$	9164(10)	9090(180)	74
$^{81}\text{Y}$	5819(9)	5510(60)	309
$^{82}\text{Y}$	7948(9)	7820(100)	128
$^{83}\text{Y}$	4625(12)	4470(40)	155
$^{83}\text{Zr}$	6263(9)†	5870(90)	393
$^{84}\text{Zr}$	2740(90)	2670(220)#	70
$^{85}\text{Zr}$	4670(20)	4690(100)	-20
$^{86}\text{Zr}$	1326(16)	1480(30)	-154
$^{88}\text{Zr}$	675(7)	676(10)	-1
$^{85}\text{Nb}$	6898(9)†	6000(200)	898
$^{86}\text{Nb}$	8829(9)†	7980(80)	849
$^{87}\text{Nb}$	5480(11)	5170(60)	310
$^{88}\text{Nb}$	7476(9)†	7550(100)	-74

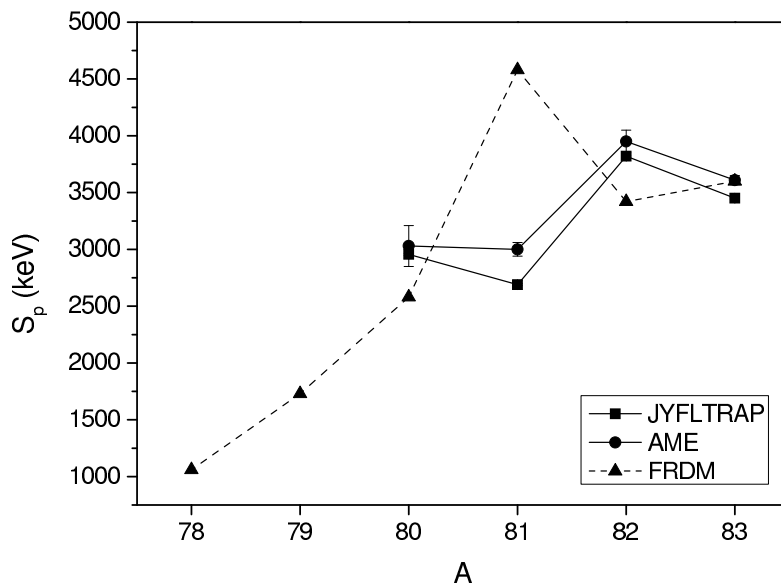


**Figure 4.40:** The proton separation energies of Y isotopes measured in this work (JYFLTRAP), tabulated in [Aud03b] (AME) and based on the FRDM model [Mö197].

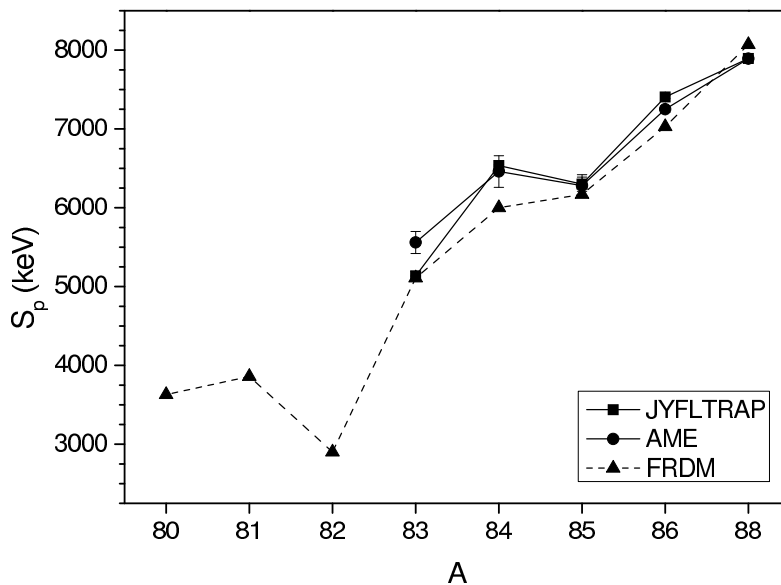


**Figure 4.41:** The proton separation energies of Zr isotopes measured in this work (JYFLTRAP), tabulated in [Aud03b] (AME) and based on the FRDM model [Mö197].

$^{81}\text{Zr}$  and  $^{85}\text{Mo}$  are essential for the determination of the alpha separation energy of  $^{85}\text{Mo}$  which, together with the alpha separation energies for lighter Mo isotopes, is important for the modeling of the Zr-Nb cycle in the rp process (see sec. 2.3.1).

The obtained new data set on masses is not complete enough for a meaningful comparison with theoretical models. However, a commonly used standard reference model in

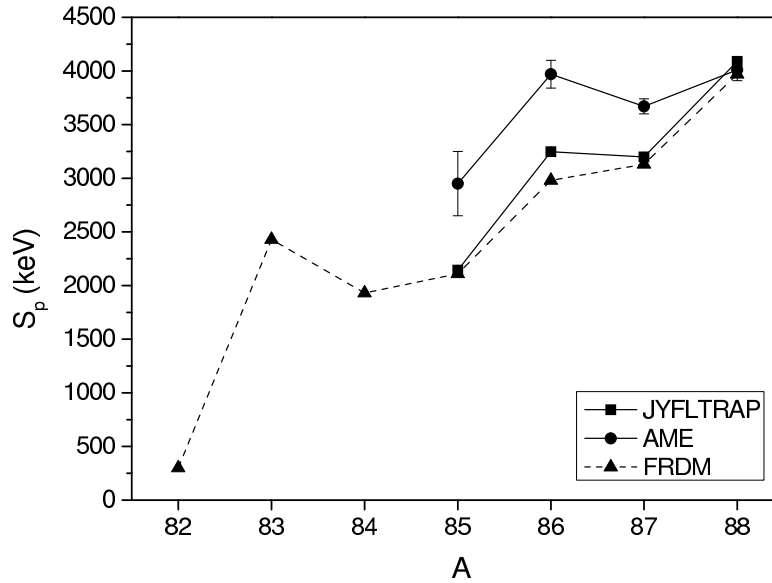


**Figure 4.42:** The proton separation energies of Nb isotopes measured in this work (JYFLTRAP), tabulated in [Aud03b] (AME) and based on the FRDM model [Möl97].

this region of collective structures has been the Finite-Range Droplet-Model (FRDM) of Möller *et al.* [Möl95]. FRDM is a macroscopic-microscopic global mass model in which the macroscopic energy is based on a finite-range droplet model and a folded Yukawa single-particle potential is used for the microscopic corrections. Nuclear properties for astrophysical applications, such as proton separation energies, have been calculated with this model [Möl97]. Figures 4.40, 4.41 and 4.42 show the proton separation energies for the studied nuclides and the corresponding FRDM model predictions which are plotted to the  $T_Z = 0$  nucleus of each isotopic chain [Möl97]. For Y isotopes, there is an unexplained sudden jump in the FRDM model at  $^{81}\text{Y}$ . Better agreement with the FRDM model is obtained with Zr and Nb isotopes. For the Zr isotopes, the proton separation energies determined in this work and the tabulated AME values follow the FRDM model quite well. On the other hand, the proton separation energies of the Nb isotopes determined in this work tend to deviate more and more from the adopted AME values when going towards the proton drip line. At the same time, the separation energies determined in this work agree quite well with the FRDM model. This may change the current estimations for the proton separation energies of the most proton-rich Nb isotopes in [Aud03b], and therefore, the position of the proton dripline.



## 5 Summary and outlook

Neutron-deficient nuclei close to the  $N = Z$  line have been studied in this thesis work via beta-decay spectroscopy at the ISOLDE and IGISOL facilities. In addition, masses of 13 nuclides have been measured with the JYFLTRAP double Penning trap system at IGISOL. The results are important for understanding basic beta-decay properties as well as for modeling the astrophysical rp process and nucleosynthesis in novae.

Beta decay of  $^{31}\text{Cl}$  has been studied with a silicon detector array and a HPGe detector at the IGISOL facility. Previously controversial proton peaks have been confirmed to belong to  $^{31}\text{Cl}$  and a new proton group with an energy of 762(14) keV has been found. Proton captures to this state at 6921(15) keV in  $^{31}\text{S}$  can have an effect on the reaction rate of  $^{30}\text{P}(p,\gamma)$  in ONe novae where the synthesis of heavier elements than sulfur depends on this reaction rate. Gamma rays of 1249.1(14) keV and 2234.5(8) keV corresponding to the de-excitations of the first two excited states in  $^{31}\text{S}$  have been measured. Beta-delayed protons from the IAS with an expected energy of only about 130 keV have not been observed due to experimental limitations. In the future, an efficient setup for beta-gamma spectroscopy would offer a means to detect possible  $\gamma$  decays from the IAS.

Beta decay of  $^{58}\text{Zn}$  has been investigated both at ISOLDE and at IGISOL. At ISOLDE,  $\gamma$  rays with energies of 203 keV and 848 keV have been observed and a half-life of 83(10) ms has been determined from the time behavior of the 203 keV peak. Beta-decay branching ratios for the states at 203 keV and 1051 keV have been calculated. Gamow-Teller strength to the state at 1051 keV has been obtained and compared to the value from  $^{58}\text{Ni}(^3\text{He},t)$  charge-exchange reactions. The results agree within the error bars. Beta-delayed protons from  $^{58}\text{Zn}$  have been searched with the ISOLDE Silicon Ball setup at ISOLDE and at IGISOL. No beta-delayed protons have been observed. The ISOLDE Silicon Ball has been tested on-line with  $^{20}\text{Na}$  and  $^{25}\text{Si}$  and the performance has been found to be good at energies above about 2 MeV. The expected small proton branching of about 2.5% for  $^{58}\text{Zn}$  requires a more efficient setup capable of identifying protons from beta particles and a higher production rate for  $^{58}\text{Zn}$ .

Beta-delayed protons from  $^{69}\text{Kr}$  important for the calculations of 2p capture rates on the waiting-point nucleus  $^{68}\text{Se}$  have been sought with a  $\Delta E - E$  setup at ISOLDE. Unfortunately, no protons have been observed due to a too low production rate of  $^{69}\text{Kr}$ . In future, target development, such as powder targets, can enhance the yield enough for the studies on beta-delayed protons of  $^{69}\text{Kr}$ .

Decay properties of neutron-deficient exotic nuclei close to  $A = 80$  have been investigated using the HIGISOL heavy-ion ion-guide at IGISOL. The studied nuclei,  $^{81}\text{Y}$ ,  $^{81}\text{Sr}$ ,  $^{81m}\text{Kr}$ ,  $^{85}\text{Nb}$ ,  $^{85}\text{Zr}$ ,  $^{86}\text{Mo}$  and  $^{86}\text{Nb}$ , have been produced by a  $^{32}\text{S}$  beam on  $^{54}\text{Fe}$  and  $^{nat}\text{Ni}$  targets. As the half-lives of the nuclides in this region are typically known only from single measurements, they have been remeasured and confirmed. With the setup consisting of the ELLI spectrometer for conversion electrons and a LeGe detector for low-energy  $\gamma$  rays conversion electrons from 43 keV and 221 keV transitions in  $^{81}\text{Sr}$  have been observed for the first time and an internal conversion coefficient for the 43 keV transition has been determined.

A new isomeric transition with an energy of 69 keV and a half-life of  $3.3 \pm 0.9$  s has been observed in  $^{85}\text{Nb}$ , which can be important for the rp-process calculations. Isomeric states typically have different properties than the ground state and can be thermally populated at high astrophysical temperatures and densities. Therefore, the contribution from these states can change proton capture rates and  $\beta^+/\text{EC}$  decay rates considerably.

Four transitions in  $^{86}\text{Nb}$  following the beta decay of  $^{86}\text{Mo}$  have been observed. The measured multipolarities for the transitions change the spin identification of the lowest state at an unknown energy  $E_0$  in  $^{86}\text{Nb}$ . The position of the level at  $E_0$  has not been determined and the existence of an earlier reported isomer with a half-life of 56 s in  $^{86}\text{Nb}$  has not been confirmed.

As a byproduct in the experiment on the nuclides around the  $A = 80$  region, the internal conversion coefficient for a 190.5 keV isomeric transition in  $^{81m}\text{Kr}$  has been measured and the internal transition rate has been determined. The rate has been used to estimate a neutrino-capture rate on  $^{81}\text{Br}$ , which yields a  $\log ft$  of  $5.13 \pm 0.09$  for the reaction  $^{81}\text{Br}(\nu, e^-)^{81m}\text{Kr}$ . Experimental data on the internal conversion coefficient for this transition provided new information about the decay rates which have been controversial. The recalculated neutrino-capture rate is slightly higher than previously claimed supporting a conclusion that  $^{81}\text{Br}$  can be used as a solar neutrino flux detector.

The masses of  $^{80,81,82,83}\text{Y}$ ,  $^{83,84,85,86,88}\text{Zr}$  and  $^{85,86,87,88}\text{Nb}$  have been measured with an accuracy better than 10 keV using the JYFLTRAP setup at IGISOL. The production method at HIGISOL was the same as for the spectroscopy experiment in the  $A = 80$  region. The mass of  $^{84}\text{Zr}$  has been measured for the first time. Large deviations (several hundreds of keV) to the adopted AME values have been found except for  $^{80}\text{Y}$ ,  $^{84,85,88}\text{Zr}$  and  $^{88}\text{Nb}$  which all agree with the adopted values. Isomers have also been sought for the measured nuclei but no isomers have been observed in the JYFLTRAP mainly due to half-life, excitation energy and production rate limitations.

The measured masses and their large deviations from the adopted mass values, which are mainly based on beta-decay end-point energies, can have an impact on the as-

astrophysical rp process network calculations. Accuracies of proton separation energies and beta-decay  $Q_{EC}$  values have been improved significantly for the studied nuclei. The  $Q_{EC}$  value for  $^{84}\text{Zr}$  and proton separation energies for  $^{84}\text{Zr}$  and  $^{85}\text{Nb}$  have been experimentally determined for the first time.

The future of the studies on the nuclei close to the  $N = Z$  line is attractive. The studies of these nuclei are crucial for testing the recent shell-model calculations in the  $pf$  shell, modeling the rp process and understanding phenomena, such as mirror symmetry, in nuclei. The future challenge is to move towards the proton drip line and to heavier elements up to  $^{100}\text{Sn}$ . However, extending the spectroscopic beta-decay studies towards the proton drip line and heavier nuclei requires an improvement in the yields of the isotopes of interest and more efficient detector setups. Concerning the detectors, new silicon detectors with high granularity and ultra-thin dead layers have shown their applicability to the beta-delayed particle spectroscopy. Projects aiming at future radioactive ion beam facilities have pushed forward the target and ion-source development at ISOL facilities. Yields of Kr isotopes have been carefully studied and future possibilities reviewed within the framework of the EURISOL project [Per03]. Long-lived radioactive ion beams planned in the EURISOL project, such as  $^{56}\text{Ni}$  on  $^{40}\text{Ca}$ ,  $^{50}\text{Cr}$  or  $^{58}\text{Ni}$  targets, can provide a way to produce medium-mass  $N \approx Z$  nuclei via fusion-evaporation reactions [Kös03]. As the refractory elements are almost impossible to produce at conventional ISOL facilities, the ion-guide method and the IGISOL facility should offer a good possibility to study neutron-deficient isotopes of refractory elements provided that the production rates are high enough.

At IGISOL, mass experiments on the  $N = Z$  nuclei seem to be very attractive. After the successful experiment on the masses in the  $A = 80$  mass region with JYFLTRAP, there are still many masses and  $Q_{EC}$  values important for the astrophysical rp process waiting to be measured. The measurements could be focused on heavier neutron-deficient nuclides, such as on Mo, Tc, Ru, Rh and Pd isotopes. The extension towards the  $A = 90$  region could be achieved by using a  $^{40}\text{Ca}$  beam on  $^{54}\text{Fe}$  and  $^{nat}\text{Ni}$  targets. Another guideline in the mass measurements of the nuclides close to the  $N = Z$  line, are the  $Q_{EC}$  values for the superallowed  $0^+ \rightarrow 0^+$  beta decays. The  $Q_{EC}$  values for  $^{42}\text{Sc}$  and  $^{46}\text{V}$  have been recently measured at JYFLTRAP [Ero06] and the studies can be extended towards heavier nuclei, such as  $^{50}\text{Mn}$  and  $^{54}\text{Co}$ .

The  $A = 80$  region is also interesting as beta decays of many nuclei in this region, such as  $^{85}\text{Mo}$ , are still not well known. In future, the FURIOS resonance laser ion source [Moo05] can be used to enhance the yields of a specific element at IGISOL substantially. This will be extremely useful in detecting to which isotope a specific transition at a certain mass belongs to. For example, in spectroscopy experiments, several  $\gamma$  transitions have been observed with HPGe detectors at mass  $A=85$  at IGISOL but the transitions could not have been connected to any isotope at  $A = 85$ . At best, the resonance laser ion source can enhance the yield of an isomeric state compared to the

ground state as was shown for  $^{68m}\text{Cu}$  in [Kös00]. Mass selectivity can be further improved by using the JYFLTRAP as an isotope selector and detecting the beta decays after the trap. However, this method will require much higher yields as the majority of the ions are lost on the way through the trap. Another interesting possibility is to do in-trap spectroscopy which has been studied with neutron-rich isotopes at JYFLTRAP [Ris05]. With this method, conversion electrons from a specific nuclide can be directly observed in the trap. The detection of converted transitions could be very useful for further spectroscopic studies in the  $A = 80$  region.

As a conclusion, there is still a lot to study in the neutron-deficient side of the chart of nuclides despite the fact that there will be a huge increase in the studies of neutron-rich nuclides comprising the substantial majority of unknown nuclides. With improved yields, the studies can be extended towards the proton drip line and to heavier nuclides. On the other hand, some of the older experiments can be repeated with significantly improved results, such as was done in the case of the triple  $\alpha$  decay of  $^{12}\text{C}$  [Fyn05]. Further experiments on the nuclei close to the  $N = Z$  line are carried out and planned at IGISOL, thus the search for these exotic nuclides is continuing.

# References

- [And96] B.D. Anderson *et al.*, Phys. Rev. C **54**, 602 (1996).
- [Ang99] C. Angulo *et al.*, Nucl. Phys. A **656**, 3 (1999).
- [Art93] A. Artna-Cohen, Nucl. Data Sheets **70**, 85 (1993).
- [Aud95] G. Audi and A.H. Wapstra, Nucl. Phys. A **595**, 409 (1995).
- [Aud03a] G. Audi, A.H. Wapstra and C. Thibault, Nucl. Phys. A **729**, 3 (2003).
- [Aud03b] G. Audi, A.H. Wapstra and C. Thibault, Nucl. Phys. A **729**, 337 (2003).
- [Axe98] L. Axelsson *et al.*, Nucl. Phys. A **634**, 475 (1998).
- [Bag96] C.M. Baglin, Nucl. Data Sheets **79**, 447 (1996).
- [Bag97] C.M. Baglin, Nucl. Data Sheets **80**, 1 (1997).
- [Bag99] C.M. Baglin, Nucl. Data Sheets **86**, 1 (1999).
- [Bah03] J.N. Bahcall *et al.*, Phys. Rev. Lett. **90**, 131301 (2003).
- [Bal71] J.B. Ball, R.L. Auble and P.G. Roos, Phys. Rev. C **4**, 196 (1971).
- [Ban02] I.M. Band *et al.*, At. Data Nucl. Data Tables **81**, 1 (2002).
- [Bar03] C.J. Barton *et al.*, Phys. Rev. C **67**, 034310 (2003).
- [Ben77] W. Benenson *et al.*, Phys. Rev. C **15**, 1187 (1977).
- [Ber82] G.F. Bertsch and I. Hamamoto, Phys. Rev. C **26**, 1323 (1982).
- [Bér94] R. Béraud *et al.*, Nucl. Instr. and Meth. A **346**, 196 (1994).
- [Ber03] U.C. Bergmann *et al.*, Nucl. Instr. and Meth. A **515**, 657 (2003).
- [Bla95a] B. Blank *et al.*, Phys. Rev. Lett. **74**, 4611 (1995).
- [Bla95b] B. Blank *et al.*, Phys. Lett. B **364**, 8 (1995).
- [Bri98] J. Britz, A. Pape and M.S. Antony, At. Data and Nucl. Data Tables **69**, 125 (1998).

- [Bro02] B.A. Brown *et al.*, Phys. Rev. C **65**, 045802 (2002).
- [Bru77] P.J. Brussaard and P.W.M. Glaudemans, Shell-Model Applications in Nuclear Spectroscopy, North-Holland, Amsterdam (1977).
- [Bur93] T.W. Burrows, Nucl. Data Sheets **68**, 635 (1993).
- [Cas85] R.F. Casten, Nucl. Phys. A **443**, 1 (1985).
- [Cau95] E. Caurier, A. Poves and A.P. Zuker, Phys. Rev. Lett. **74**, 1517 (1995).
- [Cau05] E. Caurier *et al.*, Rev. Mod. Phys. **77**, 427 (2005).
- [Cha05] M. Chartier *et al.*, J. Phys. G **31**, S1771 (2005).
- [Cla04] J.A. Clark *et al.*, Phys. Rev. Lett. **92**, 192501 (2004).
- [Cli89] E.T.H. Clifford *et al.*, Nucl. Phys. A **493**, 293 (1989).
- [Dav68] R. Davis *et al.*, Phys. Rev. Lett. **20**, 1205 (1968).
- [Dav75] J.M. Davidson *et al.*, Nucl. Phys. A **240**, 253 (1975).
- [Dav87] C.N. Davids *et al.*, Phys. Rev. C **35**, 1114 (1987).
- [Del82a] S. Della Negra *et al.*, Z. Phys. A **307**, 305 (1982).
- [Del82b] S. Della Negra, D. Jacquet and Y. Le Beyec, Z. Phys. A **308**, 243 (1982).
- [Den97] P. Dendooven, Nucl. Instr. and Meth. B **126**, 182 (1997).
- [Den98] P. Dendooven *et al.*, Nucl. Instr. and Meth. in Phys. Res. A **408**, 530 (1998).
- [Dep80] C. Deprun *et al.*, Z. Phys. A **295**, 103 (1980).
- [Dog56] W.O. Doggett, Lawrence Radiation Laboratory Report No. UCRL-3438, 1956, unpublished.
- [Dzh72] B.S. Dzhelepov *et al.*, Beta Processes, Functions for the Analysis of Beta Spectra and Electron Capture, Nauka, Leningrad 1972.
- [Ebe01] J. Eberth *et al.*, Progress in Particle and Nucl. Phys. **46**, 389 (2001).
- [End78] P.M. Endt and C. Van Der Leun, Nucl. Phys. A **310**, 1 (1978).
- [End90] P.M. Endt, Nucl. Phys. A **521**, 1 (1990).
- [End98] P.M. Endt, Nucl. Phys. A **633**, 1 (1998).
- [Ero06] T. Eronen *et al.*, Phys. Lett. B **636**, 191 (2006).

- [Ewa80] G.T. Ewan *et al.*, Nucl. Phys. A **343**, 109 (1980).
- [Ewa81] G.T. Ewan *et al.*, Nucl. Phys. A **352**, 13 (1981).
- [Fae70] A. Faessler *et al.*, Z. Phys. A **238**, 352 (1970).
- [Fed00] V.N. Fedoseyev *et al.*, Hyperfine Interactions **127**, 409 (2000).
- [Fed03] V.N. Fedoseyev *et al.*, Nucl. Instr. and Meth. B **204**, 353 (2003).
- [Fra03] L.M. Fraile and J. Äystö, Nucl. Instr. and Meth. A **513**, 287 (2003).
- [Frö06] C. Fröhlich *et al.*, Phys. Rev. Lett. **96**, 142502 (2006).
- [Fuj97] Y. Fujita *et al.*, Nucl. Instr. and Meth. B **126**, 274 (1997).
- [Fuj99] Y. Fujita *et al.*, Phys. Rev. C **59**, 90 (1999).
- [Fuj01] H. Fujita *et al.*, Nucl. Instr. and Meth. A **469**, 55 (2001).
- [Fuj02a] Y. Fujita *et al.*, Phys. Rev. C **66**, 044313 (2002).
- [Fuj02b] Y. Fujita *et al.*, Eur. Phys. J. A **13**, 411 (2002).
- [Fuj03] Y. Fujita *et al.*, Phys. Rev. C **67**, 064312 (2003).
- [Fuj04] Y. Fujita *et al.*, Phys. Rev. C **70**, 054311 (2004).
- [Fuj05] Y. Fujita *et al.*, Phys. Rev. Lett. **95**, 212501 (2005).
- [Fuj06] H. Fujita *et al.*, *to be published*.
- [Fyn05] H.O.U. Fynbo *et al.*, Nature **433**, 136 (2005).
- [Gil03] T.J. Giles *et al.*, Nucl. Instr. and Meth. B **204**, 497 (2003).
- [Goo80] C.D. Goodman *et al.*, Phys. Rev. Lett. **44**, 1755 (1980).
- [Gov71] N.B. Gove and M.J. Martin, Nucl. Data Tables **10**, 205 (1971).
- [Gro00] D.E. Groom *et al.*, Eur. Phys. J. C **15**, 1 (2000).
- [Hag83] E. Hagberg *et al.*, Nucl. Phys. A **395**, 152 (1983).
- [Han69] P.G. Hansen *et al.*, Phys. Lett. B **28**, 415 (1969).
- [Har71] J.C. Hardy *et al.*, Phys. Rev. C **3**, 700 (1971).
- [Har98] J.C. Hardy and I.S. Towner, p.733 in B.M. Sherrill, D.J. Morrissey, C.N. Davids (Eds.), Proc. ENAM98, Exotic Nuclei and Atomic Masses, AIP Conf. Proc. Vol. 455 (1998).

- [Har02] J.C. Hardy and I.S. Towner, Phys. Rev. Lett. **88**, 252501 (2002).
- [Har03] K. Hara *et al.*, Phys. Rev. C **68**, 064612 (2003).
- [Har05] J.C. Hardy and I.S. Towner, Phys. Rev. C **71**, 055501 (2005).
- [Hel02] R.G. Helmer, Nucl. Data Sheets **95**, 543 (2002).
- [Hon81] J. Honkanen, PhD Thesis, Research Report No. 17, Department of Physcis, University of Jyväskylä (1981).
- [Hon98] A. Honkanen, PhD Thesis, Research Report No. 3, Department of Physcis, University of Jyväskylä (1998).
- [Hui03] J. Huikari, PhD Thesis, Research Report No. 10, Department of Physcis, University of Jyväskylä (2003).
- [Hui04] J. Huikari *et al.* Nucl. Instr. and Meth. B **222**, 632 (2004).
- [Ike62] K. Ikeda, S. Fujii and J.I. Fujita, Phys. Lett **2**, 169 (1962).
- [Isa99] P. Van Isacker, O. Juillet and F. Nowacki, Phys. Rev. Lett. **82**, 2060 (1999).
- [Isa02] P. Van Isacker, Nucl. Phys. A **704**, 232c (2002).
- [ISO06] <http://isolde.web.cern.ch/ISOLDE>
- [Iss98] S. Issmer *et al.*, Eur. Phys. J. A **2**, 173 (1998).
- [Jan01] Z. Janas *et al.*, Eur. Phys. J. A **12**, 143 (2001).
- [Jen05] D.G. Jenkins *et al.*, Phys. Rev. C **72**, 031303(R) (2005).
- [Jok96] A. Jokinen *et al.*, Z. Phys. A **355**, 227 (1996).
- [Jok98] A. Jokinen *et al.*, Eur. Phys. J. A **3**, 271 (1998).
- [Jok02] A. Jokinen *et al.*, EPJdirect **A3**, 1 (2002).
- [Jon00] B. Jonson and A. Richter, Hyperfine Interactions **129**, 1 (2000).
- [Jos99] J. José, A. Coc and M. Hernanz, Astrophys. J. **520**, 347 (1999).
- [Jos01] J. José, A. Coc and M. Hernanz, Astrophys. J. **560**, 897 (2001).
- [Jos05] J. José, Nucl. Phys. A **752**, 540c (2005).
- [Jos06] J. José, M. Hernanz and C. Iliadis, Nucl. Phys. A, *in press*.
- [Jun95] A. Jungclaus *et al.*, Z. Phys. A **352**, 3 (1995).

- [Kan95] J. Kantele, Handbook of nuclear spectrometry, Academic Press Limited, Cornwall (U.K.), 1995.
- [Kan04] K. Kaneko, M. Hasegawa and T. Mizusaki, Phys. Rev. C **70**, 051301(R) (2004).
- [Kat90] S. Kato *et al.*, Phys. Rev. C **41**, 1276 (1990).
- [Kol04] V.S. Kolhinen *et al.*, Nucl. Instr. and Meth. A **528**, 776 (2004).
- [Kra88] K.S. Krane, Introductory nuclear physics, John Wiley Sons Inc., New York, 1988.
- [Kro87] D. Krofcheck *et al.*, Phys. Lett. B **189**, 299 (1987).
- [Kug00] E. Kugler, Hyperfine Interactions **129**, 23 (2000).
- [Kur88] T. Kuroyanagi *et al.*, Nucl. Phys. A **484**, 264 (1988).
- [Kur03] H. Kurasawa, T. Suzuki and N. Van Giai, Phys. Rev. Lett. **91**, 062501 (2003).
- [Kön95] M. König *et al.*, Int. J. Mass Spectr. Ion. Proc. **142**, 95 (1995).
- [Kös00] U. Köster *et al.*, Hyperfine Interactions **127**, 417 (2000).
- [Kös02a] U. Köster, Eur. Phys. J. A **15**, 255 (2002).
- [Kös02b] U. Köster, Nucl. Phys. A **701**, 441c (2002).
- [Kös03] U. Köster, A presentation in the Third Eurisol Town Meeting, Orsay, 12-13 May 2003. <http://www.ganil.fr/eurisol/TOWNMEETINGORSAY3/Ullik%20F6ster-Batch-Prod.pdf>
- [Lal01] A.S. Lalleman *et al.*, Hyperfine Interact. **132**, 315 (2001).
- [Let97] J. Lettry *et al.*, Nucl. Instr. and Meth. B **126**, 130 (1997).
- [Lim02] G.F. Lima *et al.*, Phys. Rev. C **65**, 044618 (2002).
- [Lip77] J. Lipták *et al.*, Nucl. Phys. A **286**, 263 (1977).
- [Lis81] C.J. Lister *et al.*, Phys. Rev. C **24**, 260 (1981).
- [Lis87] C.J. Lister *et al.*, Phys. Rev. Lett. **59**, 1270 (1987).
- [Lóp02] M.J. López Jiménez *et al.*, Phys. Rev. C **66**, 025803 (2002).
- [Low87] M.M. Lowry *et al.*, Phys. Rev. C **35**, 1950 (1987).

- [Mar96] G. Martínez-Pinedo *et al.*, Phys. Rev. C **53**, R2602 (1996).
- [Mis93] V.I. Mishin *et al.*, Nucl. Instr. and Meth. **B73**, 550 (1993).
- [Moh91] M.F. Mohar *et al.*, Phys. Rev. Lett. **66**, 1571 (1996).
- [Moo05] I.D. Moore *et al.*, J. Phys. G **31**, S1499 (2005).
- [Mut91] K. Muto *et al.*, Phys. Rev. C **43**, 1487 (1991).
- [Möl95] P. Möller, J.R. Nix, W.D. Myers and W.J. Swiatecki, At. Data and Nucl. Data Tables **59**, 185 (1995).
- [Möl97] P. Möller, J.R. Nix and K.-L. Kratz, At. Data and Nucl. Data Tables **66**, 131 (1997).
- [Nie01] A. Nieminen *et al.*, Nucl. Instr. and Meth. A **469**, 244 (2001).
- [NNDC] <http://www.nndc.bnl.gov/logft>
- [Nov01] Yu.N. Novikov *et al.*, Eur. Phys. J. A **11**, 257 (2001).
- [Ogn96] T.J. Ognibene *et al.*, Phys. Rev. C **54**, 1098 (1996).
- [Oin97] M. Oinonen *et al.*, Phys. Rev. C **56**, 745 (1997).
- [Oin98a] M. Oinonen, PhD Thesis, Research Report No. 4, Department of Physics, University of Jyväskylä (1998).
- [Oin98b] M. Oinonen *et al.*, Nucl. Instr. and Meth. A **416**, 485 (1998).
- [Oin00] M. Oinonen *et al.*, Hyperfine Interactions **127**, 431 (2000).
- [Oin02] M. Oinonen *et al.*, Nucl. Phys. A **701**, 613c (2002).
- [Ost92] F. Osterfeld, Rev. Mod. Phys. **64**, 491 (1992).
- [Oxo84] K. Oxorn and S.K. Mark, Z. Phys. A **316**, 97 (1984).
- [Par91] J.M. Parmonen *et al.*, Nucl. Instr. and Meth. A **306**, 504 (1991).
- [Pek94] L.K. Peker, Nucl. Data Sheets **73**, 1 (1994).
- [Pen97] H. Penttilä *et al.*, Nucl. Instr. and Meth. B **126**, 213 (1997).
- [Pen05] H. Penttilä *et al.*, Eur. Phys. J. A **25**, s01, 745 (2005).
- [Per00] K. Peräjärvi *et al.*, Phys. Lett. B **492**, 1 (2000).
- [Per01a] K. Peräjärvi, PhD Thesis, Research Report No. 3, Department of Physics, University of Jyväskylä (2001).

- [Per01b] K. Peräjärvi *et al.*, Nucl. Phys. A **696**, 233 (2001).
- [Per03] K. Peräjärvi, A presentation in the Third Eurisol Town Meeting, Orsay, 12-13 May 2003. <http://www.ganil.fr/eurisol/TOWNMEETINGORSAY3/KariPerajarvi.pdf>
- [Pfa96] R. Pfaff *et al.*, Phys. Rev. C **53**, 1753 (1996).
- [Rap83] J. Rapaport and E. Sugarbaker, Nucl. Phys. A **410**, 371 (1983).
- [Rap94] J. Rapaport and E. Sugarbaker, Annu. Rev. Nucl. Part. Sci. **44**, 109 (1994).
- [Rau00] T. Rauscher and F.-K. Thielemann, At. Data and Nucl. Data Tables **75**, 1 (2000).
- [Res00] J.J. Ressler *et al.*, Phys. Rev. Lett. **84**, 2104 (2000).
- [Ris05] J. Rissanen, MSc Thesis, Department of Physics, University of Jyväskylä.
- [Rud02] D. Rudolph *et al.*, Eur. Phys. J. A **14**, 137 (2002).
- [Sch95] K. Schreckenbach *et al.*, Phys. Lett. B **349**, 427 (1995).
- [Sch98] H. Schatz *et al.*, Phys. Reports **294**, 167 (1998).
- [Sch01a] H. Schatz *et al.*, Phys. Rev. Lett. **86**, 3471 (2001).
- [Sch01b] H. Schatz *et al.*, Nucl. Phys. A **688**, 150c (2001).
- [Sch06] H. Schatz and K.E. Rehm, Nucl. Phys. A, *in press*.
- [Sco76] R.D. Scott, Nature **264**, 729 (1976).
- [Set86] K.K. Seth *et al.*, Phys. Lett. B **173**, 397 (1986).
- [Shi94] T. Shizuma *et al.*, Z. Phys. A **348**, 25 (1994).
- [Shi96] M. Shibata *et al.*, J. Phys. Soc. Jpn. **65**, 3172 (1996).
- [Sie91] H. Sievers, Nucl. Data Sheets **62**, 271 (1991).
- [Sin98] B. Singh, Nucl. Data Sheets **85**, 1 (1998).
- [Sin01] B. Singh, Nucl. Data Sheets **94**, 1 (2001).
- [SRIM03] SRIM2003. <http://www.srim.org/SRIM/SRIM2003.htm>
- [Tal62] I. Talmi, Rev. Mod. Phys **34**, 704 (1962).
- [Tan02] S.K. Tandel *et al.*, Phys. Rev. C **65**, 054307 (2002).

- [Ten04] O. Tengblad *et al.*, Nucl. Instr. and Meth. A **525**, 458 (2004).
- [Tho04] J.-C. Thomas *et al.*, Eur. Phys. J. A **21**, 419 (2004).
- [Tow79] I.S. Towner and F.C. Khanna, Phys. Rev. Lett. **42**, 51 (1979).
- [Tow02] I.S. Towner and J.C. Hardy, Phys. Rev. C **66**, 035501 (2002).
- [Toy79] K. Toyoshima, Nucl. Phys. A **323**, 61 (1979).
- [Ver99] J. Vernotte *et al.*, Nucl. Phys. A **655**, 415 (1999).
- [Väi75] S. Väisälä *et al.*, Phys. Fenn. **10**, 133 (1975).
- [Wal81] R.K. Wallace and S.E. Woosley, Astrophys. J. Suppl. Series **45**, 389 (1981).
- [Wap03] A.H. Wapstra, G. Audi and C. Thibault, Nucl. Phys. A **729**, 129 (2003).
- [War85] E.K. Warburton *et al.*, Phys. Rev. C **31**, 1211 (1985).
- [Wie99] M. Wiescher, J. Görres and H. Schatz, J. Phys. G. Nucl. Part. Phys. **25**, R133 (1999).
- [Wie05] M. Wiescher, Nucl. Phys. A **751**, 285c (2005).
- [Wil69] D.H. Wilkinson (edit.), *Isospin in nuclear physics*, North-Holland, Amsterdam 1969.
- [Wil78] D.H. Wilkinson *et al.*, Phys. Rev. C **18**, 401 (1978).
- [Wil83] B.H. Wildenthal, M.S. Curtin and B.A. Brown, Phys. Rev. C **28**, 1343 (1983).
- [Wil05] D.H. Wilkinson, Nucl. Instr. and Meth. A **543**, 497 (2005).
- [Wor94] L. Van Wormer *et al.*, Astrophys. J. **432**, 326 (1994).
- [Wöh04] A. Wöhr *et al.*, Nucl. Phys. A **742**, 349 (2004).
- [Xu97] X.J. Xu *et al.*, Phys. Rev. C **55**, R553 (1997).
- [Ärj81] J. Ärje and K. Valli, Nucl. Instr. and Meth. **179**, 533 (1981).
- [Ärj86] J. Ärje, PhD Thesis, Research Report No. 3, Department of Physics, University of Jyväskylä (1986).
- [Äys76] J. Äystö, Nucl. Instr. and Meth. B **139**, 325 (1976).
- [Äys82] J. Äystö *et al.*, Phys. Lett. **110B**, 437 (1982).

- 
- [Äys83] J. Äystö *et al.*, Phys. Scr. **T5**, 193 (1983).  
[Äys84] J. Äystö *et al.*, Phys. Lett. **138B**, 369 (1984).  
[Äys85] J. Äystö *et al.*, Phys. Rev. C **32**, 1700 (1985).  
[Äys01] J. Äystö, Nucl. Phys. A **693**, 477 (2001).  
[Äys04] J. Äystö, Phys. Rep. **403-404**, 459 (2004).